

Lava Flow Emplacement in Harrat Rahat with Implications for Eruptions in Mafic Volcanic Fields

Chapter E of

Active Volcanism on the Arabian Shield—Geology, Volcanology, and Geophysics of Northern Harrat Rahat and Vicinity, Kingdom of Saudi Arabia



U.S. Geological Survey Professional Paper 1862
Saudi Geological Survey Special Report SGS–SP–2021–1

Cover. Aerial view (facing northwest) of the eruptive fissures and pāhoehoe lava channel of the basalt of Central Finger that erupted 24.4 ± 1.3 thousand years ago. This eruption produced a 15.7-kilometer-long lava flow and effused a total volume of 70 million cubic meters dense rock equivalent of lava. Features in the background include the scoria cone vents and basaltic lava flows from several nearby units, including the basalt of the Northern Fingers (upper right). U.S. Geological Survey photograph by Hannah Dietterich, 2016. Background image shows northern Harrat Rahat lava flows, maars, and lava domes. U.S. Geological Survey photograph by Andrew Calvert, January 25, 2012.

Lava Flow Emplacement in Harrat Rahat with Implications for Eruptions in Mafic Volcanic Fields

By Hannah R. Dietterich, Drew T. Downs, and Mark E. Stelten

Chapter E of

Active Volcanism on the Arabian Shield—Geology, Volcanology, and Geophysics of Northern Harrat Rahat and Vicinity, Kingdom of Saudi Arabia

Edited by Thomas W. Sisson, Andrew T. Calvert, and Walter D. Mooney

U.S. Geological Survey Professional Paper 1862
Saudi Geological Survey Special Report SGS–SP–2021–1

U.S. Department of the Interior
U.S. Geological Survey

U.S. Geological Survey, Reston, Virginia: 2023

For more information on the USGS—the Federal source for science about the Earth, its natural and living resources, natural hazards, and the environment—visit <https://www.usgs.gov> or call 1–888–ASK–USGS.

For an overview of USGS information products, including maps, imagery, and publications, visit <https://store.usgs.gov>.

Any use of trade, firm, or product names is for descriptive purposes only and does not imply endorsement by the U.S. Government.

Although this information product, for the most part, is in the public domain, it also may contain copyrighted materials as noted in the text. Permission to reproduce copyrighted items must be secured from the copyright owner.

Suggested citation:

Dietterich, H.R., Downs, D.T., and Stelten, M.E., 2023, Lava flow emplacement in Harrat Rahat with implications for eruptions in mafic volcanic fields, chap. E of Sisson, T.W., Calvert, A.T., and Mooney, W.D., eds., Active volcanism on the Arabian Shield—Geology, volcanology, and geophysics of northern Harrat Rahat and vicinity, Kingdom of Saudi Arabia: U.S. Geological Survey Professional Paper 1862 [also released as Saudi Geological Survey Special Report SGS–SP–2021–1], 49 p., <https://doi.org/10.3133/pp1862E>.

ISSN 1044-9612 (print)

ISSN 2330-7102 (online)



هيئة المساحة الجيولوجية السعودية
SAUDI GEOLOGICAL SURVEY

Ministry of Industry and Mineral Resources

BANDAR BIN IBRAHIM BIN ABDULLAH AL-KHORAYEF, Minister and SGS Chairman

Saudi Geological Survey

Abdullah bin Mufter Al-Shamrani, Chief Executive Officer

Saudi Geological Survey, Jiddah, Kingdom of Saudi Arabia: 2023

Contents

Abstract.....	1
Introduction.....	1
Geologic Setting.....	2
Methods.....	5
Morphologic Analysis	5
Flow and Channel Mapping	5
Preruptive Topography, Thickness, and Volume	5
Geochemical and Textural Analysis	8
Characterization of Lava Temperature, Viscosity, and Effusion Rate	8
Geothermometry	8
Viscosity	8
Estimation of Effusion Rates	9
Results	10
Whole-Rock Geochemistry	10
Morphologic Analysis	10
Petrologic Analysis.....	12
Analysis of Emplacement Conditions	12
Thermometry.....	12
Viscosity	12
Effusion Rates.....	18
Eruption Durations	20
Discussion.....	20
Cooling and Crystallization	20
Flow Volumes.....	22
Flow Dynamics	22
Conclusions.....	24
Acknowledgments.....	24
References Cited.....	24
Appendix 1. Samples for X-ray Fluorescence Analysis	32
Appendix 2. Samples for Textural Analysis	33
Appendix 3. Microprobe Analyses of Glass in Harrat Rahat Basaltic Lava Flows	34
Appendix 4. Microprobe Analyses of Plagioclase in Harrat Rahat Basaltic Lava Flows	40
Appendix 5. Microprobe Analyses of Olivine in Harrat Rahat Basaltic Lava Flows	45
Appendix 6. Geothermometry Results and Sample Locations	49

Figures

1. Maps of the study area in the western part of the Kingdom of Saudi Arabia	3
2. Photographs of studied lava flows in Harrat Rahat wide	4
3. Maps showing the morphological analysis methods using an example from the south branch of the Southern flow	5
4. Example of the profile interpolation method used for thickness measurements	6
5. Plots of morphometric data derived along each lava flow	11
6. Plot of textural changes with distance down flow	13
7. Plot of lava temperatures calculated using liquid, olivine-liquid, and plagioclase-liquid geothermometers versus distance down flow	13
8. Plot of apparent viscosities with distance down flow	18
9. Plots of flow and channel width versus slope	19
10. Plot of calculated temperature versus measured crystallinity for all studied flows	20
11. Plot of flow length versus effusion rate for the four studied Harrat Rahat lava flows compared with the global dataset	23

Tables

1. Representative whole-rock chemical analyses of the 1256 C.E. and Five Fingers lava flows, northern Harrat Rahat.....	7
2. Flow and channel morphology results for northern Harrat Rahat flows.....	10
3. Microprobe analyses of glass, plagioclase, and olivine compositions from northern Harrat Rahat lava flows.....	14
4. Textural analysis, thermometry, and viscosity results.....	16
5. Harrat Rahat lava effusion rate, duration, and advance rate estimates	19
6. Global lava effusion rate, duration, and advance rate estimates	21

Conversion Factors

International System of Units to U.S. customary units

Multiply	By	To obtain
Length		
micrometer (μm)	0.00003937	inch (in.)
millimeter (mm)	0.03937	inch (in.)
meter (m)	3.281	foot (ft)
kilometer (km)	0.6214	mile (mi)
meter (m)	1.094	yard (yd)
Area		
square meter (m^2)	0.0002471	acre
square meter (m^2)	10.76	square foot (ft^2)
Volume		
cubic meter (m^3)	35.31	cubic foot (ft^3)
cubic meter (m^3)	1.308	cubic yard (yd^3)
cubic kilometer (km^3)	0.2399	cubic mile (mi^3)
Flow rate		
cubic meter per second (m^3/s)	70.07	acre-foot per day (acre-ft/d)
meter per hour (m/h)	3.281	foot per hour (ft/h)
cubic meter per second (m^3/s)	35.31	cubic foot per second (ft^3/s)
meter per hour (m/h)	39.37	inch per hour (in/h)
Density		
kilogram per cubic meter (kg/m^3)	0.06242	pound per cubic foot (lb/ft^3)

Temperature in degrees Celsius ($^{\circ}\text{C}$) may be converted to degrees Fahrenheit ($^{\circ}\text{F}$) as follows:
 $^{\circ}\text{F} = (1.8 \times ^{\circ}\text{C}) + 32.$

Abbreviations

A.H.	in the year of the Hijra
C.E.	Common Era
$^{\circ}\text{C}/\text{km}$	degree Celsius per kilometer
DEM	digital elevation model
DRE	dense rock equivalent
ka	thousand years ago
LOI	loss on ignition
nA	nanoampere
Pa	pascal
Pa-s	pascal second
s^{-1}	per second

Chapter E

Lava Flow Emplacement in Harrat Rahat with Implications for Eruptions in Mafic Volcanic Fields

By Hannah R. Dietterich, Drew T. Downs, and Mark E. Stelten

Abstract

Mafic volcanic fields are widespread, but few have erupted in historical times, providing limited observations of the magnitudes, dynamics, and timescales of lava flow emplacement in these settings. The Harrat Rahat volcanic field in western Saudi Arabia offers a good opportunity to study eruptions in such a setting, with a historical eruption in 1256 C.E. (654 in the year of the Hijra) and numerous well-preserved late Pleistocene lava flows. We combine historical observations and rheological and morphological analyses of the youngest flows with analytical models to reconstruct eruptive histories and lava flow emplacement conditions in Harrat Rahat. Petrologic analysis of samples for emplacement temperatures and crystallinities show cooling trends from vent to toe of ~1,140 to ~1,090 degrees Celsius (°C) at rates of 2 to 7 °C per kilometer, crystallinities increasing from 0.5 to 60 volume percent, and apparent viscosities increasing from 10² to 10⁹ pascal seconds. High-resolution topographic data facilitate quantitative analysis of morphology and interpolation of preeruptive surfaces to measure flow thicknesses, channels, and levees, and enable calculation of eruptive volumes. Analytical models relating flow morphology to emplacement conditions are applied to estimate effusion rates. Within the suite of studied flows, minimum volume estimates range from 0.07 to 0.42 cubic kilometers dense rock equivalent, with effusion rates on the order of tens to hundreds of cubic meters per second and durations from 1 to 15 weeks. These integrated analyses quantify past lava flow emplacement conditions and dynamics in Harrat Rahat, improving our understanding and observations of fundamental parameters and controls of effusive eruptions in Harrat Rahat and other mafic volcanic fields.

Introduction

Mafic lava flows are the most prevalent volcanic landform on Earth and affect communities around the world (Walker, 2000; Harris, 2015; Siebert and others, 2015). Observations of emplacement conditions of these flows are concentrated at volcanic centers with frequent historical activity, but similar observations of more sporadic eruptions from mafic volcanic fields, of which >200 have been active during the Holocene,

are missing (Siebert and others, 2011). Such volcanic fields are widespread globally and are characterized by distributed volcanism that produces numerous, typically monogenetic volcanoes within an area (Valentine and Connor, 2015). However, with few historical eruptions (Smith and Németh, 2017), the paucity of observations of active flows in these settings has limited our understanding of their magnitudes, rheologies, dynamics, and durations. Sparse data from observed eruptions, such as at Parícutín, Mexico (1943–1952; Foshag and González, 1956), demonstrate that effusive eruptions in mafic volcanic fields can be long lived and produce extensive flows. More recently, geologic studies of prehistoric mafic volcanic field eruptions have begun to characterize these flows and their eruption conditions (Loock and others, 2010; Chevrel and others, 2016; Deligne and others, 2016; Soldati and others, 2017). However, questions remain about the range of sizes, durations, physical properties, and dynamics of effusive eruptions from mafic volcanic fields, with implications for future flow behavior, hazards, and impacts (Harris, 2015). Observations and analysis of flow emplacement are therefore needed to improve our records, modeling, and understanding of eruptive behavior in these settings.

Studies of active and solidified lava flows, as well as experimental and analytical modeling, demonstrate the close association between emplacement conditions, lava flow length and advance, and final postemplacement flow textures and morphology (Macdonald, 1953; Walker, 1973; Griffiths, 2000). Fundamental emplacement parameters include lava effusion rate, flow rheology, and eruption duration (Walker, 1973; Kilburn and Lopes, 1991; Harris and others, 2007a). Past investigations have shown that higher effusion rates produce flows with higher advance rates and greater lengths (Walker, 1973; Pinkerton and Wilson, 1994; Kauahikaua and others, 2003) and have used channel dimensions to estimate effusion rates based on analytical theory (Kerr and others, 2006; Chevrel and others, 2013; Soldati and others, 2017). Effusion rate may be characterized for different spatial scales, such as a whole flow field or a local lava channel, and timescales, including an average or mean output rate calculated by dividing the total volume by the duration of the eruption, a time-averaged discharge rate over a period, or an instantaneous measure (Harris and others, 2007a). Lava

rheology has been experimentally tied to lava temperature and composition (Giordano and others, 2008), as well as to the presence and characteristics of crystals and bubbles (Mader and others, 2013), and is reflected in flow and channel morphology in experiments and natural flows (Hulme, 1974; Kerr and others, 2006; Chevrel and others, 2013; Kolzenburg and others, 2018). We can employ the relations between lava flow petrology, morphology, and emplacement parameters to quantify the intensities and magnitudes (effusion rates and volumes), rheologies, dynamics, and timescales that control flow behavior, thereby building our understanding of eruptions in mafic volcanic fields.

Morphological and rheological analyses have proved valuable for assessing eruptive volumes at volcanic fields around the world and have offered some of the first results to characterize rheological evolution in these systems (Chevrel and others, 2016; Deligne and others, 2016; Soldati and others, 2017). Applications of flow morphology have largely used coarse cross sections with detailed rheological analysis (Chevrel and others, 2013, 2016; Kolzenburg and others, 2017; Soldati and others, 2017), or high-resolution topography without rheology measurements (Deardorff and Cashman, 2012). Integrating analysis of high-resolution topographic data with petrologic investigations and analytical models of rheology and lava channelization allows us to quantify the properties of past eruptions at such locations.

In this chapter, we expand on the work of Dietterich and others (2018) and employ this integrated methodology for reconstructing emplacement conditions to a set of young lava flows in the Harrat Rahat volcanic field in western Saudi Arabia. We integrate historical records, mapping, geochemistry, petrology, and morphologic analysis of these recent lava flows in Harrat Rahat to evaluate their eruption temperatures and initial viscosities, investigate their rheological evolution, and estimate volumes, effusion rates, and durations. We find that these methods work well for characterizing the glassy, well-exposed, young (<25 thousand years old [ka]) lavas in Harrat Rahat, and that these flows have broadly similar emplacement conditions to recent mafic lava flows at basaltic shield and stratovolcanoes. Our results help constrain the properties of recent eruptions in Harrat Rahat with implications for future eruptive behavior and hazards in this region.

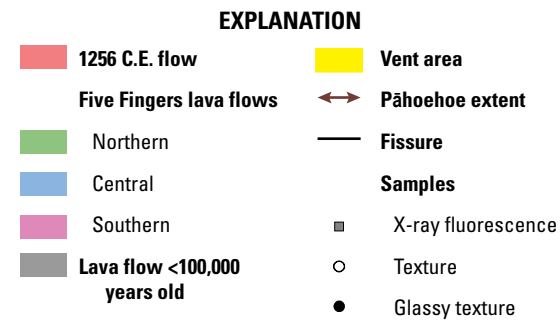
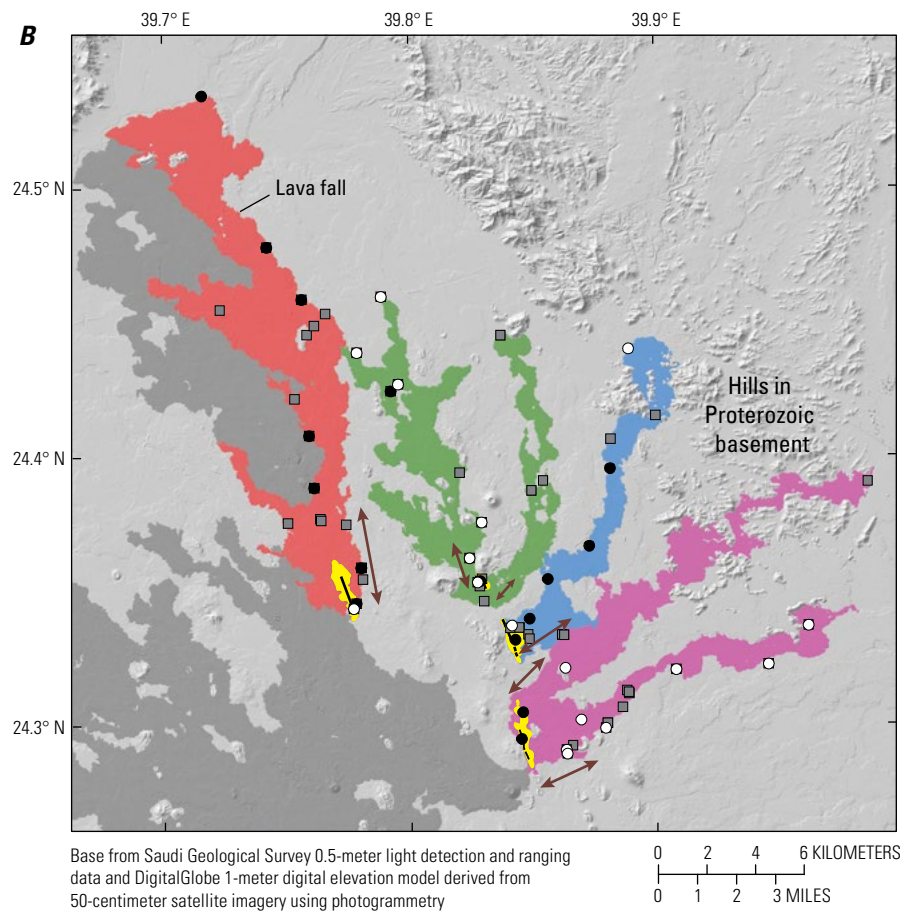
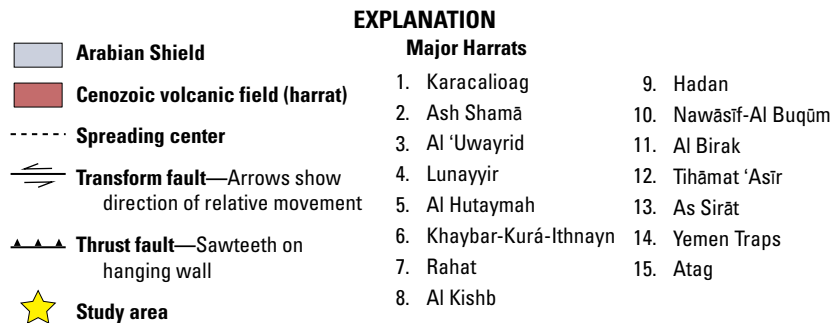
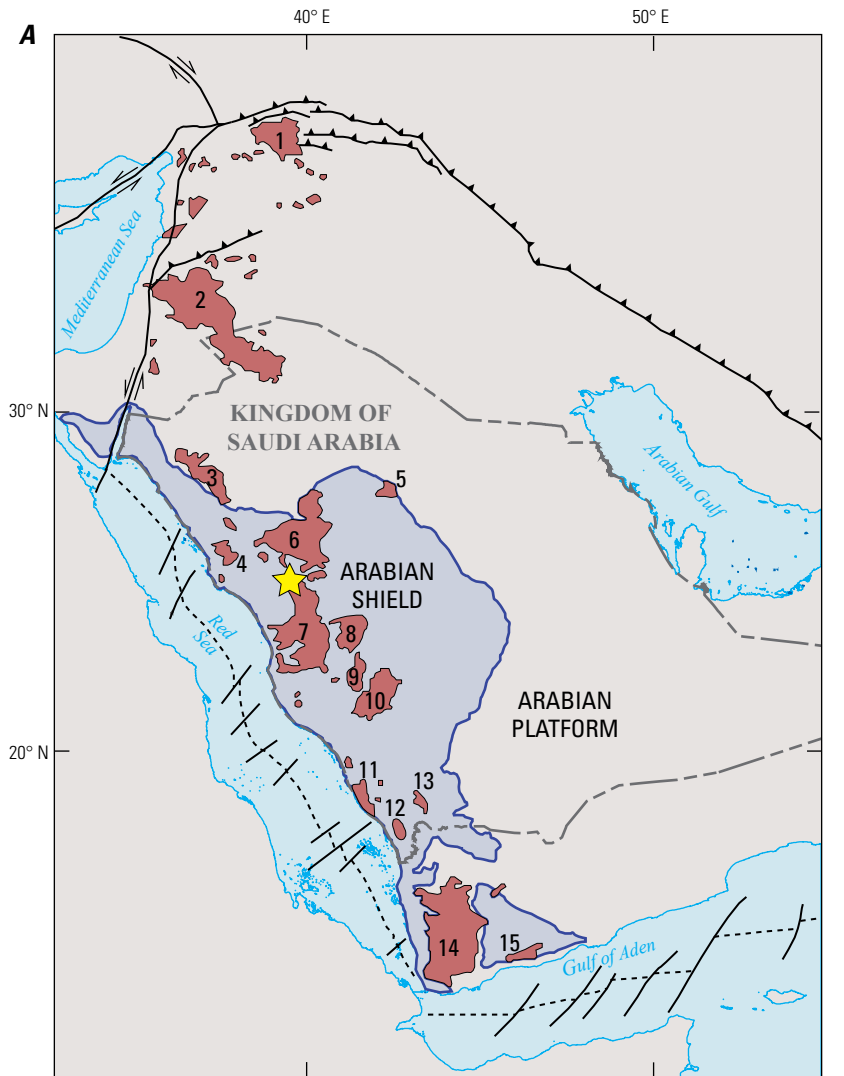
Geologic Setting

Harrat Rahat is one of more than 15 continental, intraplate volcanic fields stretching >3,000 kilometers (km) from the Gulf of Aden to the Mediterranean Sea (fig. 1A). Prior mapping has provided total eruptive volume estimates of ~2,000 cubic kilometers (km³), with mafic lava flows making up >95 percent

of the volcanic strata. The youngest eruptions are concentrated in the northernmost part of Harrat Rahat (Camp and Roobol, 1989, 1991; Moufti and others, 2012, 2013). New geologic mapping and geochronology have revealed eruption ages ranging from ≥1 million years old (Ma) to a single confirmed historical eruption in 1256 C.E. (654 in the year of the Hijra [A.H.]) (Camp and others, 1987; Moufti and others, 2013; Downs and others, 2018, 2019, 2023; Stelten and others, 2018, 2020, 2023). Lava flow emplacement in Harrat Rahat has not been investigated using quantitative analyses of morphology or rheology, but the site encompasses both historical and prehistoric flows, is covered by high-resolution topographic data, and has superb exposures with easy sample access, all of which make it an ideal setting to explore eruptive conditions of lavas in a mafic volcanic field.

The historical eruption in 1256 C.E. has been the main focus of previous lava flow emplacement studies in Harrat Rahat. Based on historical accounts, this eruption began on June 26, 1256 C.E. (Jumada-II 1, 654 A.H.), and lasted for 52 days (Al-Samhūdī, 1488). It formed seven scoria cones along a ~2.25-km-long fissure vent, which sent 0.0077 km³ of air-fall tephra to >5-km distance (Kawabata and others, 2015), and extruded ~0.4 km³ of chemically heterogeneous basalt, which flowed ~23 km from the vent (Camp and others, 1987) (figs. 1B and 2A). The products of this eruption are named the basalt of Al Labah on a new geologic map of the northern quarter of the volcanic field (Downs and others, 2018, 2019), and are also referred to as the Chada flow (Coleman, 1993), but are termed the 1256 C.E. flow field in this paper for simplicity (fig. 1B). Previous work on the geochemical evolution, surface morphology, and channel networks, as well as numerical modeling, has defined a series of six magma pulses that fed the eruption (Camp and others, 1987; Kereszturi and others, 2016). Although the 1256 C.E. eruption products have been described as encompassing alkalic and transitional compositions, all samples in the database of Downs and others (2019) are nepheline normative at concentrations of ferric and ferrous iron appropriate for probable magmatic oxygen fugacities (Sisson and others, 2023) and so are classified as alkalic. In the nomenclature from Walker (1971), this eruption produced a compound lava flow field with individual lava flow units. Chemical heterogeneity within the flow field was interpreted to be driven by magma mixing and persisted through the first three eruptive pulses (Camp and others, 1987). The bulk of the flow field was emplaced during the second pulse of the eruption and formed the main lava flow unit that consists of an ‘a’ā channel that extends north from the main vent (Camp and others, 1987). Detailed mapping by Kereszturi and others (2016) shows this branch of the flow transitioning from pāhoehoe to ‘a’ā at ~2 km from the vent (fig. 1B). Interaction with underlying topography resulted in lava ponding behind,

Figure 1 (page 3). Maps of the study area in the western part of the Kingdom of Saudi Arabia. *A*, Map of Harrat Rahat and other Cenozoic volcanic fields within the Arabia Plate. The yellow star locates the study area. *B*, Map of northeastern Harrat Rahat (yellow star in *A*) showing flows of interest, morphologic features, and sample locations. Flows shown in dark gray are those determined to be <100,000 years old on the basis of new ⁴⁰Ar/³⁹Ar radiometric and ³⁶Cl cosmogenic surface-exposure ages (Downs and others, 2019; Stelten and others, 2020, 2023). Basemap digital elevation from satellite photogrammetry (see [Methods](#) section).



and then eventually overtopping, a preexisting ridge ~16.5 km from the vent, forming a lava fall (fig. 1B; Camp and others, 1987; Kereszturi and others, 2016).

New geochronology and mapping of northern Harrat Rahat has identified late Pleistocene mafic eruptions, previously thought to be Holocene, that preceded the 1256 C.E. eruption (Downs and others, 2018, 2019, 2023; Stelten and others, 2018, 2020, 2023). The youngest of these, the basalt of Al Du'aythah (13.3 ± 1.9 ka), erupted small lava flows that extend less than 200 meters (m) (Murcia and others, 2015; Downs and others, 2018). However, prior to this was a period of eruptive activity that produced the lava flows dubbed the Five Fingers, which have five branches extending 13.2 to 20.2 km from their vents (fig. 1B). Based on mapped field relations, whole-rock chemistry, and phenocryst and microphenocryst characteristics, we subdivide the Five Fingers flows into the basalt of Northern Fingers, basalt of Central Finger, and basalt of Southern Fingers.

For simplification, these are termed the Northern, Central, and Southern flows in this chapter (fig. 1B). Past field interpretations have sometimes subdivided these into only two eruptive units (Moufti and others, 2013; Murcia and others, 2014) and estimated their ages as post-Neolithic (Camp and Roobol, 1989, 1991), although new surface-exposure ages reveal a weighted mean age of 24.4 ± 1.3 ka, with paleomagnetic studies suggesting that all three flows erupted within centuries of each other (Downs and others, 2019; Stelten and others, 2020; Champion and others, 2023). These flows are channelized 'a'ā flows with near-vent pāhoehoe extending as far as 2.5 km from the vent (figs. 1B and 2A–C). The Five Fingers flows can all be classified as simple after Walker (1971), although the Northern flow may be weakly compound as it has some late-stage overflows burying the main channels close to the vent (fig. 1B). Previous work by Murcia and others (2014) qualitatively described some of the surface morphology features and estimated volumes of

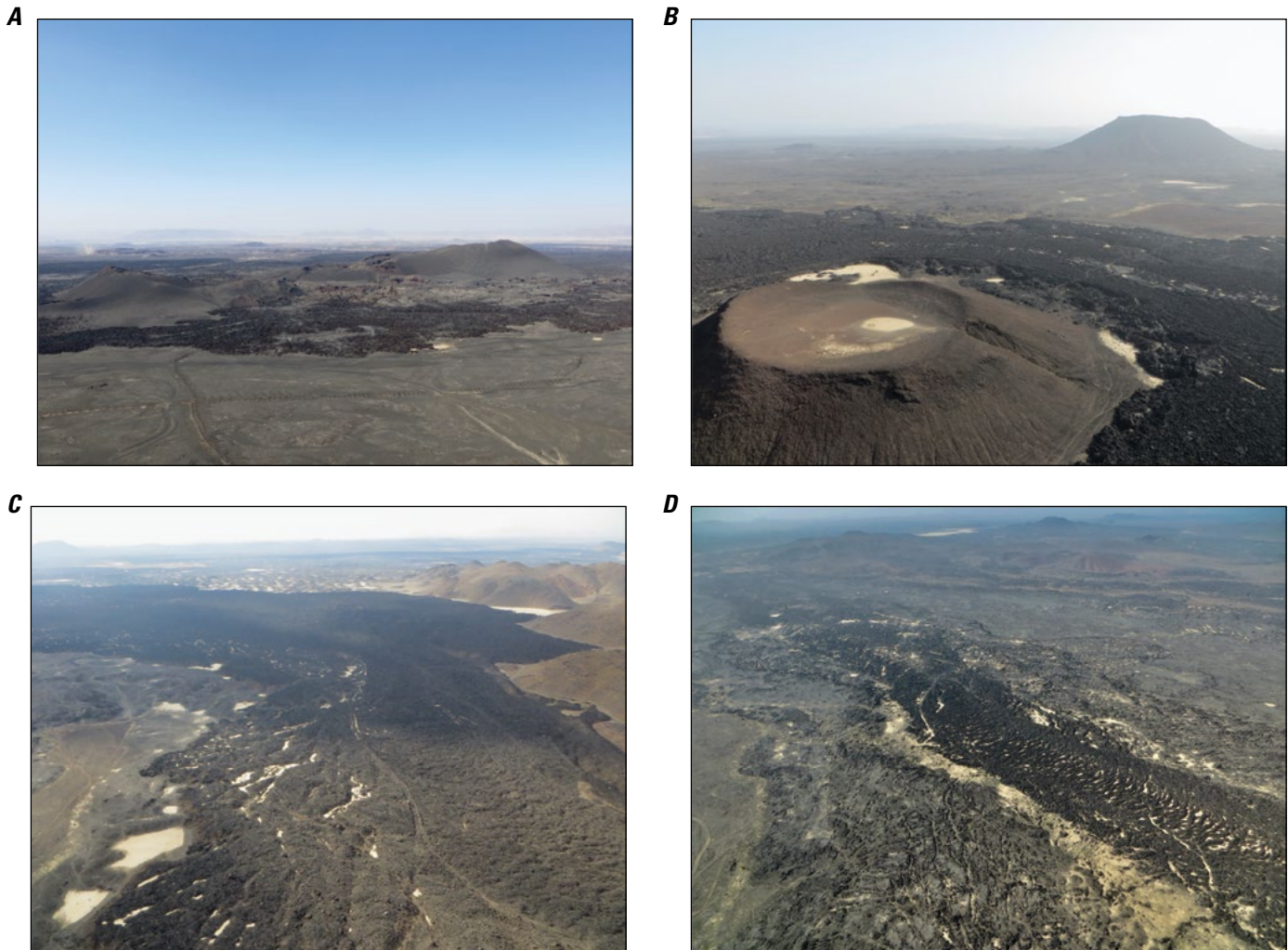


Figure 2. Photographs of studied lava flows in Harrat Rahat (fig. 1B). *A*, Photograph to the northwest showing the 1256 C.E. eruptive vents and near-vent pāhoehoe. The chain of cones from left to right is about 1.2 kilometers long. *B*, Photograph to the east-northeast showing the western channel of the Northern flow going around an undated Quaternary vent; the vent for the hawaiite of Al Malsa is visible in the distance (see Downs and others, 2019). Diameter of crater in lower left is 100 meters (m). *C*, Photograph to the west showing the Central flow as it intersects the hills composed of Proterozoic rocks. At its narrowest point in the bend, the flow is 160 m wide. *D*, Photograph to the west showing the south channel of the Southern flow with pāhoehoe levees near the vent. Channel width is 120–140 m. Photographs by Hannah Dietterich, U.S. Geological Survey, 2016.

these flows, but no quantitative work on flow morphology or rheology has been undertaken. Since the 1256 C.E. and Five Fingers lavas preserve the morphology and textures of the most recent effusive eruptions within northernmost Harrat Rahat, we focus our study on an investigation of the emplacement histories and properties of these flows.

Methods

Morphologic Analysis

A sufficiently high-resolution digital elevation model (DEM) to enable quantification of morphological properties, such as levee heights and channel widths, is fundamental for characterizing lava flow emplacement. We utilized several elevation datasets to achieve the highest possible resolution over our study area in northernmost Harrat Rahat (fig. 1B). Datasets included a 0.5-m-resolution light detection and ranging DEM from 2012 that encompasses the 1256 C.E. lava flow field, provided by the Saudi Geological Survey, and a 1-m-resolution DEM of the Five Fingers area purchased from DigitalGlobe and derived from satellite photogrammetry (using DigitalGlobe WorldView-2 50-centimeter-resolution visible imagery from December 9, 2012, and February 7–March 6, 2014). Vertical resolution of the DigitalGlobe DEM is about 0.1 m.

Flow and Channel Mapping

We used shaded-relief and slope maps derived from these DEMs to map the extents and morphology of lava flows. The

topographic data, in combination with the 50-centimeter-resolution WorldView-2 2012 and 2014 imagery, facilitated mapping channel margins along each flow (Downs and others, 2019). Channels are indistinct near the vent, where lavas are dominantly pāhoehoe (figs. 1B, 2A, and 2D), and distally, in the zone of dispersed flow and at the flow toe. We traced multiple sets of channel margins along the flows where they branched (for example, the Northern and Southern flows within the Five Fingers).

We analyzed these flow and channel extents using cross sections to quantify the evolution of flow and channel width down flow after Deardorff and Cashman (2012). Cross-section lines spaced every 100 m along the channel centerline were built using the HEC-GeoRAS software (U.S. Army Corps of Engineers, <http://www.hec.usace.army.mil/software/hec-georas>). To calculate channel and flow widths, we used a geographic information system-based method from Deardorff and Cashman (2012) that buffers each cross-section line by 50 m, both up flow and down flow, to create measurement boxes oriented perpendicular to the flow centerline and 100 m in the flow direction (fig. 3A). The total flow area within each cross-section box, divided by the 100 m box width, then represents the average flow width in this segment, whereas the narrower internal area between the channel margins is used to calculate average channel width.

Preeruptive Topography, Thickness, and Volume

High-resolution morphologic analysis also allows estimation of lava flow thicknesses and volumes. This is best done by comparing preeruptive and postemplacement topography

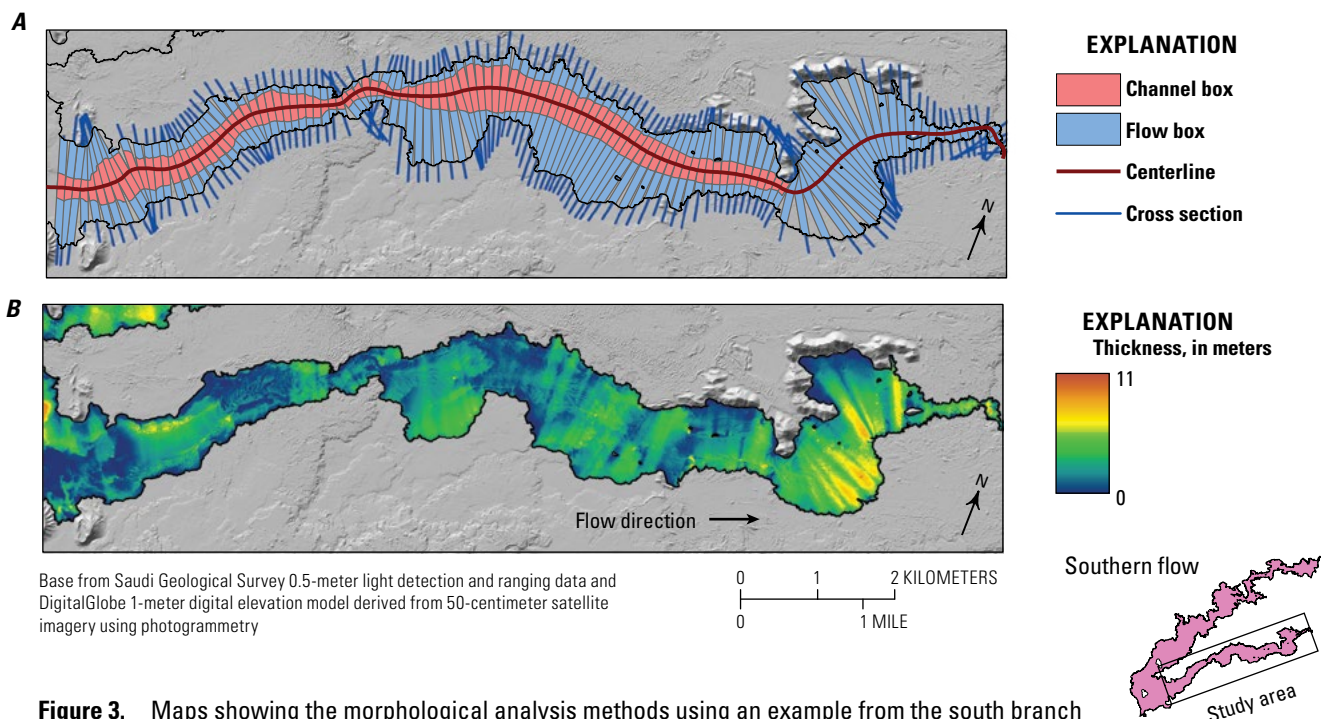


Figure 3. Maps showing the morphological analysis methods using an example from the south branch of the Southern flow (see fig. 1B for location). *A*, Planform morphology showing mapped flow and channel extents, flow centerline with cross sections, and the 100-meter-wide cross-section boxes. *B*, Flow thickness map constructed by subtraction of the reconstructed basal surface from present-day topography.

to derive a flow thickness map and integrating over the flow area to calculate volume (Mazzarini and others, 2005; Coltelli and others, 2007; Soldati and others, 2018). However, since preeruptive topographic information is lacking, we must use the present-day topography at the flow margins to interpolate an underlying surface.

One approach is to interpolate the basal surface using a triangulated irregular network connecting points along the flow margin, as was done for the 1256 C.E. flow field by Kereszturi and others (2016). However, we found that this method yields regions of significant negative thicknesses for these lava flows, as Kereszturi and others (2016) noted. To avoid this, we allowed preeruptive elevations within the flow to be lower than the flow margins by using flow cross sections and inserting additional points where required, similar to the method of Stevens (2002). We used the same cross sections as for morphologic analysis, but along the full flow length, and extracted their elevations. For cross sections where the surface of the lava flow was everywhere higher than the elevation at the margins, the base of the flow was modeled using a straight line between the end points along opposite flow edges. Where the lava flow surface was lower in elevation than that of the margins, the base was defined by the minimum number of line segments that intersect interior low points along the cross section, requiring a minimum thickness of 0.2 m based on our field observations (fig. 4). The base of the entire flow was then constructed with a natural neighbor interpolation of all the

basal cross sections and then subtracted from the elevation of the flow top to obtain flow thicknesses and volumes (fig. 3B). These thicknesses and volumes likely represent minimum estimates, with potential thickness underestimates on the order of a few meters where flows are strongly confined by topography. The result has artifacts from the cross-section locations, so we calculated average thicknesses within the cross-section boxes described above to smooth the results and for comparison with other morphology metrics.

Finally, we measured the slope of the channel surface and the entire flow, as well as its interpolated base, using the same cross-section boxes. The averaged slopes of the flow-top segments were calculated after Deardorff and Cashman (2012) by fitting a planar surface to the portion of the DEM within the lava channel in each box and extracting its topographic gradient. Test datasets were also made using the interpolated flow base from the thickness calculations and the full flow area, instead of the channel. However, the slope of the interpolated base and the full flow area were much noisier than the slope extracted from within the channel, with artifacts from the cross-section spacing in the interpolated surface and disruption from the morphology of the levees and overflows within the full area of the flow. We therefore used the present-day channel surface to calculate the slope, which succeeds in capturing changes in slope, such as the lava fall, in the 1256 C.E. flow, but is limited to the channel extent and is only a best approximation of the preeruptive slope.

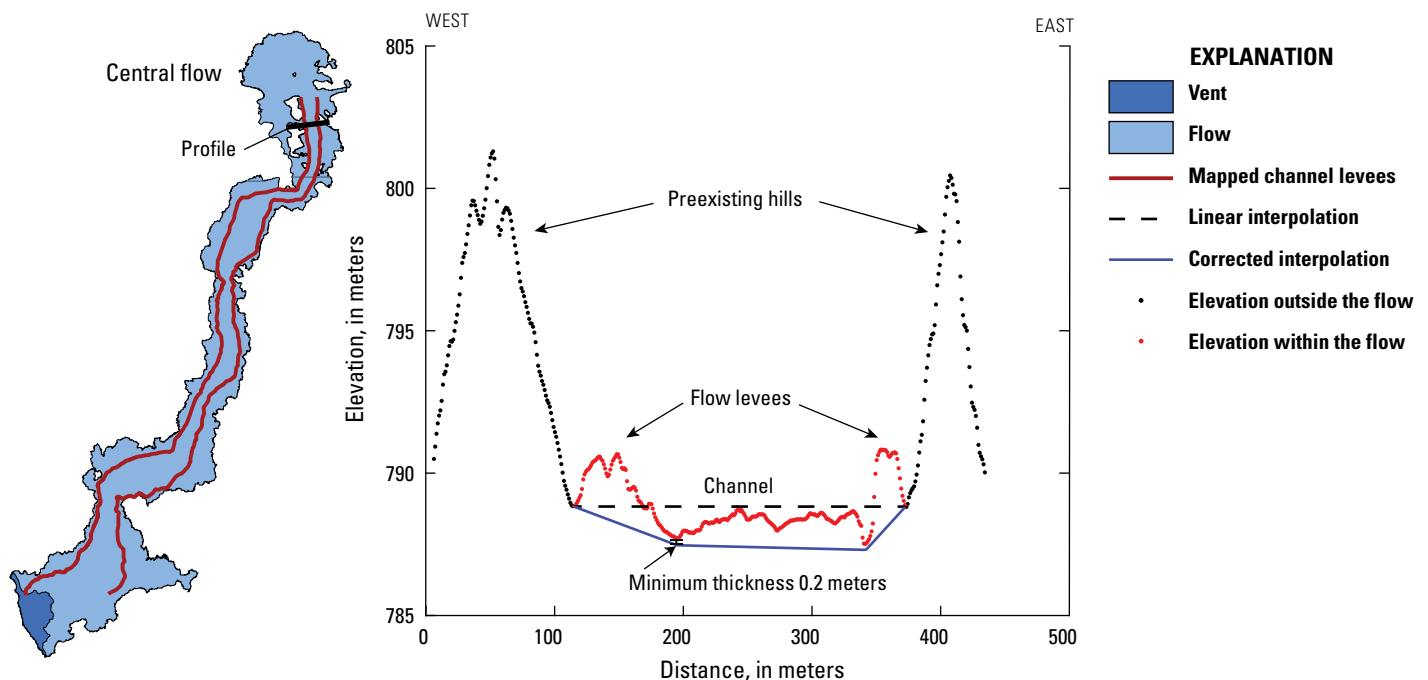


Figure 4. Example of the profile interpolation method used for thickness measurements. The map shows the vent area, flow extent, and mapped channel levees of the Central flow (see fig. 1B for location). The cross section shows the profile near the flow toe (trace shown on map). Here the flow is confined in a valley (high elevation spikes in cross section) with a set of levees on the margins of the lower channel surface. The black dashed line is the initial linear interpolation of the preeruptive surface based on the elevations at the flow margin. The interpolation erroneously lies above the flow surface in many places. The blue line shows the linear interpolation corrected to the flow surface, preventing negative values of thickness and requiring a minimum thickness of 0.2 meters.

Table 1. Representative whole-rock chemical analyses of the 1256 C.E. and Five Fingers lava flows, northern Harrat Rahat.

[Major-oxide concentrations were measured by X-ray fluorescence. Values have been recalculated to 100 weight percent anhydrous, but original loss on ignition (LOI) and totals are given. All iron content reported as FeO (FeO*). See [appendix 1](#) for sample details. Values are in weight percent]

Sample name	SiO ₂	TiO ₂	Al ₂ O ₃	FeO*	MnO	MgO	CaO	Na ₂ O	K ₂ O	P ₂ O ₅	LOI	Total
1256 C.E. flow												
R14AC056	46.9	2.97	16.0	12.7	0.22	6.35	8.80	4.19	0.95	0.97	0.00	99.1
R15DD150A	46.8	1.83	16.2	11.4	0.18	8.98	11.3	2.76	0.32	0.20	0.00	99.0
R14TS012	46.8	3.00	16.1	13.0	0.22	6.05	8.67	4.23	0.97	1.02	0.00	99.7
R14TS093	46.7	3.00	16.0	13.1	0.22	6.02	8.60	4.31	0.99	1.05	0.00	99.8
R14TS096	46.8	3.02	16.1	12.8	0.22	5.95	8.73	4.26	0.99	1.05	0.00	99.7
R14TS097	47.0	3.01	16.3	13.0	0.22	5.93	8.46	4.12	0.99	1.03	0.00	99.6
R14TS098	46.5	2.10	16.0	11.5	0.18	9.47	10.5	3.00	0.43	0.30	0.00	99.2
R14TS100	46.9	3.07	16.2	12.9	0.22	5.96	8.54	4.26	1.00	1.06	0.00	99.5
R14TS102	47.0	3.05	16.2	13.0	0.22	6.00	8.35	4.19	0.98	0.94	0.00	99.4
R14TS103	46.9	3.02	16.1	12.9	0.22	6.03	8.59	4.26	0.99	1.05	0.00	99.9
R14TS104	46.7	3.04	16.0	13.1	0.22	6.01	8.50	4.28	1.02	1.08	0.00	99.5
R14TS142	46.6	1.99	16.7	11.6	0.18	8.64	10.8	3.02	0.38	0.24	0.00	100.0
Northern flow												
R15DD011	45.9	3.68	16.4	13.1	0.19	6.49	9.49	3.55	0.82	0.40	0.00	99.7
R15DD018	45.8	3.46	16.0	12.8	0.19	7.40	9.80	3.45	0.82	0.39	0.98	98.4
R14DS079	45.8	3.61	16.3	13.0	0.19	6.88	9.25	3.81	0.84	0.40	0.00	99.1
R14DS082	45.8	3.64	16.4	13.0	0.19	6.79	9.27	3.83	0.81	0.39	0.00	99.6
R15DS097	45.9	3.74	16.5	13.2	0.21	6.58	9.04	3.53	0.81	0.44	0.00	99.1
R15DS099	45.9	3.63	16.4	12.9	0.19	6.78	9.39	3.61	0.78	0.40	0.00	100.0
R15DS100	45.8	3.64	16.4	13.2	0.20	6.52	9.33	3.65	0.83	0.41	0.00	99.8
R14TS017	45.3	3.65	16.3	13.2	0.19	6.58	9.67	3.93	0.82	0.40	0.87	98.4
R14TS019	45.9	3.72	16.5	13.4	0.20	6.73	8.77	3.57	0.81	0.41	0.00	99.0
R14TS020	45.9	3.68	16.5	13.2	0.19	6.66	9.12	3.56	0.81	0.39	0.00	98.8
Central flow												
R14AC008	45.8	3.44	16.0	13.2	0.19	7.61	9.07	3.58	0.75	0.32	0.00	100.0
R14AC009	45.3	3.48	15.8	13.2	0.18	7.51	9.73	3.69	0.77	0.33	0.00	98.9
R14TS011	45.4	3.63	16.3	13.2	0.22	6.94	9.39	3.55	0.82	0.56	0.24	98.7
R14TS024	45.8	3.65	16.3	13.3	0.20	7.14	8.92	3.54	0.79	0.42	0.00	99.2
R16MS071	45.9	3.65	16.3	13.2	0.19	6.81	9.13	3.61	0.87	0.39	0.00	99.4
Southern flow												
R14AC005	46.2	2.36	15.7	12.0	0.18	8.88	11.1	2.93	0.43	0.24	0.00	98.9
R14AC006	46.0	2.35	15.9	12.0	0.18	8.57	11.4	2.95	0.44	0.23	0.03	99.6
R14AC007	46.1	2.49	15.9	12.3	0.18	8.82	10.6	2.96	0.47	0.26	0.00	99.8
R15DD019	46.0	2.32	15.9	11.8	0.19	8.92	11.4	2.77	0.45	0.26	0.46	99.6
R15DD022	46.2	2.36	16.1	11.9	0.18	8.79	11.1	2.76	0.38	0.24	0.00	99.6
R15DD025	46.2	2.30	15.7	11.5	0.18	8.64	12.1	2.76	0.44	0.24	0.91	98.7
R15DS101	46.6	2.36	15.8	11.9	0.18	8.97	10.6	2.92	0.44	0.22	0.00	98.6
R15DS105	46.2	2.34	15.9	12.2	0.18	8.75	11.0	2.81	0.43	0.24	0.00	99.4
R14TS008	46.0	2.34	15.7	12.2	0.18	8.93	11.2	2.77	0.43	0.24	0.00	99.4
R14TS026	46.1	2.48	16.2	11.6	0.21	8.48	11.2	2.84	0.53	0.36	0.81	99.0

Geochemical and Textural Analysis

To characterize the whole-rock compositions of the 1256 C.E. and Five Fingers eruptive products, we collected and analyzed 37 scoria and lava samples from throughout these units (squares in [fig. 1B](#); [table 1](#); [appendix 1](#)). Major-oxide analyses were performed by X-ray fluorescence at the GeoAnalytical Laboratory at Washington State University.

Another set of 35 samples was collected for textural analysis down flow from vent to toe at flow levees, with an effort to select samples that preserve original air-quenched textures, including near-vent tephra (circles in [fig. 1B](#); locations in [appendix 2](#); sampling methods after Crisp and others, 1994; Riker and others, 2009; Robert and others, 2014). Despite field selection of glassy samples, thin section analysis revealed that only 16 samples preserved significant glass appropriate for textural and chemical analyses (black circles in [fig. 1B](#)). We restricted our geochemical and textural interpretations to the glassy margins of these samples.

We used a JEOL JXA-8900 wavelength-dispersive electron microprobe to measure the chemistry of minerals and glass as a record of the syneruptive state of the lava. We used a 15 kilovolt accelerating voltage for all analyses and a current of 5 nanoamperes (nA) and a 5 micrometer (μm) spot size for glass, a current of 10 nA and a 5 μm spot size for plagioclase microphenocrysts, and applied 30 nA with a focused beam for olivine microphenocrysts. The instrument was standardized on a selection of natural and synthetic glasses and minerals, and background-corrected X-ray count rates were converted to oxide concentrations, in weight percent, with the JEOL proprietary version of the CITZAF reduction scheme (Armstrong, 1995).

Textural data were derived from Tescan Vega3 scanning electron microscope backscattered electron images at a range of magnifications (10–800 \times , 10–30 images per sample). We mosaicked images and postprocessed these with threshold ranges to make each phase a uniform grayscale color (after Shea and others, 2010). Postprocessed images were analyzed using ImageJ to calculate phase proportions and crystal shapes. We measured crystal aspect ratios only for crystals that have areas larger than 10^{-5} square millimeters (mm^2) to reduce the influence of pixel-scale noise, and we corrected for stereological effects after Higgins (2000).

Characterization of Lava Temperature, Viscosity, and Effusion Rate

To reconstruct eruptive conditions, we first independently characterized lava viscosity petrologically and then combined these viscosities with the morphology metrics to assess effusion rates. We calculated lava viscosity as a function of the liquid viscosity and the effects of crystallinity and vesicularity (methods after Costa, 2005; Llewellyn and Manga, 2005; Giordano and others, 2008; Costa and others, 2009; Mueller and others, 2011; Mader and others, 2013). Effusion rates were then estimated from these viscosities, as well as channel width

and topographic slope, using a model of channel formation in solidifying viscous flows from analytical theory and experiments by Kerr and others (2006).

Geothermometry

Lava viscosity is strongly controlled by its temperature and this can be calculated from the compositions of coexisting mineral phases (Shaw, 1972; Crisp and others, 1994; Giordano and others, 2008; Putirka, 2008). We applied a suite of geothermometers based on liquid chemistry, olivine-liquid equilibrium, and plagioclase-liquid equilibrium from Helz and Thornber (1987), Beattie (1993), Sisson and Grove (1993), Montierth and others (1995), Putirka and others (2007), and Putirka (2008). Each geothermometer assumes that phases are in equilibrium and some use estimates of dissolved water content and pressure (see Putirka, 2008, for a review). We used VolatileCalc (Newman and Lowenstern, 2002) to model water content at atmospheric pressure and measured glass SiO_2 concentrations. Temperatures derived from glass-rich samples are taken to be those at the time the flows were actively emplacing at the sample locations.

Viscosity

The viscosity of the bulk lava is influenced by the viscosity of the liquid phase, as well as its crystallinity and vesicularity (Llewellyn and Manga, 2005; Giordano and others, 2008; Costa and others, 2009; Mueller and others, 2011; Mader and others, 2013). To calculate the mixture viscosity, we computed the liquid viscosity, added the relative effect of crystals on the bulk viscosity, and then assessed the impact of the vesicle fraction.

We model the apparent bulk viscosity (η_{app}) of our samples as a function of the viscosity of the residual liquid (η_{liq}) and the relative viscosity based on the crystal or vesicle content (η_r)

$$\eta_{app} = \eta_{liq} \eta_r. \quad (1)$$

We calculated liquid viscosity (η_{liq}) from glass compositions and calculated temperatures using the model of Giordano and others (2008). Viscosity is highly sensitive to H_2O dissolved in the melt, we applied our water content estimates at atmospheric pressure from VolatileCalc based on the glass compositions (Newman and Lowenstern, 2002).

The relative viscosity (η_r) can be estimated from a variety of different models to account for the effects of the solid fraction. Crystallinities were adjusted for analysis to exclude the volume fraction of bubbles by normalizing the crystal fraction to the vesicle-free (melt + crystals) fraction (Mader and others, 2013; Robert and others, 2014; Soldati and others, 2018). In the first model, from Mueller and others (2011), all particles are treated as identical and have the shape of the observed crystals. Elongate particles reduce the effective maximum packing volume fraction of the particles (ϕ_m) following a relation derived experimentally by Mueller and others (2011)

$$\phi_m = \phi_{m_i} \exp \left[-\frac{(\log_{10} r_p)^2}{2b^2} \right], \quad (2)$$

where r_p is the crystal aspect ratio, ϕ_{m_i} is the maximum packing fraction for particles with $r_p = 1$, and b is the variance of the log-Gaussian function. We used the observed crystal aspect ratio and the best-fit values of ϕ_{m_i} and b for natural crystals (Mader and others, 2013) to calculate the maximum packing fraction (ϕ_m). As the crystallinity (ϕ) increases with cooling, and approaches this value, the relative viscosity (η_r) will rise rapidly following the relation of Maron and Pierce (1956)

$$\eta_r = \left(1 - \frac{\phi}{\phi_m} \right)^2. \quad (3)$$

This model can describe the evolution in apparent viscosity at low crystal fraction, but becomes infinite at the maximum packing fraction, whereas lavas are still capable of deformation at higher crystal contents (Costa, 2005; Mader and others, 2013; Bergantz and others, 2017).

We therefore extend our analysis using a second model from Costa (2005) and Costa and others (2009) that seeks to capture behavior at any crystal fraction. This model determines relative viscosity as a function of strain rate because the rheology of crystal-rich flows is likely non-Newtonian (Castruccio and others, 2014). Relative viscosity (η_r) as a function of crystal fraction (ϕ) is calculated as:

$$\eta_r = \frac{\left(1 + \frac{\phi}{\phi_*} \right)^\delta}{\left[1 - F \left(\frac{\phi}{\phi_*}, \xi, \gamma \right) \right]^{B\phi}}, \quad (4)$$

where

$$F = (1 - \xi) \operatorname{erf} \left[\frac{\sqrt{\pi}}{2(1 - \xi)} \frac{\phi}{\phi_*} \left(1 + \frac{\phi^\gamma}{\phi_*^\gamma} \right) \right] \quad (5)$$

and where ϕ_* is the critical crystal fraction when crystal interactions dominate the rheology, γ is a parameter that reflects how rapidly viscosity changes as ϕ approaches ϕ_* , δ controls the viscosity change when ϕ exceeds ϕ_* and $\delta = 13 - \phi_*$ after Costa and others (2009), B is the Einstein coefficient, and ξ sets the values of η_r when ϕ equals ϕ_* . The parameters for this model must be determined experimentally and we use values from Cimarelli and others (2011) that best reflect the Harrat Rahat crystal aspect ratio (r_p). Since the fit parameters are also a function of strain rate, we calculate values for two different strain rates (10^{-4} and 1 per second [s^{-1}]). At low crystal fraction, equations 4 and 5 approximate equation 3.

We also estimated the effect of the vesicle fraction following Llewellyn and Manga (2005) and Mader and others (2013) to account for the addition of vesicles to the melt-plus-crystals mixture. The modeled effect of the vesicle fraction

varies with strain rate and vesicle size, so we test two different strain rates (10^{-4} and $1 s^{-1}$) and use an average bubble radius of 0.01 millimeters (mm) following Llewellyn and Manga (2005) and Mader and others (2013).

Estimation of Effusion Rates

Analytical theory, analogue experiments, and observations of eruptions suggest that lava channel geometry is controlled by effusion rate, underlying slope, and flow rheology (Hulme, 1974; Harris and Rowland, 2001; Kerr and others, 2006). In flows that are cooling and growing a surface crust, crustal growth and lateral flow spreading will balance at a given volumetric flux, viscosity, and slope to develop a channel of constant width (Kerr and others, 2006). Following Kerr and others (2006), the relation between parameters can be written as an equation for flow width, w ,

$$w = 2 \left[\frac{(g\Delta\rho)^2 Q^7 \eta^4 \cos^9 \theta}{\sigma_c^6 \kappa^3 \sin^7 \theta} \right]^{1/13} \quad (6)$$

where

g	is gravity,
$\Delta\rho$	is density of the flow relative to its environment,
Q	is volumetric flux through the channel,
η	is viscosity,
θ	is slope,
σ_c	is crustal yield strength, and
κ	is thermal diffusivity.

We use a value of 2,400 kilograms per cubic meter (kg/m^3) for bulk flow density for these low-vesicularity basalts (Shea and others, 2010; Downs and others, 2018). Values for σ_c range from 10^4 to 10^6 pascals (Pa) and a value of 10^{-6} square meters per second (m^2/s) for κ is most commonly used for basalt (Blake and Bruno, 2000; Kerr and others, 2006; Kerr and Lyman, 2007; Deardorff and Cashman, 2012; Cashman and others, 2013; Castruccio and others, 2013). The volumetric flux of lava through the channel derived from this equation provides an estimate of the average local effusion rate through the whole channel while it was active.

The crustal yield strength is typically calculated by fitting this model to flow advance data (Blake and Bruno, 2000; Kerr and others, 2006; Kerr and Lyman, 2007; Castruccio and others, 2013), however we lack such observations for these eruptions. We therefore calculate a best-fit value for σ_c for the Harrat Rahat basalts by fitting equation 6 to parameters for the 1256 C.E. eruption, which is the only eruption for which we have an independent estimate of effusion rate from the observed total mean output rate of the eruption (total volume divided by total duration). This assumes that the channel morphology represents flow at the average local effusion rate through the channel during the eruption (eq. 6). Instantaneous effusion rates would be higher or lower as the eruption waxed and waned, but using the constraint of the total mean output rate offers an educated, if uncertain, estimate for this parameter for the 1256 C.E. flow.

We adopt this crust-dominated model for flow emplacement and channelization to estimate the effusion rates that formed the observed ‘a’ā channel morphology after Kerr and others (2006) and Deardorff and Cashman (2012). This regime assumes a flow with a core viscosity, retarded by a growing surface crust, rather than an evolving bulk rheology. We lack flow advance data to fully test for crust-dominated behavior or discard alternatives, but analyses of similar flows in the literature support the application of this model (Kilburn and Lopes, 1991; Kerr and others, 2006; Lyman and Kerr, 2006; Castruccio and others, 2013). We therefore use our calculations of apparent viscosity to constrain the core viscosity, averaging apparent viscosities in log space to capture values with intermediate crystallinity and temperature. We exclude samples with crystallinities greater than the maximum packing fraction in our averages because they are unlikely to represent the insulated flow interior beneath the surface crust. Using the method of Deardorff and Cashman (2012), we combine these core viscosities with the slope and width measurements from morphologic analysis to fit equation 6 to our data and calculate the best-fit volumetric flux through each channel. The results represent the best-fit local effusion rate during channelized flow, which we use as an approximation of the average effusion rate for the emplacement of each flow branch.

Results

Whole-Rock Geochemistry

Whole-rock major-oxide compositions are summarized in table 1. Our data, and those of previous workers, show that the 1256 C.E. eruption produced variably alkalic compositions, as well as hybrids interpreted as mixtures of two or more end members. A similar conclusion was reached by Camp and others (1987). The Five Fingers lavas all consist of alkalic basalt typical of Harrat Rahat volcanism (Downs and others, 2019), but each of the three eruptions that make up the Five Fingers are compositionally distinct. For a complete list of Harrat Rahat geochemical analyses, see Downs’ (2019) data release.

Morphologic Analysis

Morphology measurements are summarized for all flows and branches in fig. 5A–L and table 2. Field contacts allow us to distinguish the boundaries between the Five Fingers flows. The Central flow was the first of the Five Fingers to erupt based on stratigraphic relations, but it is unknown if the Northern or Southern flows erupted second, as their lava flows are not in contact. The channel networks are mostly simple, where

Table 2. Flow and channel morphology results for northern Harrat Rahat flows.

[Volume estimates are likely minimums because of the lack of preeruptive topography. Flow lengths are measured along the main channel from vent to toe. Errors are standard errors. The full range of values are shown in figure 5. km³, cubic kilometer; DRE, dense rock equivalent; km, kilometer; m, meter; kg/m³, kilogram per cubic meter]

Flow	Vent volume (km ³)	Flow volume (km ³)	Total volume DRE ¹ (km ³)	Flow length (km)	Mean flow thickness (m)	Mean flow width (m)	Mean channel width (m)	Mean slope (degree)
1256 C.E. flow								
1256 C.E. flow	0.02	0.44	0.42	21.8	7.7±0.2	1,403±61	329±18	0.80±0.06
Northern flow								
West branch		0.14		14.3	6.3±0.2	888±49	165±6	0.72±0.06
East branch		0.04		13.2	3.6±0.1	728±23	194±9	0.75±0.06
Whole flow	0.01	0.18	0.17	14.3				
Central flow								
Central flow	0.01	0.07	0.07	15.7	3.8±0.2	978±34	436±19	0.67±0.04
Southern flow								
North branch		0.09		20.2	3.4±0.1	924±38	276±8	0.54±0.03
South branch		0.05		16.6	2.2±0.1	791±26	346±11	0.65±0.04
Whole flow	0.01	0.14	0.13	20.2				

¹DRE volume calculated using 2,600 kg/m³ for dense rock, 2,400 kg/m³ for lava, and 1,500 kg/m³ for tephra.

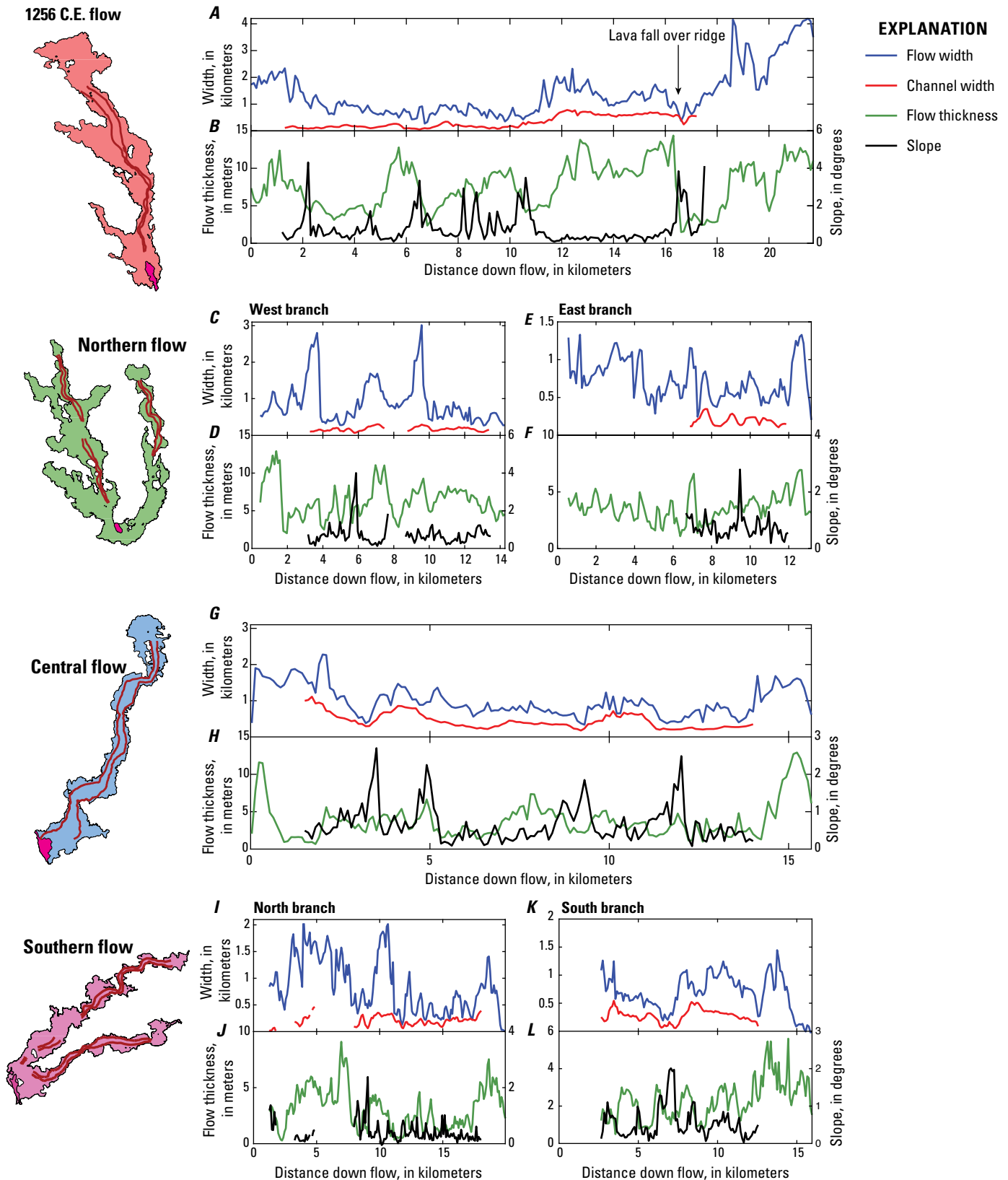


Figure 5. Plots of morphometric data derived along each lava flow. For each lava flow, flow and channel width are shown in the upper plots (A, C, E, G, I, and K) and flow thickness and slope are shown in the lower plots (B, D, F, H, J, and L). Channel width and slope are only calculated where the channel is well defined (fig. 3). Mapped channel levees are shown as red lines in the flow maps at left.

each branch contains a single channel. Where levees are well defined, they stand 1 to 6 m above the channel floor, but it is not possible to trace the levees along the entire flow length because of burial by proximal pāhoehoe and later overflows (compare with Robert and others, 2014). No channels are present within the zone of dispersed flow near the flow toes. Distally, the Central flow and the north branch of the Southern flow advanced through hills consisting of Proterozoic rocks to the east, where they were confined in narrow valleys (figs. 1B and 2C; Camp and Roobol, 1989). The 1256 C.E. flow has a more complex branched network (Camp and others, 1987; Kereszturi and others, 2016), and for channel and flow morphology metrics we extracted only the main channel from the second pulse of the eruption, which was by far the largest in volume (Camp and others, 1987). This channel extends from the vent to the most distal flow toe (fig. 5A–B). The flows vary in size considerably; minimum bulk-flow volumes range from 0.07 km³ for the Central flow to 0.44 km³ for the 1256 C.E. flow (table 2). As expected, flow thickness and slope show an inverse relation (compare with Walker, 1973). There is evidence of flow thickening upslope of large slope increases, particularly in the 1256 C.E. flow field at ~16 km down flow where the lava ponded above the lava fall at ~16.5 km identified by Camp and others (1987; figs. 1B and 5B).

Petrologic Analysis

Major-oxide glass and mineral compositions averaged for each sample are presented in table 3 with complete results in appendix 3. Variations in composition across the flow fields show glass SiO₂ concentrations ranging from 44 to 49 weight percent, plagioclase spanning anorthite content An₅₆ to An₇₁, and olivine spanning forsterite content Fo₆₇ to Fo₈₃. Glass Al₂O₃ and MgO concentrations both decrease slightly with distance down flow, whereas K₂O concentration increases, consistent with crystallization with emplacement time and cooling away from the vent. The lack of quenched samples from the Northern and Southern flows prevents detailed analysis of their down-flow evolution. We therefore use available data to provide estimates of the textural and rheological parameters for these flows, but only make interpretations of down-flow changes based on the flows with more complete datasets (in other words, for the 1256 C.E. and Central flows).

Textural analysis yields variations in crystallinity and vesicularity. Proportions of crystals from image analysis show crystallinity increasing down flow. Analysis of vesicles reveals high vesicularity for air-fall tephra and spatter (32 percent on average), and low vesicularity for lava samples (6 percent on average; fig. 6A–B). Plagioclase dominates the crystal fraction, but we identify olivine and Fe-Ti oxides in nearly all samples (table 4). We assign an uncertainty of 2 percent to these phase proportions to account for textural variability within the samples based on analyses of subsamples of images. Crystals with areas greater than 10⁻⁵ mm² are euhedral and have broad-peaked distributions in aspect ratio in two-dimensional intersection, indicative of three-dimensional aspect ratios of ~3.5 for plagioclase and

~2 for olivine (Higgins, 2000). A majority of samples contain sparse (<1 percent) resorbed phenocrysts of 0.5 to 2 mm plagioclase and olivine.

Analysis of Emplacement Conditions

Thermometry

We average results from all of the individual geothermometers to derive lava temperatures for each sample (table 4; full results in appendix 6). Calculated dissolved H₂O concentrations used for geothermometry were 0.08 to 0.09 weight percent H₂O based on glass compositions at 1 bar (Newman and Lowenstern, 2002), consistent with the high microprobe totals for glass analyses (table 3). Our results capture near-vent temperatures for the flows of 1,120 to 1,150 degrees Celsius (°C) (table 4). Results from the 1256 C.E. and Central flows show an overall cooling trend with distance from the vent (fig. 7), with lava temperatures dropping from ~1,140 to ~1,090 °C over 9 to 20 km, giving cooling rates of 2 to 7 °C/km. Limited data from the Northern and Southern flows preclude any interpretation of temperature trends (fig. 7). Although the 1256 C.E. flow is chemically diverse (tables 1 and 3), the least alkalic sample analyzed (R15DD150B) shows temperatures within the same range as the other samples (1,139±6 °C).

Viscosity

Melt viscosities calculated with the model from Giordano and others (2008) increase with cooling down flow, and range from 10² to 10³ pascal seconds (Pa·s) (table 4). To add the effect of the crystal fraction after Mueller and others (2011), the average Harrat Rahat crystal aspect ratio (r_p) of 2.7 yields a maximum packing fraction (ϕ_m) of 0.50 from equation 2. Integrating results from equations 1–3, the apparent viscosities of the Harrat Rahat lavas were on the order of 10² to 10³ Pa·s near the vent and increased by nearly three orders of magnitude with distance down flow for the well-sampled 1256 C.E. flow (fig. 8, solid lines; table 4).

Viscosities at higher crystal fractions are derived from the model of Costa (2005) and Costa and others (2009) shown in equations 4 and 5. Using experimentally derived parameters from Cimarelli and others (2011) that best match the Harrat Rahat crystal aspect ratio (type C in their paper with $r_p=1.82$), results follow the Mueller and others (2011) dilute mixture model until the crystallinity reaches maximum packing (fig. 8; table 4). Lower values at the higher strain rate (1 s⁻¹) demonstrate that the flow underwent shear thinning at very high crystallinities (Mader and others, 2013), but the effect of strain rate on apparent viscosity was small relative to changes in temperature and crystallinity. Viscosities ranged from 10² to 10⁹ Pa·s with vesicle-free crystallinities between 1 and 65 volume percent (table 4). Although the 1256 C.E. and Central flows show viscosity increased with distance from vent (fig. 8), sampling of the Northern and Southern flows is not complete enough to show unambiguous trends.

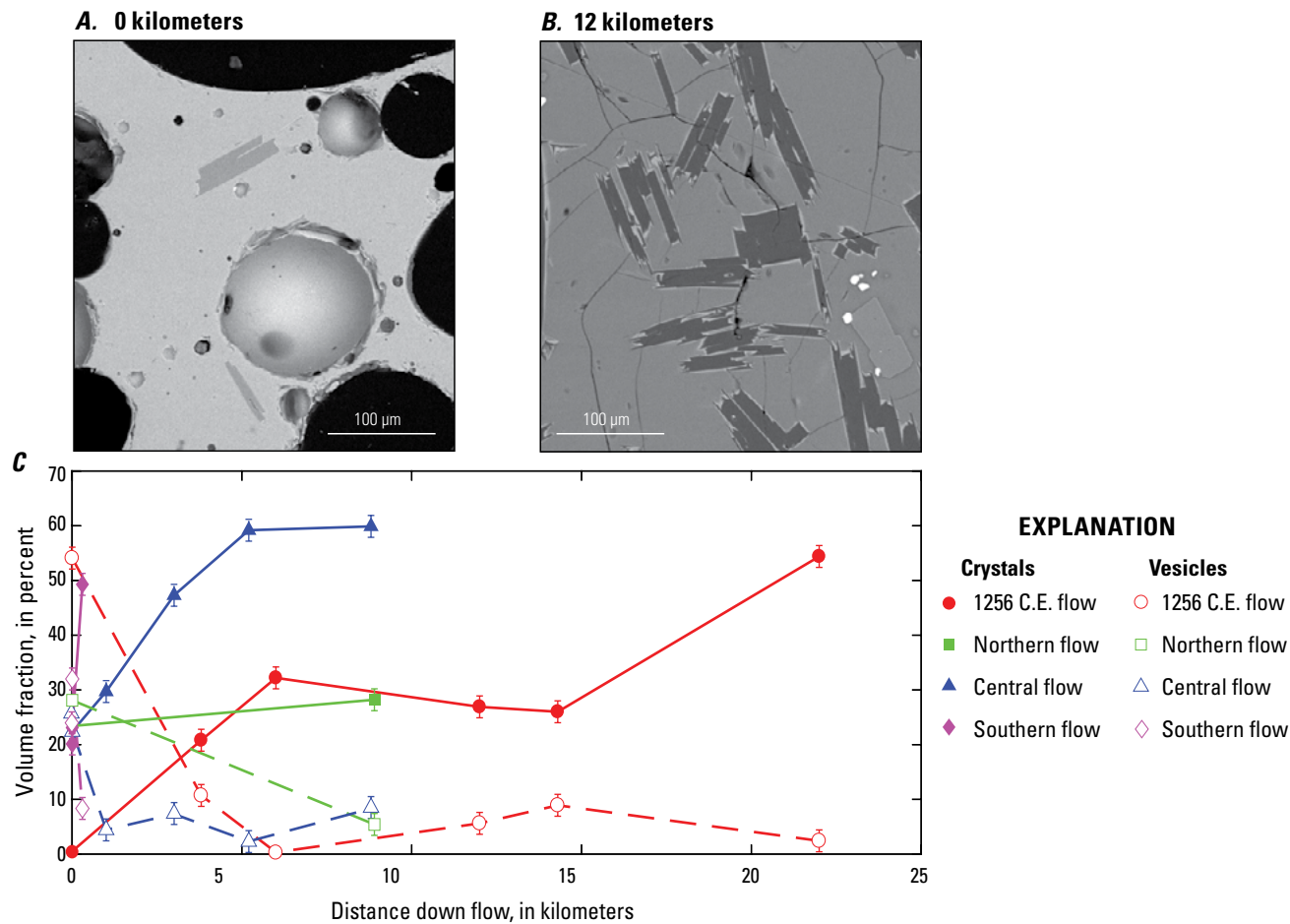


Figure 6. Plot of textural changes with distance down flow. Scanning electron microscope backscattered electron images showing textures in the 1256 C.E. flow (A) at the vent (0 kilometers [km]) and (B) down flow (12 km). C, Plot showing volume percent of crystals and vesicles with distance down flow. All samples from the vent area (distance of 0 km) are air-fall tephra or spatter samples. Error bars are ± 1 standard error. μm , micrometers.

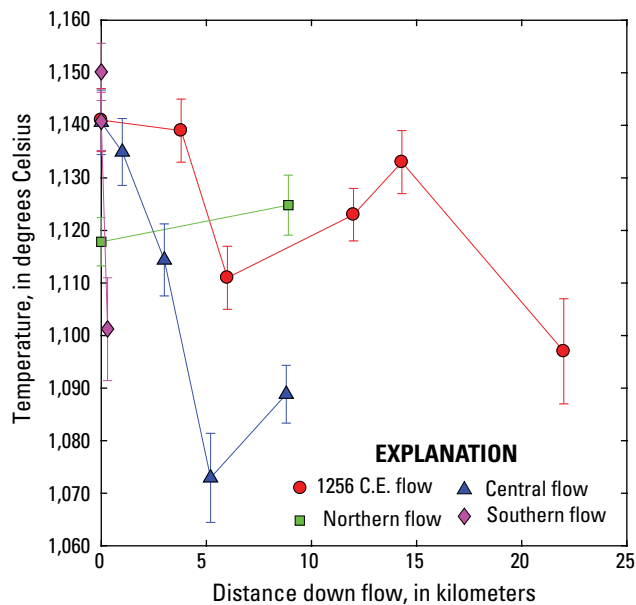


Figure 7. Plot of lava temperatures calculated using liquid, olivine-liquid, and plagioclase-liquid geothermometers versus distance down flow. Values are averages of all temperature calculations (see [appendix 3](#)) and error bars are ± 1 standard error ([table 4](#)).

Table 3. Microprobe analyses of glass, plagioclase, and olivine compositions from northern Harrat Rahat lava flows.

[Values are sample averages. Major-oxide concentrations in weight percent. All iron content reported as FeO (FeO*). See [appendix 1](#) for sample details and [appendices 3–5](#) for all measurements. Mineral end-member compositions are calculated to 100 mole percent (mol. %). An, Ab, and Or are the anorthite, albite, and orthoclase proportions in plagioclase. Fo, Fa, and Tp are the forsterite, fayalite, and tephroite proportions in olivine. km, kilometer; *N*, number of samples; -, not analyzed]

1256 C.E. flow						
Sample	R14TS95	R15DD150B	R15DD015	R15DD012	R15DD010	R16HD010
Description	Tephra	Lava	Lava	Lava	Lava	Lava
Distance from vent (km)	0	3.8	6.0	12.0	14.3	22.0
Glass						
SiO ₂	47.2	46.4	45.7	45.6	47.2	47.7
TiO ₂	3.13	3.74	4.10	3.94	3.75	4.56
Al ₂ O ₃	16.3	14.8	14.8	14.9	15.9	14.2
FeO*	13.0	13.6	13.7	14.1	14.2	15.2
MnO	0.21	0.28	0.31	0.26	0.28	0.27
MgO	5.30	5.48	3.93	4.46	4.98	3.49
CaO	8.50	9.91	9.00	8.48	8.71	10.27
Na ₂ O	4.32	3.96	4.25	3.90	3.85	4.01
K ₂ O	0.99	0.82	1.77	1.37	1.33	1.72
Cl	-	0.02	0.03	0.03	0.02	0.04
P ₂ O ₅	1.11	0.60	1.70	1.67	1.25	1.12
Total	100.1	99.5	99.3	98.7	101.6	102.6
<i>N</i>	51	11	15	15	15	5
Plagioclase						
SiO ₂	53.1	50.3	53.7	53.4	52.7	51.4
TiO ₂	-	0.17	0.20	0.21	0.17	0.21
Al ₂ O ₃	28.6	30.0	28.1	27.9	29.4	29.9
FeO*	1.14	0.83	0.73	0.81	0.74	0.86
MnO	-	0.05	0.04	0.05	0.07	0.08
MgO	0.26	0.36	0.10	0.15	0.13	0.22
CaO	12.1	14.3	11.6	11.8	12.8	13.8
Na ₂ O	4.67	3.15	4.69	4.56	4.20	3.73
K ₂ O	0.27	0.10	0.26	0.27	0.21	0.17
BaO	-	0.05	0.04	0.03	0.05	0.08
SrO	-	0.07	0.22	0.11	0.17	0.19
Total	100.1	99.3	99.7	99.3	100.6	100.6
An (mol. %)	57.9	71.1	56.9	57.9	62.0	66.4
Ab (mol. %)	40.5	28.3	41.6	40.6	36.8	32.6
Or (mol. %)	1.55	0.59	1.54	1.56	1.18	0.99
<i>N</i>	21	7	15	15	15	14
Olivine						
SiO ₂	37.6	38.9	37.2	37.3	38.0	37.8
FeO*	24.2	15.4	27.2	26.9	24.9	25.2
MnO	0.41	0.26	0.54	0.52	0.46	0.47
MgO	37.0	43.3	34.7	35.0	36.9	37.0
CaO	0.37	0.35	0.35	0.39	0.45	0.44
Cr ₂ O ₃	-	0.03	0.04	0.02	0.01	0.03
NiO	0.08	0.15	0.01	0.01	0.02	0.01
Total	99.6	98.3	100.0	100.1	100.7	100.8

Northern flow		Central flow					Southern flow		
R15DD18	R15DD14	R16HD01	R16HD14	R16HD13	R16HD15	R16HD16	R16HD09	R16HD27	R16HD26
Spatter	Lava	Spatter	Lava	Lava	Lava	Lava	Spatter	Spatter	Lava
0	8.9	0	1.0	3.0	5.2	8.8	0	0	0.3
Glass									
47.6	46.2	46.9	44.7	44.3	52.0	48.9	47.2	46.4	47.3
5.21	5.01	4.40	4.68	4.93	4.58	5.45	3.69	3.72	5.03
14.4	15.4	16.4	12.1	11.9	13.9	12.9	15.5	14.7	12.6
14.9	14.8	13.2	14.5	16.4	10.2	11.9	13.8	13.5	13.6
0.27	0.24	0.19	0.32	0.32	0.26	0.28	0.27	0.29	0.33
4.60	4.75	5.41	5.00	4.71	2.92	3.35	6.01	5.49	3.86
7.75	8.70	8.29	11.11	10.14	7.22	8.40	10.28	9.96	12.32
3.01	3.67	4.15	3.21	3.28	3.89	3.75	3.31	3.99	3.72
1.28	1.07	0.90	1.59	1.71	2.38	2.56	0.69	0.82	1.28
0.02	0.03	0.03	0.02	0.02	0.04	0.04	0.02	0.02	0.02
0.71	0.67	0.56	0.66	0.66	1.11	1.34	0.58	0.60	0.83
99.7	100.7	100.4	97.9	98.4	98.5	98.9	101.3	99.5	100.9
13	9	15	13	11	11	9	15	15	12
Plagioclase									
52.0	52.8	52.4	52.7	50.9	53.2	53.5	51.1	51.7	52.8
0.19	0.22	0.29	0.25	0.17	0.22	0.27	0.16	0.12	0.23
29.7	29.0	29.4	29.2	30.1	29.0	28.5	30.9	29.8	29.4
0.72	0.69	0.77	0.78	0.78	0.95	0.99	0.67	0.70	0.68
0.02	0.05	0.05	0.04	0.03	0.04	0.02	0.05	0.07	0.06
0.13	0.11	0.12	0.10	0.14	0.17	0.15	0.17	0.14	0.24
12.9	13.0	12.8	12.5	13.2	12.3	12.0	14.0	13.5	13.2
4.08	4.24	4.21	4.25	3.74	4.32	4.52	3.55	3.64	3.95
0.20	0.19	0.21	0.20	0.15	0.23	0.26	0.13	0.14	0.17
0.09	0.05	0.07	0.10	0.04	0.10	0.04	0.07	0.10	0.11
0.14	0.19	0.25	0.20	0.16	0.16	0.23	0.13	0.13	0.28
100.2	100.5	100.6	100.3	99.4	100.7	100.5	100.9	100.0	101.1
62.9	62.1	62.0	61.2	65.6	60.3	58.6	68.0	66.7	64.2
36.0	36.8	36.8	37.6	33.5	38.3	39.9	31.3	32.5	34.8
1.17	1.09	1.19	1.19	0.88	1.34	1.53	0.75	0.82	0.98
10	6	10	8	10	5	10	11	7	9
Olivine									
37.6	38.5	38.0	38.7	37.0	38.1	37.4	38.8	38.8	38.5
24.6	23.5	22.6	21.1	29.0	22.5	26.1	19.4	19.8	20.8
0.39	0.39	0.37	0.30	0.61	0.38	0.51	0.28	0.33	0.38
36.4	37.7	38.8	40.2	33.8	39.0	35.5	41.7	40.7	39.8
0.14	0.33	0.32	0.24	0.34	0.31	0.53	0.37	0.32	0.41
0.03	0.06	0.06	0.09	0.06	0.05	0.02	0.08	0.07	0.06
0.08	0.07	0.08	0.10	0.06	0.08	0.10	0.14	0.11	0.11
99.2	100.6	100.3	100.7	100.8	100.3	100.1	100.8	100.2	100.1

Table 3.—Continued

1256 C.E. flow						
Olivine—Continued						
Fo (mol. %)	72.8	83.1	69.0	69.5	72.2	72.0
Fa (mol. %)	26.7	16.6	30.3	29.9	27.3	27.5
Tp (mol. %)	0.46	0.28	0.62	0.58	0.51	0.52
N	8	8	25	23	30	19

Table 4. Textural analysis, thermometry, and viscosity results.

[See [appendix 6](#) for results from individual geothermometers. Viscosity errors are calculated on a log scale and shown as error bars in [fig. 8](#). km, kilometer; s⁻¹, per second; -, not applicable]

1256 C.E. flow						
Sample	R14TS95	R15DD150B	R15DD015	R15DD012	R15DD010	R16HD010
Description	Tephra	Lava	Lava	Lava	Lava	Lava
Distance from vent (km)	0	3.8	6.0	12.0	14.3	22.0
Volume proportions from textural analysis, in percent						
Melt	45.3	68.5	67.5	67.5	65.1	43.2
Vesicles	54.1	10.7	0.3	5.6	8.9	2.4
Crystals	0.5	20.8	32.2	26.9	26.0	54.4
Plagioclase	0.2	13.3	24.3	24.0	22.6	48.0
Olivine	0.3	7.5	7.4	2.6	3.3	6.2
Oxides	0.0	0.0	0.4	0.3	0.1	0.3
Thermometry, in degrees Celsius						
Average	1,141	1,139	1,111	1,123	1,133	1,097
Standard error	6	6	6	5	6	10
Viscosity, in pascal seconds						
Liquid viscosity (Giordano and others, 2008)	1.4×10 ²	1.4×10 ²	4.2×10 ²	2.7×10 ²	1.9×10 ²	7.0×10 ²
Apparent viscosity (Mueller and others, 2010)	1.5×10 ²	4.8×10 ²	3.2×10 ³	1.4×10 ³	1.0×10 ³	-
Apparent viscosity (Costa and others, 2009, strain rate of 10 ⁻⁴ s ⁻¹)	1.5×10 ²	4.5×10 ²	3.4×10 ³	1.4×10 ³	1.0×10 ³	3.4×10 ⁶
Apparent viscosity (Costa and others, 2009, strain rate of 1 s ⁻¹)	1.5×10 ²	3.8×10 ²	2.6×10 ³	1.1×10 ³	8.2×10 ²	1.0×10 ⁶

Northern flow			Central flow				Southern flow		
Olivine—Continued									
72.2	73.7	75.0	77.0	67.1	75.3	70.4	79.0	78.3	77.0
27.4	25.8	24.5	22.7	32.3	24.3	29.0	20.7	21.3	22.6
0.44	0.43	0.41	0.32	0.69	0.41	0.57	0.30	0.36	0.42
4	10	13	6	12	12	12	15	5	3

Northern flow		Central flow					Southern flow		
R15DD18	R15DD14	R16HD01	R16HD14	R16HD13	R16HD15	R16HD16	R16HD09	R16HD27	R16HD26
Spatter	Lava	Spatter	Lava	Lava	Lava	Lava	Spatter	Spatter	Lava
0	8.9	0	1.0	3.0	5.2	8.8	0	0	0.3

Volume proportions from textural analysis, in percent

48.5	66.4	54.9	65.9	45.4	38.5	31.8	56.0	44.9	42.5
28.1	5.4	22.6	4.4	7.3	2.3	8.3	24.0	31.9	8.2
23.4	28.2	22.4	29.7	47.3	59.2	59.9	20.0	23.2	49.3
18.9	19.9	16.4	22.1	36.2	46.4	46.7	13.9	15.7	43.9
3.1	8.0	5.5	6.6	10.1	10.7	8.1	5.9	6.5	3.1
1.4	0.4	0.5	1.0	1.0	2.2	5.1	0.2	1.0	2.3

Thermometry, in degrees Celsius

1,118	1,125	1,141	1,135	1,114	1,073	1,089	1,150	1,141	1,101
5	6	6	6	7	9	6	5	6	10

Viscosity, in pascal seconds

6.7×10^2	3.1×10^2	1.9×10^2	2.0×10^2	5.7×10^2	1.1×10^4	3.8×10^3	9.8×10^1	1.3×10^2	8.0×10^2
5.3×10^3	1.9×10^3	1.1×10^3	1.4×10^3	-	-	-	4.3×10^2	1.3×10^3	-
5.6×10^3	1.9×10^3	1.1×10^3	1.4×10^3	3.9×10^5	5.2×10^8	1.6×10^9	4.2×10^2	1.4×10^3	1.6×10^6
4.3×10^3	1.5×10^3	8.4×10^2	1.1×10^3	1.5×10^5	1.5×10^8	4.1×10^8	3.4×10^2	1.0×10^3	5.2×10^5

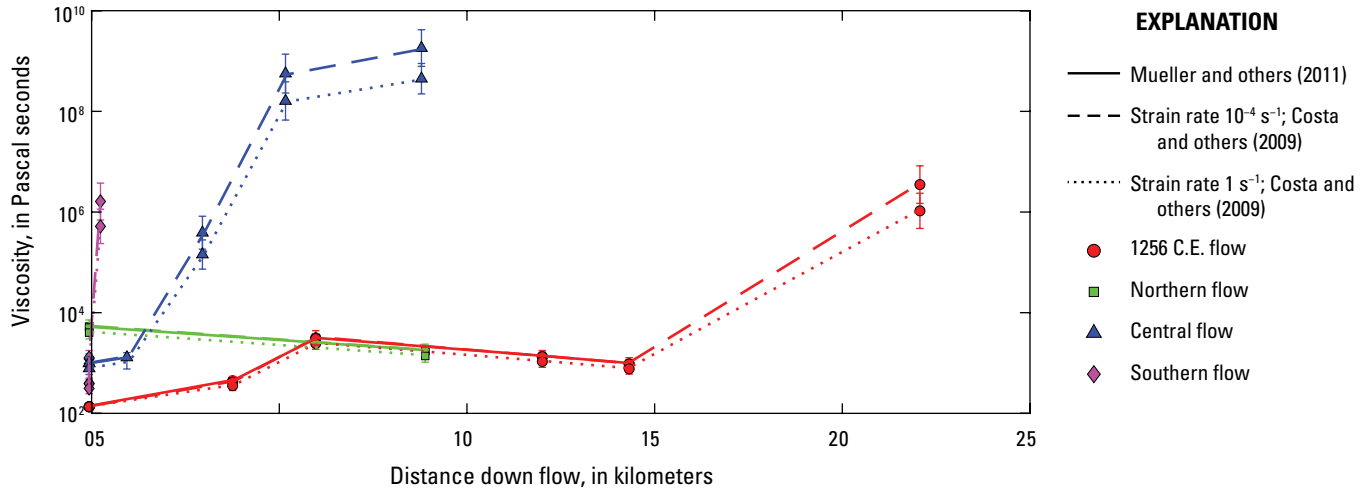


Figure 8. Plot of apparent viscosities with distance down flow. Viscosities are calculated from [equation 1](#) with liquid viscosity (η_{liq}) from Giordano and others (2008) and relative viscosity (η_r) from either Mueller and others (2011; eqs. 2–3; solid line) or Costa and others (2009) with parameters from Cimarelli and others (2011) at low (dashed line) and high (dotted line) strain rates (eqs. 4–5). Error bars are ± 1 standard error.

Since these flows generally have low vesicularity away from their vents (the average vesicularity for all lava samples is 5.8 volume percent, with a standard deviation of 3.2 percent and range of 0.3–10.7 percent; [fig. 6](#)), the influence of vesicles on rheology would have been relatively small (Lewellin and Manga, 2005; Mader and others, 2013; Truby and others, 2015). The effect of the vesicle fraction varies with strain rate, such that relative viscosities for our lavas ranged from 0.9 to 1.1 for η_{app} of 2,000 Pa·s and an average bubble radius of 0.01 mm following Llewellyn and Manga (2005) and Mader and others (2013). Vesicles in these lavas therefore have decreased or increased the apparent viscosity during flow and thus increase uncertainty in the calculated properties. For the air-fall tephra and spatter samples, the higher vesicularity results in greater uncertainty, but a full vesicle size distribution and independent strain rate analysis is needed to determine the rheology effect more precisely (Mader and others, 2013). However, model results and their errors from both textural and petrologic analyses are representative of the magnitudes and trends in the viscosity results (Riker and others, 2009; Chevrel and others, 2013; Mader and others, 2013) and also highlight uncertainties ([fig. 8](#)).

Effusion Rates

Effusion rate calculations integrate rheology and morphology observations using methods from Kerr and others (2006) and Deardorff and Cashman (2012). As predicted by [equation 6](#), channel width varies inversely with slope ([fig. 9A](#)). However, this relation does not hold for flow segments where lateral spreading of the flow was limited, such as where the

Central and Southern flows wound through hilly topography ([figs. 2C and 5](#)). We therefore exclude these regions from our analysis. Local effusion rates through each channel are calculated by fitting [equation 6](#) to the remaining morphologic data with rheological parameters derived from our petrologic analysis and solving for the best-fit flux term (Q in [eq. 6](#)).

The rheological parameters that must be determined for application of this crust-dominated flow model are the strength of the crust and the core viscosity. We estimate the crustal yield strength from the 1256 C.E. rheological parameters and the observed total mean output rate (solid line in [fig. 9A](#)). Fitting [equation 6](#) to the 1256 C.E. total mean output rate, core viscosity, slope, and channel width returns a crustal yield strength of $2.5 \pm 0.5 \times 10^6$ Pa, which falls within the range observed for lavas in other studies (Blake and Bruno, 2000; Kerr and others, 2006; Kerr and Lyman, 2007; Deardorff and Cashman, 2012; Castruccio and others, 2013). The core viscosities derived from the apparent viscosity measurements for each flow are given in [table 5](#). Although our Harrat Rahat measurements generally capture solidification down flow with lower temperatures and increasing crystal content, the bulk rheology of the 1256 C.E. flow, as well as the limited Northern flow results, changed little with distance ([figs. 6–8](#)).

Results for each flow and flow branch show a range of best-fit lava channel fluxes (local effusion rates) from 15 ± 2 to 68 ± 11 cubic meters per second (m^3/s) based on channel width, rheology, and slope ([table 5](#)). With significant scatter in the data, we include the 95-percent confidence interval error for fitted flux values in [table 5](#). Following Deardorff and Cashman (2012), we also further account for this scatter by finding flux values that bracket the entire dataset, including

flow width, to explore the full range of potential values (fig. 9B). Instantaneous effusion rate typically peaks near the start of eruptions (Wadge, 1981; Harris and others, 2011; Bonny and Wright, 2017), and flow width may capture this with best-fit fluxes on the order of 100 m³/s (table 5). Flow

width also grows by overflows (Walker, 1971; Lipman and Banks, 1987; Tarquini and de' Michieli Vitturi, 2014), so these values represent maxima. Although our results have significant uncertainty, the magnitudes and relative lava fluxes through these channels provide information on eruption dynamics.

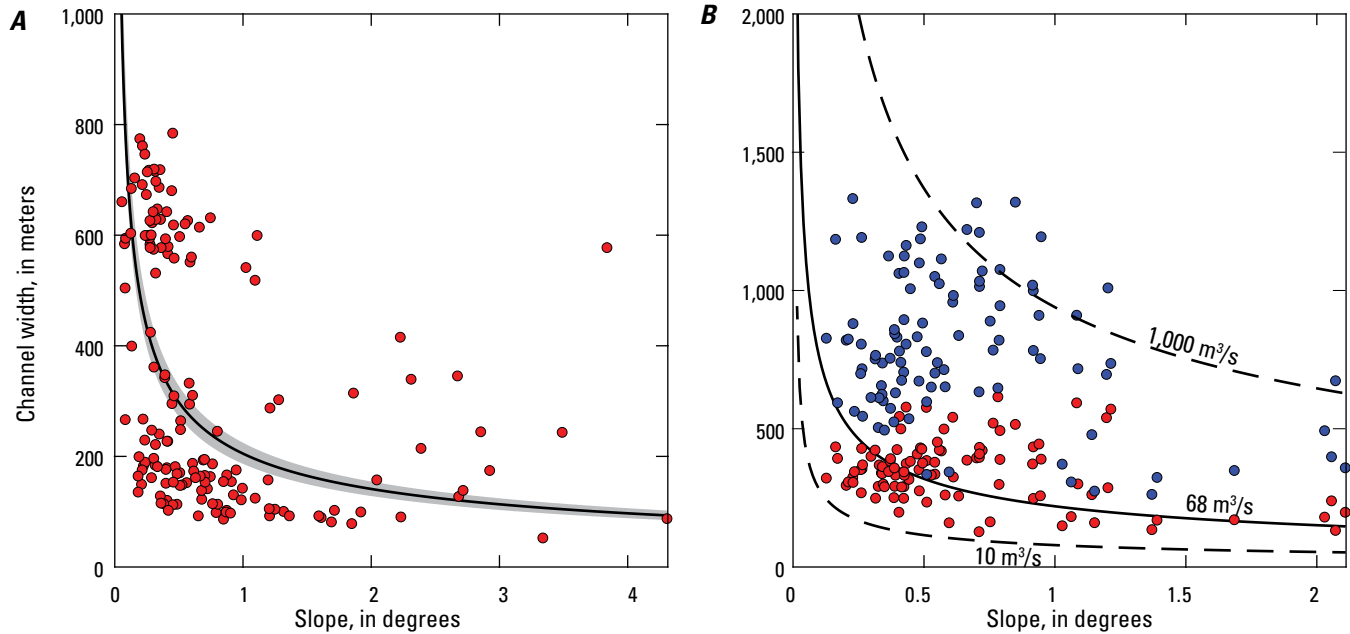


Figure 9. Plots of flow and channel width versus slope. *A*, The 1256 C.E. flow channel width measurements compared to slope. The black line shows the equation 6 curve fit and the gray area shows the 95-percent confidence interval (best-fit crustal yield strength [σ_c] is $2.5 \pm 0.5 \times 10^6$ pascals and observed average flux [Q] is 98 cubic meters per second [m³/s]). *B*, Flow (blue dots) and channel (red dots) widths compared to slope for the south branch of the Southern flow. The best-fit flux is shown by the solid line (68 m³/s), accompanied by dashed curves showing 10 and 1,000 m³/s fluxes that bracket the dataset.

Table 5. Harrat Rahat lava effusion rate, duration, and advance rate estimates.

[Pa·s, pascal second; m³/s, cubic meter per second; m/h, meter per hour]

Flow	Core viscosity (Pa·s)	Best-fit flux (m ³ /s)	Maximum flux from flow width (m ³ /s)	Duration (days)	Average advance rate (m/h)	Channel advance rate (m/h)
1256 C.E. flow						
1256 C.E. flow	$7.6 \pm 2.0 \times 10^2$	98 (fit)	$7.0 \pm 0.9 \times 10^2$	52 (observed)	17	$8.4 \pm 0.6 \times 10^2$
Northern flow						
West branch	$2.9 \pm 0.9 \times 10^3$	15 ± 2	$4.0 \pm 1.0 \times 10^2$	108 ± 15	6 ± 1	$2.3 \pm 0.3 \times 10^2$
East branch	$2.9 \pm 0.9 \times 10^3$	21 ± 5	$1.7 \pm 0.4 \times 10^2$	24 ± 6	23 ± 6	$2.7 \pm 0.6 \times 10^2$
Whole flow		36 ± 5	$5.7 \pm 1.0 \times 10^2$			
Central flow						
Central flow	$4.3 \pm 1.8 \times 10^3$	51 ± 13	$1.8 \pm 0.3 \times 10^2$	15 ± 4	44 ± 11	$2.4 \pm 0.5 \times 10^2$
Southern flow						
North branch	$1.8 \pm 0.8 \times 10^3$	40 ± 5	$3.2 \pm 0.7 \times 10^2$	26 ± 3	32 ± 4	$3.4 \pm 0.5 \times 10^2$
South branch	$1.8 \pm 0.8 \times 10^3$	68 ± 11	$3.2 \pm 0.5 \times 10^2$	8 ± 1	85 ± 13	$4.4 \pm 0.7 \times 10^2$
Whole flow		$1.1 \pm 0.1 \times 10^2$	$6.4 \pm 0.8 \times 10^2$			

For flows with simple channel geometries (in other words, the cases of the 1256 C.E. second pulse and the Central flow), the lava flux through a single channel represents an estimate of the total average effusion rate at the vent during channel formation. For branched flow fields (Northern and Southern flow fields), the volumetric lava fluxes of each branch capture the local average effusion rates and should sum to the total average effusion rate at the vent (36 ± 5 and 108 ± 12 m³/s, respectively). For the Northern flow, our results show similar local effusion rates through the west and east channels (table 5). Within the Southern flow, the estimated effusion rate through the south channel is more than 1.5 times higher than in the north channel. Morphologically, our mapping shows that only the northmost section of the eruptive fissure lies directly upslope of the north channel (figs. 1B and 5), so this difference could reflect that the north branch was fed by a smaller proportion of the fissure than the south branch.

Eruption Durations

We can also use the effusion rate estimates to calculate the potential range of eruption durations for the Five Fingers. Assuming the lava flux estimates through the channels are best estimates for the local average effusion rates, and combining them with the corresponding volumes of each branch in table 5, we calculate the time required to emplace the individual flow branches. These emplacement times offer estimates of eruption durations with values on the order of weeks, similar to the 52-day duration of the eruption observed for the entire 1256 C.E. eruption (Al-Samhūdī, 1488). Different durations estimated for the different branches of the Northern and Southern flows suggest that not all branches were active for the entire eruption. For example, the estimated local average effusion rate through the north channel of the Southern flow is lower than for south channel, but the volume of the north branch is larger (table 5). This may reflect that although the north branch was fed at a lower lava supply rate, it was fed for a longer duration than the south branch.

Discussion

By integrating morphologic and textural observations with analytical models of rheology and flow propagation, we can reconstruct the emplacement conditions and behaviors of the Harrat Rahat lavas. Results encompass eruption temperatures, viscosities, effusion rates, down-flow cooling and crystallization, as well as eruption duration. All of these inform the dynamics of past Harrat Rahat eruptions and have implications for the emplacement behavior of future lava flows in Harrat Rahat and the magnitudes, rheologies, dynamics, and durations of mafic volcanic field eruptions. We analyze our results in context through comparisons with other volcanic fields, as well as recent, well-observed mafic lava flows from shield and stratovolcanoes around the world (table 6).

Cooling and Crystallization

The rheological evolution of these Harrat Rahat lava flows demonstrates the interplay between cooling, crystallization, and surface morphology in basaltic lavas. Vent temperatures of $\sim 1,140$ °C calculated for Harrat Rahat lavas are subliquidus, as shown by the initial crystallinity at the vent, which is in agreement with liquidus temperatures of 1,188 to 1,223 °C estimated by MELTS software at atmospheric pressure (Ghiorso and Sack, 1995). Vent temperatures are similar to eruption temperatures of ‘a‘ā-dominated flows at Mauna Loa and Kīlauea volcanoes in Hawai‘i (table 6; Lipman and Banks, 1987; Wolfe and others, 1987; Cashman and others, 1999; Soule and others, 2004; Robert and others, 2014). The 1256 C.E. flow measurements show an overall cooling rate of 1.6 °C/km, whereas the Central flow cooled much more rapidly at 7.0 °C/km (fig. 7). These rates are consistent with open channel flows, where cooling rates, particularly near the vent, can be greater than 5 °C/km, but cooling along channels further from the vent can be less than 1 °C/km (table 6; Lipman and Banks, 1987; Cashman and others, 1999; Soule and others, 2004; Harris and others, 2007b; Riker and others, 2009; Robert and others, 2014; Kolzenburg and others, 2017; Rhéty and others, 2017). Temperatures at the vent may also have varied during eruption, particularly with variable magma compositions (table 1), but we are unable to assess this with our samples. For the Northern and Southern flows, cooling trends

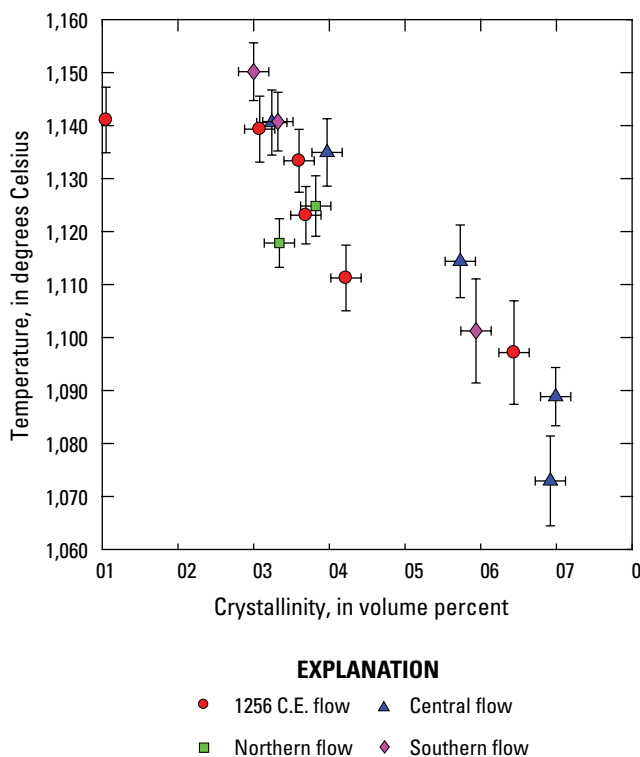


Figure 10. Plot of calculated temperature versus measured crystallinity for all studied flows. Error bars are ± 1 standard error.

Table 6. Global lava effusion rate, duration, and advance rate estimates.

[Values for whole volcanic fields or volcanoes are ranges for lava flows from them. Effusion rates are bulk mean output rates, unless otherwise specified. m³, cubic meter; km, kilometer; °C, degree Celsius; °C/km, degree Celsius per kilometer; m³/s, cubic meter per second; m/h, meter per hour; max. maximum; -, not reported]

Volcano	Bulk volume (×10 ⁶ m ³)	Length (km)	Eruption temperature (°C)	Cooling rate (°C/km)	Effusion rate (m ³ /s)	Duration (days)	Advance rate (m/h)	Reference(s)
Mafic volcanic fields								
Harrat Rahat	70–440	14.3–21.8	1,118–1,150	1.6–7.0	36–106	15–108	6–840	This chapter
Paricutín, 1943–1952	700	1–10	1,070	-	1–4	0.5	1–180	Krauskopf (1948); Fries (1953); Foshag and Gozález (1956)
Auckland	0.02–650	0.8–11	-	-	-	-	-	Kereszturi and others (2013)
Cima	15	2	1,110	0	30	6	14 (average)	Soldati and others (2017)
Sand Mountain	1–190	<8	-	-	-	-	-	Deligne and others (2016)
Other mafic lava flows								
Mauna Loa (historical)	1–383	10–51	-	-	-	1–450	-	Lockwood and Lipman (1987)
Mauna Loa, 1859	270	51	1,194–1,216	0.5–5.6	116–235 (391 at peak)	18–27	267 (average), 3,600 (max.)	Riker and others (2009)
Mauna Loa, 1984	220	27	1,140	0.7	275	21	280 (average), 5,000 (max.)	Lipman and Banks (1987)
Kīlauea, May 1974	4.1–9.7	8.6	1,164	6.7	23–54 (90–420 at peak)	2.1	600 (max.)	Harris and others (2009); Robert and others (2014); Sehlke and others (2014)
Kīlauea, July 1974	3.5	2	1,150	7	150–275	0.2	350–6,000	Soule and others (2004)
Kīlauea, Pu‘u ‘Ō‘ō (‘a‘ā flows)	2–38	2–13	1,135–1,150	4.4–6.8	10–500	0.2–16	50–500	Wolfe and others (1987); Cashman and others (1999); Heliker and Mattox (2003); Kauahikaua and others (2003)
Piton de la Fournaise, April 2007	200–230	3	1,167	6.8–42	84 (200 at peak)	29.6	261	Peltier and others (2009); Rhéty and others (2017)
Piton de la Fournaise, December 2010	350	1.1	1,145	11–27	9.8 (132 at peak)	0.6	73 (average)	Soldati and others (2018)
Tenerife (historical)	0.7–51	2–9	-	-	0.5–15	9 to >98	70–4,000	Solana (2012)
Holuhraun, 2014–2015	1,440	17	1,147–1,200	18.7–24	90 (350 at peak)	182	63	Kolzenburg and others (2017); Pedersen and others (2017)
Etna (since 1980)	0.4–185	0.2–8.8	1,060–1,100	5–180 (max. in 2001)	0.3–183	0.2 to <518	30 (in 2001) to 125 (max. in 1981)	Guest and others (1987); Harris and others (2005, 2007b, 2011); Coltelli and others (2007)

are uncertain because of the lack of glassy samples from along their lengths. Nevertheless, our sampling enables estimates of vent temperature, with a distal sample from the Northern flow that shows a slight increase in temperature (within error) and a near-vent sample from the Southern flow shows cooling, but with a large uncertainty.

Cooling of the Harrat Rahat flows was accompanied by a pronounced increase in crystallinity, with both olivine and plagioclase having crystallized in the groundmass, which is normal during cooling of basaltic lavas (Helz and Thornber, 1987; Crisp and others, 1994; Soule and others, 2004; Riker and others, 2009; Robert and others, 2014; Rhéty and others, 2017; Soldati and others, 2018). All of the flows record a similar relation between temperature and crystallinity (fig. 10). In places, small temperature changes were accompanied by significant crystallization, suggesting degassing-induced crystallization and buffering of flow temperature by latent heat (Lipman and Banks, 1987; Riker and others, 2009). The 1256 C.E. flow shows nearly constant flow temperature and crystallinity over much of its length (figs. 6 and 7), resulting in steady calculated viscosities (fig. 8) and supporting the use of the crust-dominated model for effusion rate estimation.

The rheological evolution of each flow was also accompanied by changes in surface morphology. Mapping of the 1256 C.E. flow by Kereszturi and others (2016) found a transition from pāhoehoe to ‘a’ā at ~2 km down flow (fig. 1B). This transition is strongly controlled by viscosity, and the trends in our data suggest a temperature of ~1,140 °C and a vesicle-free crystallinity of ~12 volume percent, yielding a magma viscosity of ~250 Pa·s, at this distance. These values are consistent with flow properties recorded at the pāhoehoe to ‘a’ā transition in a number of Hawaiian flows (Soule and others, 2004; Robert and others, 2014) and rheology experiments (Sehlke and others, 2014; Kolzenburg and others, 2017). Strain rate also plays a major role in the transition, which is commonly associated with slope increase (MacDonald, 1953; Peterson and Tilling, 1980; Robert and others, 2014). For the 1256 C.E. flow, we see a large increase in slope (as much as 4.3°) at the transition location, accompanied by a decrease in flow thickness and flow width (fig. 5A–B). The change in slope likely resulted in an increased flow velocity, producing a thinner and narrower flow, as well as higher strain rates, that, combined with increased viscosity, formed ‘a’ā. Our measurements of rheological and morphological evolution are also in line with the qualitative progression of flow surface morphologies that Murcia and others (2014) identify in the Five Fingers flows. Further sampling and analysis of the Northern and Southern flows is needed to characterize their rheological evolution more completely.

Flow Volumes

Our calculated volumes are similar to past estimates for the Harrat Rahat flows. Previous bulk volume estimates for the 1256 C.E. flow range from 0.29 to 0.5 km³ (Camp and others, 1987; Murcia and others, 2014; Kereszturi and others,

2016). Our calculation of 0.44 km³ using flow cross sections accounts for more detail than an average thickness and total area approach, and avoids the negative thicknesses within the estimate of 0.4 km³ by Kereszturi and others (2016). The previous interpretation of the Five Fingers flows as made up of the northern “Two Fingers” (Northern flow) and the southern “Three Fingers” (Central and Southern flows), yielded bulk volumes of 0.09 and 0.23 km³, respectively (Murcia and others, 2014). We calculate a much larger bulk volume of 0.18 km³ for the Northern flow, which is consistent with the area and thicknesses reported by Murcia and others (2014), whereas their “Three Fingers” volume is similar to our combined bulk volume of Central and Southern flows of 0.20 km³ (0.22 km³ including vents; table 2). Based on mapping of the entire volcanic field, the extents of these flows are representative of Harrat Rahat basalts (Camp and Roobol, 1989; Downs and others, 2018, 2023; Stelten and others, 2020, 2023).

With dense rock equivalent (DRE) volumes on the order of 10⁻² to 10⁻¹ km³, these Harrat Rahat lavas are small-volume basalts typical of mafic volcanic fields (<1 km³; Valentine and Connor, 2015; table 6). However, the comparison in table 6 shows that they have larger volumes than most recent basaltic lava flows at Kīlauea (Heliker and Mattox, 2003), Piton de la Fournaise (Peltier and others, 2009), Tenerife (Solana, 2012), and Etna (Harris and others, 2011), but are of similar volume to historical eruptions from Mauna Loa (Lockwood and Lipman, 1987) and smaller than the 2014–2015 Holuhraun eruption in Iceland (Pedersen and others, 2017) and the 2018 lower East Rift Zone eruption of Kīlauea (Neal and others, 2019). Among mafic volcanic fields, these young Harrat Rahat lavas are larger than most Auckland volcanic field lavas (Kereszturi and others, 2013), smaller than the total eruption of Parícutín (Fries, 1953), and of similar size to past eruptions in the Sand Mountain and Cima volcanic fields (Deligne and others, 2016; Soldati and others, 2017).

Flow Dynamics

Effusion rate estimates and emplacement durations are of primary importance for understanding and modeling lava flow behavior (Harris and others, 2007a). Our combined rheologic and morphologic analyses reveal local average effusion rates ranged from 36 to 106 m³/s, erupting over 1 to 15 weeks (table 5). These effusion rates are typical for Kīlauea ‘a’ā flows (Heliker and Mattox, 2003; Kauahikaua and others, 2003), consistent with the later phases of the Holuhraun eruption (Pedersen and others, 2017), larger than most Etna eruptions (Harris and others, 2011), but smaller than many Mauna Loa eruptions (Walker, 1973) (table 6). Amongst volcanic fields, a similar effusion rate of 10¹ to 10² m³/s has been estimated from the youngest eruption within the Cima volcanic field using rheology experiments and morphologic analysis (Soldati and others, 2017), whereas typical lava effusion during the Parícutín eruption was observed on the order of 1 m³/s (Krauskopf, 1948). In Harrat Rahat, calculated eruption durations of weeks are in agreement with the 1256 C.E.

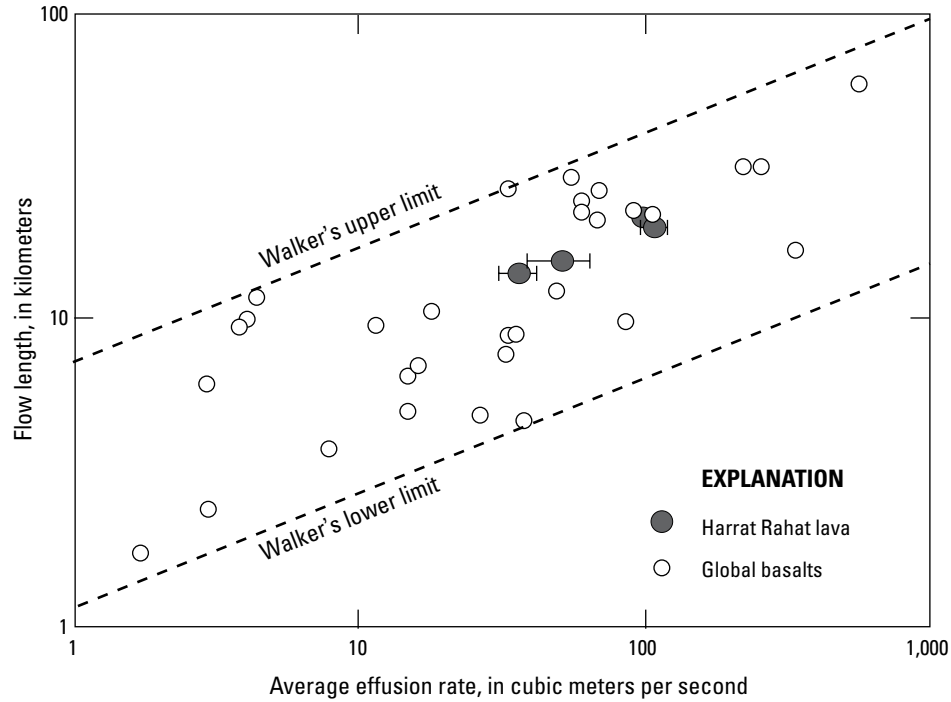


Figure 11. Plot of flow length versus effusion rate for the four studied Harrat Rahat lava flows compared with the global dataset of mean output rates and lengths of basaltic lavas. General trend limits from Walker (1973). Effusion rates are the total mean output rate for the 1256 C.E. flow and the best-fit total average effusion rates from analytical modeling for the Five Fingers flows.

eruption, and similar to observed Mauna Loa, Etna, Tenerife, and Piton de la Fournaise eruptions (table 6; Lockwood and Lipman, 1987; Peltier and others, 2009; Harris and others, 2011; Solana, 2012). Our analysis is constrained by the limited glassy samples available and significant uncertainties, but it provides valuable estimates of effusion rates and emplacement durations of Harrat Rahat eruptions critical for informing the potential hazards and impacts from a future eruption in the region, as well as insights into the magnitudes and timescales of activity at other mafic volcanic fields.

Lava flow length is widely observed to be controlled by effusion rate, and our results support this. We estimate total average effusion rate and flow length independently for each eruption and find a correlation between them (fig. 11). Our results fall within the global distribution of basalt flow lengths and average effusion rates (Walker, 1973). Although lateral confinement can lengthen flows (Dietterich and Cashman, 2014), our results from the Central and Southern flows, which are both confined at their distal ends by interaction with hilly topography (fig. 2C), do not show this effect. The geometry of these hills, though laterally confining, may have also impeded the flow advance, forcing the highly sinuous flow paths apparent in the morphology and reducing the anticipated lengthening effect (fig. 1B).

Flow lengths and estimated eruption durations indicate average advance rates were around 6 to 85 meters per hour

(m/h) with significant uncertainty (table 5). Our measurements can also be used to estimate likely velocities within channels during eruption. Channel geometry, slope, flux, and rheology can be related to channel depth-averaged propagation rate (U_{front}) after Kerr and others (2006)

$$U_{front} = \frac{1}{3} \left[\frac{9g\Delta\rho \sin \theta Q^2}{\eta_{app} w^2} \right]^{\frac{1}{3}}. \quad (7)$$

Applying the core viscosity (η_{app}), calculated flux (Q), and average width (w) and slope (θ), we calculate propagation rates at the flow front were between 230 and 840 m/h for the studied flows (table 5), which are faster than average rates from length and duration. These faster velocities may more accurately represent lava advance rates in the early stages of the eruption and correspond well with advance rates of flows with comparable effusion rates at other mafic volcanic fields and basaltic shields and stratovolcanoes (table 6). Modeling of the 1256 C.E. flow by Kereszturi and others (2016) similarly found maximum modeled time-averaged advance rates of ~200 m/h. Farther from the vent, and later in the eruption, decaying effusion rates and continued cooling and crystallization would have retarded flow advance (Wadge, 1981; Lipman and Banks, 1987; Harris and Rowland, 2001; Bonny and Wright, 2017).

Conclusions

With few observed eruptions in Holocene mafic volcanic fields worldwide, our morphologic and petrologic analyses of lava flow emplacement in Harrat Rahat offer insight into the eruptive conditions and dynamics of these events. We focus on four of the youngest flows in Harrat Rahat and use new whole-rock geochemistry and field observations to separate the previously described Five Fingers flows into three separate eruptive units, with the Northern and Southern flows made up of multiple flow branches. Morphologic analysis yields volume estimates typical of mafic volcanic fields ranging from 0.07 to 0.42 km³ DRE. With petrologic analysis, we find that these flows erupted at subliquidus temperatures of ~1,140 °C. For the well-sampled 1256 C.E. and Central flows, we observed evidence of flow cooling and crystallization with distance down flow producing apparent viscosities that increased from 10² to 10⁹ Pa·s. Combining rheology estimates with morphologic analysis of channel width and slope, we use analytical theory to reconstruct effusion rates that ranged from approximately 40 to 110 m³/s, and estimate eruption durations of 1 to 15 weeks. Our results support previous assessments of the intrinsic and extrinsic controls on lava flow emplacement, tracking the temperature and crystallinity down flow, quantitatively describing the transition from pāhoehoe to ‘a’ā, and documenting the effects of effusion rate and underlying topography on flow morphology and length (Walker, 1973; Cashman and others, 1999; Soule and others, 2004; Riker and others, 2009; Robert and others, 2014; Soldati and others, 2018).

A comparative analysis of these results demonstrates that the mafic volcanic field eruptions in Harrat Rahat have similar emplacement conditions to basaltic eruptions observed around the world (fig. 11; table 6). We find flow volumes and lengths consistent with other mapped mafic volcanic fields, and additionally contribute estimates of effusion rates and durations that offer quantitative insights into the magnitudes and variability of these crucial eruption parameters in these settings. Our petrology and rheology results record similar behavior to well-studied, open-channel flows and contribute measurements, trends, and interdependencies of the physical properties of flows in mafic volcanic fields. Critically, we also show that the Harrat Rahat lavas have comparable properties and dynamics to recent eruptions at basaltic shield and stratovolcanoes. Thus, the frequent mafic effusive eruptions in these settings can inform the properties and dynamics of the less frequent, but widespread, mafic volcanic field eruptions for a greater understanding of their eruptive history and potential future behavior and hazards.

Acknowledgments

This research was funded by the Saudi Geological Survey through a Technical Cooperative Agreement between the Saudi Geological Survey and U.S. Geological Survey. We

thank Tom Sisson, Dave Sherrod, and the Saudi Geological Survey staff for help with field sampling and Leslie O’Brien and Dawnika Blatter for analytical assistance. Reviews of this manuscript by Elise Rumpf and Tim Orr, as well those of a previous version by Carmen Solana, Oryaëlle Chevrel, Mike James, and Andy Harris, greatly improved this chapter.

References Cited

- Al-Samhūdī, A.B.A.A., 1488 [edited and reprinted in 2001], *Wafā‘ al-Wafā‘ bi Akhbār Dār al-Muṣṭafā*: London, Al-Furqān Islamic Heritage Foundation, 2,615 p.
- Armstrong, J.T., 1995, CITZAF—A package of correction programs for quantitative electron microbeam X-ray analysis of thick polished materials, thin films, and particles: *Microbeam Analysis*, v. 4, p. 177–200.
- Beattie, P., 1993, Olivine-melt and orthopyroxene-melt equilibria: *Contributions to Mineralogy and Petrology*, v. 115, p. 103–111, <https://doi.org/10.1007/BF00712982>.
- Bergantz, G.W., Schleicher, J.M., and Burgisser A., 2017, On the kinematics and dynamics of crystal-rich systems: *Journal of Geophysical Research*, v. 122, p. 6131–6159, <https://doi.org/10.1002/2017JB014218>.
- Blake, S., and Bruno, B.C., 2000, Modelling the emplacement of compound lava flows: *Earth and Planetary Science Letters*, v. 184, p. 181–197, [https://doi.org/10.1016/S0012-821X\(00\)00278-8](https://doi.org/10.1016/S0012-821X(00)00278-8).
- Bonny, E., and Wright, R., 2017, Predicting the end of lava flow-forming eruptions from space: *Bulletin of Volcanology*, v. 79, no. 52, 13 p., <https://doi.org/10.1007/s00445-017-1134-8>.
- Camp, V.E., Hooper, P.R., Roobol, M.J., and White, D.L., 1987, The Madinah eruption, Saudi Arabia—Magma mixing and simultaneous extrusion of three basaltic chemical types: *Bulletin of Volcanology*, v. 49, p. 498–508, <https://doi.org/10.1007/BF01245475>.
- Camp, V.E., and Roobol, M.J., 1989, The Arabian continental alkali basalt province—Part I, Evolution of Harrat Rahat, Kingdom of Saudi Arabia: *Geological Society of America Bulletin*, v. 101, p. 71–95, [https://doi.org/10.1130/0016-7606\(1989\)101<0071:TACABP>2.3.CO;2](https://doi.org/10.1130/0016-7606(1989)101<0071:TACABP>2.3.CO;2).
- Camp, V.E., and Roobol, M.J., 1991, Geologic map of the Cenozoic lava field of Harrat Rahat, Kingdom of Saudi Arabia: Ministry of Petroleum and Mineral Resources Geoscience Map GM-123, 1:250,000 scale, 37 p.
- Cashman, K.V., Soule, S.A., Mackey, B.H., Deligne, N.I., Deardorff, N.D., and Dietterich, H.R., 2013, How lava flows—New insights from applications of lidar technologies to lava flow studies: *Geosphere*, v. 9, p. 1664–1680, <https://doi.org/10.1130/GES00706.1>.

- Cashman, K.V., Thornber, C., and Kauahikaua, J.P., 1999, Cooling and crystallization of lava in open channels, and the transition of pāhoehoe lav4p 3428 [also released as Saudi Geological Survey Special Report SGS-SP-2019-2], 65 p., 4 sheets, scales 1:75,000, 1:25,000, <https://doi.org/10.3133/sim3428>.
- Champion, D.E., Downs, D.T., Stelten, M.E., Robinson, J.E., Sisson, T.W., Shawali, J., Hassan, K., and Zahran, H.M., 2023, Paleomagnetism of the Harrat Rahat volcanic field, Kingdom of Saudi Arabia—Geologic unit correlations and geomagnetic cryptochron identifications, chap. H of Sisson, T.W., Calvert, A.T., and Mooney, W.D., eds., Active volcanism on the Arabian Shield—Geology, volcanology, and geophysics of northern Harrat Rahat and vicinity, Kingdom of Saudi Arabia: U.S. Geological Survey Professional Paper 1862 [also released as Saudi Geological Survey Special Report SGS-SP-2021-1], 31 p., <https://doi.org/10.3133/pp1862H>.
- Downs, D.T., 2019, Major and trace-element chemical analyses of rocks from the northern Harrat Rahat volcanic field and surrounding area, Kingdom of Saudi Arabia: U.S. Geological Survey data release, <https://doi.org/10.5066/P91HL91C>.
- Downs, D.T., Stelten, M.E., Champion, D.E., Dietterich, H.R., Hassan, K., and Shawali, J., 2023, Eruptive history within the vicinity of Al Madīnah in northern Harrat Rahat, Kingdom of Saudi Arabia, chap. C of Sisson, T.W., Calvert, A.T., and Mooney, W.D., eds., Active volcanism on the Arabian Shield—Geology, volcanology, and geophysics of northern Harrat Rahat and vicinity, Kingdom of Saudi Arabia: U.S. Geological Survey Professional Paper 1862 [also released as Saudi Geological Survey Special Report SGS-SP-2021-1], 41 p., <https://doi.org/10.3133/pp1862C>.
- Downs, D.T., Stelten, M.E., Champion, D.E., Dietterich, H.R., Nawab, Z., Zahran, H., Hassan, K., and Shawali, J., 2018, Volcanic history of the northernmost part of the Harrat Rahat volcanic field, Saudi Arabia: *Geosphere*, v. 14, p. 1253–1282, <https://doi.org/10.1130/GES01625.1>.
- Foshag, W.F., and González, J., 1956, Birth and development of Parícutin Volcano Mexico: U.S. Geological Survey Bulletin 956-D, p. 335–489, <https://doi.org/10.3133/b965D>.
- Fries, C., 1953, Volumes and weights of pyroclastic material, lava, and water erupted by Parícutin volcano, Michoacan, Mexico: *Eos, Transactions American Geophysical Union*, v. 34, p. 603–616, <https://doi.org/10.1029/TR034i004p00603>.
- Ghiorso, M.S., and Sack, R.O., 1995, Chemical mass transfer in magmatic processes IV. A revised and internally consistent thermodynamic model for the interpolation and extrapolation of liquid-solid equilibria in magmatic systems at elevated temperatures and pressures: *Contributions to Mineralogy and Petrology*, v. 119, p. 197–212, <https://doi.org/10.1007/BF00307281>.
- Giordano, D., Russell, J.K., and Dingwell, D.B., 2008, Viscosity of magmatic liquids—A model: *Earth and Planetary Science Letters*, v. 271, p. 123–134, <https://doi.org/10.1016/j.epsl.2008.03.038>.
- Griffiths, R.W., 2000, The dynamics of lava flows: *Annual Review of Fluid Mechanics*, v. 32, p. 477–518, <https://doi.org/10.1146/annurev.fluid.32.1.477>.
- Guest, J.E., Kilburn, C.R.J., Pinkerton, H., and Duncan, A.M., 1987, The evolution of lava flow-fields—Observations of the 1981 and 1983 eruptions of Mount Etna, Sicily: *Bulletin of Volcanology*, v. 49, p. 527–540, <https://doi.org/10.1007/BF01080447>.
- Harris, A.J.L., 2015, Chapter 2. Basaltic Lava Flow Hazard, in Shroder, J.F., and Papale, P., eds., *Volcanic Hazards, Risks and Disasters*: Elsevier, Boston, p. 17–46.
- Harris, A., Bailey, J., Calvari, S., and Dehn, J., 2005, Heat loss measured at a lava channel and its implications for down-channel cooling and rheology, in Manga, M., and Ventura, G., eds., *Kinematics and dynamics of lava flows*: Geological Society of America Special Paper 396, p. 125–146.
- Harris, A.J.L., Dehn, J., and Calvari, S., 2007a, Lava effusion rate definition and measurement—A review: *Bulletin of Volcanology*, v. 70, no. 1, 22 p.
- Harris, A.J.L., Favalli, M., Mazzarini, F., and Hamilton, C.W., 2009, Construction dynamics of a lava channel: *Bulletin of Volcanology*, v. 71, no. 4, p. 459–474.
- Harris, A., Favalli, M., Mazzarini, F., and Pareschi, M.T., 2007b, Best-fit results from application of a thermo-rheological model for channelized lava flow to high spatial resolution morphological data: *Geophysical Research Letters*, v. 34, no. 1, 5 p.
- Harris, A.J., and Rowland, S., 2001, FLOWGO—A kinematic thermo-rheological model for lava flowing in a channel: *Bulletin of Volcanology*, v. 63, no. 1, p. 20–44.
- Harris, A., Steffke, A., Calvari, S., and Spampinato, L., 2011, Thirty years of satellite-derived lava discharge rates at Etna—Implications for steady volumetric output: *Journal of Geophysical Research*, v. 116, no. B08204, 15 p., <https://doi.org/10.1029/2011JB008237>.
- Heliker C., and Mattox, T.N., 2003, The First Two Decades of the Pu‘u ‘Ō‘ō-Kupaianaha Eruption—Chronology and Selected Bibliography, in Heliker, C., Swanson, D.A., and Takahashi, T.J., eds., *The Pu‘u ‘Ō‘ō-Kupaianaha Eruption of Kīlauea Volcano, Hawai‘i—The First 20 Years*: U.S. Geological Survey Professional Paper 1676, p. 1–28.
- Helz, R.T., and Thornber, C.R., 1987, Geothermometry of Kīlauea Iki lava lake, Hawaii: *Bulletin of Volcanology*, v. 49, no. 5, p. 651–668, <https://doi.org/10.1007/BF01080357>.
- Higgins, M.D., 2000, Measurement of crystal size distributions: *American Mineralogist*, v. 85, no. 9, p. 1105–1116, <https://doi.org/10.2138/am-2000-8-901>.

- Hulme, G., 1974, The interpretation of lava flow morphology: *Geophysical Journal International*, v. 39, no. 2, p. 361–383.
- Kauahikaua, J., Sherrod, D.R., Cashman, K.V., Heliker, C., Hon, K., Mattox, T.N., and Johnson, J.A., 2003, Hawaiian lava-flow dynamics during the Pu‘u ‘Ō‘ō-Kupaianaha eruption—A tale of two decades, *in* Heliker, C., Swanson, D.A., Takahashi, T.J., eds., *The Pu‘u ‘Ō‘ō-Kupaianaha Eruption of Kīlauea Volcano, Hawai‘i—The First 20 Years*: U.S. Geological Survey Professional Paper 1676, p. 63–87.
- Kawabata, E., Cronin, S.J., Bebbington, M.S., Moufti, M.R.H., El-Masry, N., and Wang, T., 2015, Identifying multiple eruption phases from a compound tephra blanket—An example of the AD1256 Al-Madinah eruption, Saudi Arabia: *Bulletin of Volcanology*, v. 77, no. 1, p. 6, <https://doi.org/10.1007/s00445-014-0890-y>.
- Kereszturi, G., Németh, K., Cronin, S.J., Agustín-Flores, J., Smith, I.E.M., and Lindsay, J., 2013, A model for calculating eruptive volumes for monogenetic volcanoes—Implication for the Quaternary Auckland Volcanic Field, New Zealand: *Journal of Volcanology and Geothermal Research*, v. 266, p. 16–33, <https://doi.org/10.1016/j.jvolgeores.2013.09.003>.
- Kereszturi, G., Németh, K., Moufti, M.R., Cappello, A., Murcia, H., Ganci, G., Del Negro, C., Procter, J., and Zahran, H.M.A., 2016, Emplacement conditions of the 1256 AD Al-Madinah lava flow field in Harrat Rahat, Kingdom of Saudi Arabia—Insights from surface morphology and lava flow simulations: *Journal of Volcanology and Geothermal Research*, v. 309, p. 14–30, <https://doi.org/10.1016/j.jvolgeores.2015.11.002>.
- Kerr, R.C., Griffiths, R.W., and Cashman, K.V., 2006, Formation of channelized lava flows on an unconfined slope: *Journal of Geophysical Research*, v. 111, no. B10206, 13 p., <https://doi.org/10.1029/2005JB004225>.
- Kerr, R.C., and Lyman, A.W., 2007, Importance of surface crust strength during the flow of the 1988–1990 andesite lava of Lonquimay Volcano, Chile: *Journal of Geophysical Research*, v. 112, no. B03209, 8 p., <https://doi.org/10.1029/2006JB004522>.
- Kilburn, C.R.J., and Lopes, R.M.C., 1991, General patterns of flow field growth—Aa and blocky lavas: *Journal of Geophysical Research*, v. 96, p. 19721–19732, <https://doi.org/10.1029/91JB01924>.
- Kolzenburg, S., Giordano, D., Thordarson, T., Höskuldsson, A., and Dingwell, D.B., 2017, The rheological evolution of the 2014/2015 eruption at Holuhraun, central Iceland: *Bulletin of Volcanology*, v. 79, no. 45, <https://doi.org/10.1007/s00445-017-1128-6>.
- Kolzenburg, S., Jaenicke, J., Münzer, U., and Dingwell, D.B., 2018, The effect of inflation on the morphology-derived rheological parameters of lava flows and its implications for interpreting remote sensing data—A case study on the 2014/2015 eruption at Holuhraun, Iceland: *Journal of Volcanology and Geothermal Research*, v. 357, p. 200–212, <https://doi.org/10.1016/j.jvolgeores.2018.04.024>.
- Krauskopf, K.B., 1948, Lava movement at Parícutin Volcano, Mexico: *Geological Society of America Bulletin*, v. 59, p. 1267–1284, [https://doi.org/10.1130/0016-7606\(1948\)59\[1267:LMAVPM\]2.0.CO;2](https://doi.org/10.1130/0016-7606(1948)59[1267:LMAVPM]2.0.CO;2).
- Lipman, P., and Banks, N., 1987, A‘a flow dynamics, Mauna Loa 1984, *in* Decker, R.W., Wright, T.L., Stauffer, P.H., eds., *Volcanism in Hawaii*: U.S. Geological Survey Professional Paper 1350, p. 1527–1567.
- Llewellyn, E.W., and Manga, M., 2005, Bubble suspension rheology and implications for conduit flow: *Journal of Volcanology and Geothermal Research*, v. 143, p. 205–217, <https://doi.org/10.1016/j.jvolgeores.2004.09.018>.
- Lockwood, J.P., and Lipman, P.W., 1987, Holocene eruptive history of Mauna Loa Volcano, *in* Decker, R.W., Wright, T.L., Stauffer, P.H., eds., *Volcanism in Hawaii*: U.S. Geological Survey Professional Paper 1350, p. 509–535.
- Loock, S., van Wyk de Vries, B., and Hénot, J.-M., 2010, Clinker formation in basaltic and trachybasaltic lava flows: *Bulletin of Volcanology*, v. 72, no. 7, p. 859–870, <https://doi.org/10.1007/s00445-010-0362-y>.
- Lyman, A.W., and Kerr, R.C., 2006, Effect of surface solidification on the emplacement of lava flows on a slope: *Journal of Geophysical Research*, v. 111, no. B05206, 14 p., <https://doi.org/10.1029/2005JB004133>.
- Macdonald, G.A., 1953, Pahoehe, aa, and block lava: *American Journal of Science*, v. 251, p. 169–191, <https://doi.org/10.2475/ajs.251.3.169>.
- Mader, H.M., Llewellyn, E.W., and Mueller, S.P., 2013, The rheology of two-phase magmas—A review and analysis: *Journal of Volcanology and Geothermal Research*, v. 257, p. 135–158, <https://doi.org/10.1016/j.jvolgeores.2013.02.014>.
- Maron, S.H., and Pierce, P.E., 1956, Application of Ree-Eyring generalized flow theory to suspensions of spherical particles: *Journal of Colloid Science*, v. 11, no. 1, p. 80–95, [https://doi.org/10.1016/0095-8522\(56\)90023-X](https://doi.org/10.1016/0095-8522(56)90023-X).
- Mazzarini, F., 2005, Morphology of basaltic lava channels during the Mt. Etna September 2004 eruption from airborne laser altimeter data: *Geophysical Research Letters*, v. 32, no. 4, <https://doi.org/10.1029/2004GL021815>.
- Montierth, C., Johnston, A.D., and Cashman, K.V., 1995, An empirical glass-composition-based geothermometer for Mauna Loa lavas, *in* Rhodes, J.M. and Lockwood, J.P. eds., *Mauna Loa Revealed—Structure, Composition, History, and Hazards*: American Geophysical Union, p. 207–217.

- Moufti, M.R., Moghazi, A.M., and Ali, K.A., 2012, Geochemistry and Sr–Nd–Pb isotopic composition of the Harrat Al-Madinah Volcanic Field, Saudi Arabia: *Gondwana Research*, v. 21, no. 2, p. 670–689, <https://doi.org/10.1016/j.gr.2011.06.003>.
- Moufti, M.R., Moghazi, A.M., and Ali, K.A., 2013, $^{40}\text{Ar}/^{39}\text{Ar}$ geochronology of the Neogene–Quaternary Harrat Al-Madinah intercontinental volcanic field, Saudi Arabia—Implications for duration and migration of volcanic activity: *Journal of Asian Earth Sciences*, v. 62, p. 253–268, <https://doi.org/10.1016/j.jseae.2012.09.027>.
- Mueller, S., Llewellyn, E.W., and Mader, H.M., 2011, The effect of particle shape on suspension viscosity and implications for magmatic flows: *Geophysical Research Letters*, v. 38, no. L13316, 5 p., <https://doi.org/10.1029/2011GL047167>.
- Murcia, H., Németh, K., El-Masry, N.N., Lindsay, J.M., Moufti, M.R.H., Wameyo, P., Cronin, S.J., Smith, I.E.M., and Kereszturi, G., 2015, The Al-Du'aythah volcanic cones, Al-Madinah City—Implications for volcanic hazards in northern Harrat Rahat, Kingdom of Saudi Arabia: *Bulletin of Volcanology*, v. 77, no. 6, 54 p., <https://doi.org/10.1007/s00445-015-0936-9>.
- Murcia, H., Németh, K., Moufti, M.R., Lindsay, J.M., El-Masry, N., Cronin, S.J., Qaddah, A., and Smith, I.E.M., 2014, Late Holocene lava flow morphotypes of northern Harrat Rahat, Kingdom of Saudi Arabia—Implications for the description of continental lava fields: *Journal of Asian Earth Sciences*, v. 84, p. 131–145, <https://doi.org/10.1016/j.jseae.2013.10.002>.
- Neal, C.A., Brantley, S.R., Antolik, L., Babb, J., Burgess, M., Calles, K., Cappos, M., Chang, J.C., Conway, S., Desmither, L., Dotray, P., Elias, T., Fukunaga, P., Fuke, S., Johanson, I.A., Kamibayashi, K., Kauahikaua, J., Lee, R.L., Pekalib, S., Miklius, A., Million, W., Moniz, C.J., Nadeau, P.A., Okubo, P., Parcheta, C., Patrick, M.R., Shiro, B., Swanson, D.A., Tollett, W., Trusdell, F., Younger, E.F., Zoeller, M.H., Montgomery-Brown, E.K., Anderson, K.R., Poland, M.P., Ball, J., Bard, J., Coombs, M., Dietterich, H.R., Kern, C., Thelen, W.A., Cervelli, P.F., Orr, T., Houghton, B.F., Gansecki, C., Hazlett, R., Lundgren, P., Diefenbach, A.K., Lerner, A.H., Waite, G., Kelly, P., Clor, L., Werner, C., Mulliken, K., and Fisher, G., 2019, The 2018 rift eruption and summit collapse of Kilauea Volcano: *Science*, v. 363, no. 6425, p. 367–374, <https://doi.org/10.1126/science.aav7046>.
- Newman, S., and Lowenstern, J.B., 2002, VolatileCalc—A silicate melt– H_2O – CO_2 solution model written in Visual Basic for excel: *Computers & Geosciences*, v. 28, no. 5, p. 597–604, [https://doi.org/10.1016/S0098-3004\(01\)00081-4](https://doi.org/10.1016/S0098-3004(01)00081-4).
- Pedersen, G.B.M., Höskuldsson, A., Dürig, T., Thordarson, T., Jónsdóttir, I., Riishuus, M.S., Óskarsson, B.V., Dumont, S., Magnusson, E., Gudmundsson, M.T., Sigmundsson, F., Drouin, V.J.P.B., Gallagher, C., Askew, R., Gudnason, J., Moreland, W.M., Nikkola, Rpl, Reynolds, H.I., Schmith, J., and the IES eruption team, 2017, Lava field evolution and emplacement dynamics of the 2014–2015 basaltic fissure eruption at Holuhraun, Iceland: *Journal of Volcanology and Geothermal Research*, v. 340, p. 155–169, <https://doi.org/10.1016/j.jvolgeores.2017.02.027>.
- Peltier, A., Bachèlery, P., and Staudacher, T., 2009, Magma transport and storage at Piton de La Fournaise (La Réunion) between 1972 and 2007—A review of geophysical and geochemical data: *Journal of Volcanology and Geothermal Research*, v. 184, no. 1, p. 93–108, <https://doi.org/10.1016/j.jvolgeores.2008.12.008>.
- Peterson, D.W., and Tilling, R.I., 1980, Transition of basaltic lava from pahoehoe to aa, Kilauea Volcano, Hawaii—Field observations and key factors: *Journal of Volcanology and Geothermal Research*, v. 7, no. 3, p. 271–293, [https://doi.org/10.1016/0377-0273\(80\)90033-5](https://doi.org/10.1016/0377-0273(80)90033-5).
- Pinkerton, H., and Wilson, L., 1994, Factors controlling the lengths of channel-fed lava flows: *Bulletin of Volcanology*, v. 56, no. 2, p. 108–120, <https://doi.org/10.1007/BF00304106>.
- Putirka, K.D., 2008, Thermometers and barometers for volcanic systems: *Reviews in Mineralogy and Geochemistry*, v. 69, no. 1, p. 61–120, <https://doi.org/10.2138/rmg.2008.69.3>.
- Putirka, K.D., Perfit, M., Ryerson, F.J., and Jackson, M.G., 2007, Ambient and excess mantle temperatures, olivine thermometry, and active vs. passive upwelling: *Chemical Geology*, v. 241, no. 3, p. 177–206, <https://doi.org/10.1016/j.chemgeo.2007.01.014>.
- Rhéty, M., Harris, A., Villeneuve, N., Gurioli, L., Médard, E., Chevrel, O., and Bachèlery, P., 2017, A comparison of cooling-limited and volume-limited flow systems—Examples from channels in the Piton de la Fournaise April 2007 lava-flow field: *Geochemistry, Geophysics, Geosystems*, v. 18, no. 9, p. 3270–3291, <https://doi.org/10.1002/2017GC006839>.
- Riker, J.M., Cashman, K.V., Kauahikaua, J.P., and Montierth, C.M., 2009, The length of channelized lava flows—Insight from the 1859 eruption of Mauna Loa Volcano, Hawai'i: *Journal of Volcanology and Geothermal Research*, v. 183, no. 3–4, p. 139–156, <https://doi.org/10.1016/j.jvolgeores.2009.03.002>.
- Robert, B., Harris, A., Gurioli, L., Médard, E., Sehlke, A., and Whittington, A., 2014, Textural and rheological evolution of basalt flowing down a lava channel: *Bulletin of Volcanology*, v. 76, no. 824, 21 p., <https://doi.org/10.1007/s00445-014-0824-8>.

- Sehlke, A., Whittington, A., Robert, B., Harris, A., Gurioli, L., and Médard, E., 2014, Pahoe-hoe to ‘a‘a transition of Hawaiian lavas—An experimental study: *Bulletin of Volcanology*, v. 76, no. 876, 20 p., <https://doi.org/10.1007/s00445-014-0876-9>.
- Shea, T., Houghton, B.F., Gurioli, L., Cashman, K.V., Hammer, J.E., and Hobden, B.J., 2010, Textural studies of vesicles in volcanic rocks—An integrated methodology: *Journal of Volcanology and Geothermal Research*, v. 190, no. 3, p. 271–289, <https://doi.org/10.1016/j.jvolgeores.2009.12.003>.
- Shaw, H.R., 1972, Viscosities of magmatic silicate liquids; an empirical method of prediction: *American Journal of Science*, v. 272, no. 9, p. 870–893, <https://doi.org/10.2475/ajs.272.9.870>.
- Siebert, L., Cottrell, E., Venzke, E., and Andrews, B., 2015, Chapter 12—Earth’s Volcanoes and Their Eruptions; An Overview, in Sigurdsson, H., ed., *The Encyclopedia of Volcanoes* (2d ed.): Academic Press, Amsterdam, p. 239–255, <https://doi.org/10.1016/B978-0-12-385938-9.00012-2>.
- Siebert, L., Simkin, T., and Kimberly, P., 2011, *Volcanoes of the World*: University of California Press, Washington, D.C., 568 p.
- Sisson, T.W., Downs, D.T., Calvert, A.T., Dietterich, H.R., Mahood, G.A., Salters, V.J.M., Stelten, M.E., and Shawali, J., 2023, Mantle origin and crustal differentiation of basalts and hawaiites of northern Harrat Rahat, Kingdom of Saudi Arabia, chap. I of Sisson, T.W., Calvert, A.T., and Mooney, W.D., eds., *Active volcanism on the Arabian Shield—Geology, volcanology, and geophysics of northern Harrat Rahat and vicinity, Kingdom of Saudi Arabia*: U.S. Geological Survey Professional Paper 1862 [also released as Saudi Geological Survey Special Report SGS–SP–2021–1], 42 p., <https://doi.org/10.3133/pp1862I>.
- Sisson, T.W., and Grove, T.L., 1993, Temperatures and H₂O contents of low-MgO high-alumina basalts: *Contributions to Mineralogy and Petrology*, v. 113, no. 2, p. 167–184, <https://doi.org/10.1007/BF00283226>.
- Smith, I.E.M., and Németh, K., 2017, Source to surface model of monogenetic volcanism—A critical review, in Németh, K., Carrasco-Núñez, G., Aranda-Gómez, J.J., and Smith, I.E.M., eds., *Monogenetic volcanism*: Geological Society of London Special Publications, v. 446, p. 1–28, <https://doi.org/10.1144/SP446.14>.
- Solana, M.C., 2012, Development of unconfined historic lava flow fields in Tenerife—Implications for the mitigation of risk from a future eruption: *Bulletin of Volcanology*, v. 74, no. 10, p. 2397–2413, <https://doi.org/10.1007/s00445-012-0670-5>.
- Soldati, A., Beem, J., Gomez, F., Huntley, J.W., Robertson, T., and Whittington, A., 2017, Emplacement dynamics and timescale of a Holocene flow from the Cima Volcanic Field (CA)—Insights from rheology and morphology: *Journal of Volcanology and Geothermal Research*, v. 374, p. 91–111, <https://doi.org/10.1016/j.jvolgeores.2017.09.005>.
- Soldati, A., Harris, A.J.L., Gurioli, L., Villeneuve, N., Rhéty, M., Gomez, F., and Whittington, A., 2018, Textural, thermal, and topographic constraints on lava flow system structure—The December 2010 eruption of Piton de la Fournaise: *Bulletin of Volcanology*, v. 80, no. 74, 19 p., <https://doi.org/10.1007/s00445-018-1246-9>.
- Soule, S.A., Cashman, K.V., and Kauahikaua, J.P., 2004, Examining flow emplacement through the surface morphology of three rapidly emplaced, solidified lava flows, Kilauea Volcano, Hawai‘i: *Bulletin of Volcanology*, v. 66, no. 1, p. 1–14, <https://doi.org/10.1007/s00445-003-0291-0>.
- Stelten, M.E., Downs, D.T., Champion, D.E., Dietterich, H.R., Calvert, A.T., Sisson, T.W., Mahood, G.A., and Zahran, H., 2020, The timing and compositional evolution of volcanism within northern Harrat Rahat, Kingdom of Saudi Arabia: *Geological Society of America Bulletin*, v. 132, no. 7–8, p. 1381–1403, <https://doi.org/10.1130/B35337.1>.
- Stelten, M.E., Downs, D.T., Champion, D.E., Dietterich, H.R., Calvert, A.T., Sisson, T.W., Mahood, G.A., and Zahran, H.M., 2023, Eruptive history of northern Harrat Rahat—Volume, timing, and composition of volcanism over the past 1.2 million years, chap. D of Sisson, T.W., Calvert, A.T., and Mooney, W.D., eds., *Active volcanism on the Arabian Shield—Geology, volcanology, and geophysics of northern Harrat Rahat and vicinity, Kingdom of Saudi Arabia*: U.S. Geological Survey Professional Paper 1862 [also released as Saudi Geological Survey Special Report SGS–SP–2021–1], 46 p., <https://doi.org/10.3133/pp1862D>.
- Stelten, M.E., Downs, D.T., Dietterich, H.R., Mahood, G.A., Calvert, A.T., Sisson, T.W., Zahran, H., and Shawali, J., 2018, Timescales of magmatic differentiation from alkali basalt to trachyte within the Harrat Rahat volcanic field, Kingdom of Saudi Arabia: *Contributions to Mineralogy and Petrology*, v. 173, no. 68, 17 p., <https://doi.org/10.1007/s00410-018-1495-9>.
- Stevens, N.F., 2002, Emplacement of the large andesite lava flow in the Oturere Stream valley, Tongariro Volcano, from airborne interferometric radar: *New Zealand Journal of Geology and Geophysics*, v. 45, no. 3, p. 387–394, <https://doi.org/10.1080/00288306.2002.9514980>.
- Tarquini, S., and de’ Michieli Vitturi, M., 2014, Influence of fluctuating supply on the emplacement dynamics of channelized lava flows: *Bulletin of Volcanology*, v. 76, no. 801, 13 p., <https://doi.org/10.1007/s00445-014-0801-2>.

- Truby, J.M., Mueller, S.P., Llewellyn, E.W., and Mader, H.M., 2015, The rheology of three-phase suspensions at low bubble capillary number: *Proceedings of the Royal Society A*, v. 471, no. 20140557, 18 p., <https://doi.org/10.1098/rspa.2014.0557>.
- Valentine, G.A., and Connor, C.B., 2015, Chapter 23—Basaltic volcanic fields, *in* Sigurdsson, H., ed., *The Encyclopedia of Volcanoes* (2d ed.): Academic Press, Amsterdam, p. 423–439.
- Wadge, G., 1981, The variation of magma discharge during basaltic eruptions: *Journal of Volcanology and Geothermal Research*, v. 11, no. 2, p. 139–168, [https://doi.org/10.1016/0377-0273\(81\)90020-2](https://doi.org/10.1016/0377-0273(81)90020-2).
- Walker, G.P.L., 1971, Compound and simple lava flows and flood basalts: *Bulletin Volcanologique*, v. 35, no. 3, p. 579–590, <https://doi.org/10.1007/BF02596829>.
- Walker, G.P.L., 1973, Mount Etna and the 1973 eruption—Lengths of lava flows: *Philosophical Transactions of the Royal Society of London A*, v. 274, p. 107–118, <https://doi.org/10.1098/rsta.1973.0030>.
- Walker, G.P.L., 2000, Basaltic volcanoes and volcanic systems, *in* Sigurdsson, H., ed., *The Encyclopedia of Volcanoes*: Academic Press, Amsterdam, p. 283–289.
- Wolfe, E.W., Garcia, M.O., Jackson, D.B., Koyanagi, R.Y., Neal, C.A., and Okamura, A.T., 1987, The Puu Oo Eruption of Kilauea Volcano, episodes 1–20, January 3, 1983, to June 8, 1984, *in* Decker, R.W., Wright, T.L., and Stauffer, P.H., eds., *Volcanism in Hawaii*: U.S. Geological Survey Professional Paper 1350, p. 471–508.

Appendixes 1–6

Appendix 1. Samples for X-ray Fluorescence Analysis

[Locations are in World Geodetic System of 1984 Universal Transverse Mercator zone 37R coordinates]

Sample	Easting	Northing
Basalt of Al Labah (1256 C.E.)		
R14AC056	579189	2693655
R15DD150A	577175	2697425
R14TS012	573283	2704764
R14TS093	576082	2695967
R14TS096	578490	2695914
R14TS097	577423	2696155
R14TS098	577456	2696076
R14TS100	576357	2701088
R14TS102	576852	2703743
R14TS103	577161	2704116
R14TS104	577619	2704619
R14TS142	571589	2709371
Basalt of Northern Fingers		
R15DD011	579906	2705336
R15DD018	583909	2693556
R14DS079	584099	2693699
R14DS082	584011	2693396
R15DS097	580618	2701714
R15DS099	583582	2694555
R15DS100	584075	2696024
R14TS017	583162	2698065
R14TS019	586138	2697339
R14TS020	586141	2697340
Basalt of Central Finger		
R14AC008	585651	2691695
R14AC009	586015	2691406
R14TS011	586070	2691222
R14TS024	591246	2700451
R16MS071	586185	2691972
Basalt of Southern Fingers		
R14AC005	587854	2686827
R14AC006	589290	2687752
R14AC007	590079	2689116
R15DD019	587600	2686651
R15DD022	592104	2689983
R15DD025	597563	2691822
R15DS101	587627	2686488
R15DS105	595916	2690209
R14TS008	588179	2686472
R14TS026	600012	2697759

Appendix 2. Samples for Textural Analysis

[Locations are in World Geodetic System of 1984 Universal Transverse Mercator zone 37R coordinates]

Sample	Easting	Northing	Glassy?
Basalt of Al Labah (1256 C.E.)			
R14TS95	579120	2694140	Yes
R15DD010	575198	2707364	Yes
R15DD012	576644	2705208	Yes
R15DD015	576966	2699590	Yes
R15DD016	578810	2692453	No
R15DD150B	577175	2697425	Yes
R15DS98	578913	2692667	No
R16HD010	572518	2713603	Yes
Basalt of Northern Fingers			
R15DD011	579906	2705336	No
R15DD013	578925	2703018	No
R15DD014	580314	2701426	Yes
R15DD017	583909	2693556	No
R15DD018	584014	2693617	Yes
R15DS100	584075	2696024	No
R15DS97	580618	2701714	No
R15DS99	583582	2694555	No
Basalt of Central Finger			
R16HD001	585482	2691196	Yes
R16HD012A	585341	2691771	No
R16HD012B	585341	2691771	No
R16HD013	586815	2693696	Yes
R16HD014	586070	2692055	Yes
R16HD015	588512	2695074	Yes
R16HD016	589369	2698263	Yes
R16HD017	590124	2703219	No
Basalt of Southern Fingers			
R15DD019	587600	2686651	No
R15DD021	589212	2687569	No
R15DD022	592104	2689983	No
R15DD025	597563	2691822	No
R15DS101	587627	2686488	No
R15DS105	595916	2690209	No
R16HD009	585750	2687104	Yes
R16HD018	588202	2687903	No
R16HD026	585793	2688207	Yes
R16HD027	585793	2688207	Yes
R16HD28A	587549	2690040	No

Appendix 3. Microprobe Analyses of Glass in Harrat Rahat Basaltic Lava Flows

[Values in weight percent. All iron reported as FeO (FeO*). -, not analyzed]

SiO ₂	TiO ₂	Al ₂ O ₃	FeO*	MnO	MgO	CaO	Na ₂ O	K ₂ O	Cl	P ₂ O ₅	Total
Basalt of Al Labah (1256 C.E.)											
Sample R14TS95 (51 analyses)											
46.1	3.37	16.3	13.5	0.20	5.23	8.56	4.30	0.97	-	1.16	99.7
46.0	3.30	16.2	13.2	0.20	4.92	8.63	4.17	0.99	-	1.01	98.5
47.1	3.22	16.4	13.0	0.15	5.26	8.64	4.36	1.07	-	1.28	100.4
48.0	3.22	16.2	13.2	0.11	4.96	8.11	4.48	1.01	-	1.00	100.2
46.8	3.20	15.9	12.9	0.15	5.00	8.69	4.16	0.95	-	1.09	98.8
47.8	2.98	16.3	12.6	0.17	5.22	8.59	4.02	1.00	-	1.17	99.8
48.1	3.25	16.4	13.0	0.26	5.04	8.74	4.35	1.05	-	1.31	101.5
47.7	3.38	16.9	12.7	0.34	5.32	8.83	4.54	1.01	-	1.15	101.9
47.5	2.91	16.5	12.2	0.28	5.00	8.12	4.45	1.12	-	1.00	99.0
46.7	2.92	16.1	13.1	0.29	5.21	8.37	4.17	0.95	-	1.02	98.7
47.3	2.96	15.7	13.2	0.26	5.37	8.41	4.34	1.00	-	1.17	99.8
47.1	3.46	16.5	12.8	0.15	5.54	8.76	4.48	0.98	-	0.94	100.7
47.8	3.19	16.9	12.5	0.28	5.31	8.54	3.93	1.02	-	0.99	100.5
47.7	3.14	16.2	12.6	0.21	5.66	8.77	4.35	0.99	-	1.01	100.5
47.2	2.75	16.1	12.6	0.18	5.51	8.59	3.88	0.82	-	1.19	98.8
47.5	2.86	16.7	12.5	0.08	5.50	8.39	4.20	1.00	-	1.18	99.9
46.9	3.41	16.7	12.8	0.19	5.66	8.43	4.52	0.97	-	1.01	100.6
47.9	2.96	16.3	13.1	0.28	5.24	8.50	4.47	0.92	-	1.23	100.8
47.2	3.12	16.6	12.9	0.15	5.25	8.32	4.22	1.03	-	1.07	99.8
47.9	3.25	16.5	12.7	0.25	5.17	8.72	4.69	0.84	-	1.00	101.0
47.4	3.12	16.5	13.3	0.25	5.18	8.28	4.53	0.95	-	1.24	100.7
47.5	3.06	16.7	12.8	0.25	5.52	8.49	5.08	0.93	-	1.24	101.6
48.0	3.13	16.8	13.4	0.22	5.22	8.32	4.11	1.03	-	1.15	101.3
47.5	3.09	16.3	12.4	0.21	5.14	8.86	4.39	1.01	-	1.15	99.9
47.6	3.19	16.2	13.1	0.19	5.39	8.63	4.26	0.97	-	1.30	100.7
47.1	3.46	16.2	12.9	0.14	5.43	8.41	4.54	0.99	-	0.95	100.2
46.7	3.17	16.4	12.8	0.20	5.04	8.72	3.88	1.03	-	1.14	99.1
46.8	3.01	16.5	12.8	0.20	4.82	8.95	4.01	1.06	-	1.06	99.2
47.2	2.89	15.7	13.7	0.14	5.21	8.22	4.36	0.93	-	1.01	99.3
47.3	3.15	15.2	13.1	0.35	7.05	7.90	4.50	0.92	-	1.07	100.6
47.4	3.06	16.0	13.3	0.20	4.88	8.23	4.67	1.00	-	1.28	100.1
47.5	3.36	16.0	13.3	0.24	5.12	8.52	4.21	1.11	-	1.15	100.5
47.8	3.36	16.3	12.9	0.22	5.02	8.38	3.84	0.92	-	1.22	100.0
47.1	2.64	16.5	13.1	0.16	5.41	8.90	4.68	1.07	-	1.17	100.8
47.3	2.99	16.5	13.3	0.21	4.93	8.42	4.07	1.06	-	0.99	99.7
47.0	3.08	16.8	13.2	0.23	5.10	8.23	4.54	1.02	-	0.98	100.1
46.5	2.83	16.5	13.3	0.26	4.96	8.27	4.44	1.00	-	1.22	99.3
46.7	3.12	16.6	12.9	0.15	5.23	8.59	4.33	1.01	-	1.17	99.8

SiO ₂	TiO ₂	Al ₂ O ₃	FeO*	MnO	MgO	CaO	Na ₂ O	K ₂ O	Cl	P ₂ O ₅	Total
Basalt of Al Labah (1256 C.E.)—Continued											
Sample R14TS95 (51 analyses)—Continued											
46.8	3.52	16.1	13.0	0.21	5.29	8.75	4.44	1.04	-	1.19	100.4
46.4	3.39	16.3	13.5	0.26	5.29	8.41	4.66	0.98	-	1.11	100.2
46.5	2.95	16.3	13.1	0.20	5.47	8.19	4.16	1.06	-	1.16	99.2
46.8	3.15	15.9	12.8	0.22	5.37	8.17	4.46	1.19	-	1.08	99.2
47.2	3.13	16.3	13.7	0.19	5.11	8.54	4.49	0.90	-	1.07	100.7
47.3	3.39	16.2	13.4	0.28	5.68	8.47	4.36	0.98	-	0.94	101.0
47.7	3.07	16.3	12.6	0.25	5.32	8.83	4.42	0.98	-	1.12	100.6
46.8	3.10	16.2	13.5	0.16	5.57	8.46	4.28	0.99	-	1.01	100.0
47.0	3.11	16.4	13.1	0.23	5.59	8.41	4.30	0.95	-	1.19	100.3
46.6	3.06	16.3	13.3	0.20	5.35	8.63	3.95	0.98	-	1.18	99.5
47.4	3.37	16.3	13.0	0.15	5.27	8.38	3.95	0.92	-	1.12	99.9
47.7	3.01	16.8	12.9	0.24	5.20	8.94	3.92	0.85	-	0.99	100.5
46.7	2.78	16.5	13.0	0.24	5.66	8.28	4.47	0.98	-	0.94	99.6
Sample R15DD150B (11 analyses)											
46.1	3.88	14.7	13.8	0.24	5.34	9.82	3.61	0.80	0.04	0.61	98.9
46.6	3.82	14.9	13.8	0.13	5.28	9.92	4.15	0.81	0.01	0.54	99.9
46.4	3.60	15.1	13.2	0.21	5.18	10.2	3.97	0.79	0.03	0.62	99.2
46.5	3.54	14.8	14.1	0.24	5.45	10.1	3.70	0.75	0.00	0.67	99.9
46.5	3.68	14.7	13.8	0.38	5.31	9.91	3.76	0.84	0.02	0.59	99.5
46.4	3.88	15.0	14.1	0.39	5.48	9.56	3.51	0.99	0.03	0.60	99.9
46.2	3.90	14.7	13.3	0.21	5.42	10.3	4.01	0.83	0.01	0.54	99.4
45.7	3.78	14.5	13.3	0.35	6.36	9.26	4.38	0.81	0.04	0.61	99.2
46.6	3.52	14.8	13.3	0.19	5.42	9.92	4.13	0.79	0.03	0.59	99.2
46.7	3.89	14.7	13.5	0.34	5.36	10.0	4.22	0.81	0.00	0.61	100.1
46.7	3.67	14.7	13.1	0.38	5.62	10.0	4.08	0.81	0.00	0.57	99.6
Sample R15DD015 (15 analyses)											
46.9	4.13	15.1	14.0	0.26	4.14	8.56	4.25	1.81	0.00	1.63	100.8
46.6	4.16	15.0	12.8	0.19	3.56	8.94	4.25	1.88	0.00	1.74	99.1
46.5	4.54	15.3	12.9	0.43	3.84	8.67	4.53	1.94	0.02	1.75	100.4
45.9	4.18	14.9	12.9	0.34	3.48	9.75	4.60	2.02	0.00	1.74	99.9
45.5	4.04	15.1	13.9	0.37	4.21	8.61	4.17	1.85	0.02	1.74	99.5
45.7	4.45	14.7	13.7	0.31	3.38	9.61	4.75	1.84	0.05	1.74	100.2
45.9	3.62	15.0	13.6	0.40	3.92	9.28	4.51	1.79	0.05	1.67	99.7
45.1	3.82	14.3	13.1	0.33	3.05	10.2	4.98	2.13	0.01	1.69	98.6
44.0	4.04	14.3	12.7	0.38	3.46	9.93	4.22	2.01	0.03	1.76	96.7
43.9	3.98	14.2	13.6	0.36	3.78	9.42	4.43	1.85	0.03	1.74	97.3
45.2	4.32	15.0	14.4	0.36	4.33	8.19	3.91	1.61	0.05	1.62	99.0
45.9	4.33	14.5	14.0	0.38	4.40	8.61	3.55	1.39	0.06	1.73	98.9
46.6	3.96	14.9	14.5	0.23	4.46	8.29	4.00	1.59	0.03	1.61	100.2
46.5	3.99	14.8	14.9	0.16	4.52	8.53	3.53	1.44	0.05	1.63	100.0
45.6	4.00	14.7	14.4	0.22	4.42	8.37	4.06	1.38	0.04	1.67	98.9
Sample R15DD012 (15 analyses)											
45.0	3.95	14.7	14.0	0.43	4.50	8.59	3.94	1.37	0.05	1.63	98.1
45.3	3.99	15.0	14.0	0.31	4.59	8.27	4.10	1.42	0.03	1.65	98.6

SiO ₂	TiO ₂	Al ₂ O ₃	FeO*	MnO	MgO	CaO	Na ₂ O	K ₂ O	Cl	P ₂ O ₅	Total
Basalt of Al Labah (1256 C.E.)—Continued											
Sample R15DD012 (15 analyses)—Continued											
45.1	4.25	15.0	13.8	0.24	4.61	8.51	4.50	1.39	0.03	1.65	99.1
45.5	3.52	14.6	14.0	0.28	4.19	8.33	4.21	1.41	0.01	1.70	97.7
45.2	4.13	15.1	14.0	0.23	4.44	8.74	4.18	1.30	0.02	1.69	99.0
45.8	3.82	14.5	14.0	0.16	4.41	8.33	4.24	1.38	0.03	1.54	98.3
46.1	3.93	15.1	14.5	0.32	4.69	8.64	4.54	1.35	0.05	1.75	101.0
45.7	4.04	14.6	13.9	0.35	4.40	8.52	3.20	1.36	0.00	1.76	97.8
46.4	3.51	15.1	14.3	0.13	4.50	8.39	4.10	1.40	0.01	1.73	99.5
46.1	3.93	15.0	14.4	0.36	4.39	8.54	3.85	1.33	0.02	1.64	99.5
45.7	4.14	14.9	14.3	0.32	4.42	8.49	4.24	1.37	0.04	1.60	99.5
45.2	4.02	14.7	14.9	0.22	4.33	8.49	3.38	1.27	0.00	1.63	98.1
46.1	4.14	15.0	13.6	0.14	4.53	8.54	3.25	1.40	0.05	1.72	98.4
46.4	3.72	14.9	14.0	0.21	4.48	8.59	3.16	1.38	0.02	1.70	98.5
44.7	3.97	15.1	13.4	0.22	4.45	8.21	3.60	1.44	0.03	1.67	96.7
Sample R15DD010 (15 analyses)											
46.5	3.74	15.5	13.6	0.28	4.84	8.84	4.17	1.06	0.00	1.23	99.7
47.0	3.87	16.1	13.7	0.32	4.87	8.87	4.00	1.10	0.03	1.15	100.9
47.5	3.82	16.2	14.0	0.35	4.79	8.36	3.97	1.64	0.00	1.32	101.9
47.7	3.85	16.4	14.3	0.30	4.97	8.82	3.56	1.58	0.00	1.25	102.7
46.8	3.62	15.7	14.9	0.31	5.24	8.23	3.48	1.44	0.02	1.29	101.0
47.5	3.72	15.7	14.6	0.27	5.27	7.68	4.34	1.77	0.01	1.24	102.1
47.4	3.69	15.9	14.9	0.33	5.02	8.27	3.93	1.74	0.00	1.26	102.3
47.0	3.62	16.0	14.2	0.23	4.73	8.38	3.71	1.48	0.01	1.33	100.8
47.3	3.75	16.3	14.0	0.24	4.93	9.18	3.64	1.36	0.03	1.30	102.0
47.9	3.59	16.4	13.6	0.26	5.15	9.02	3.29	1.28	0.04	1.23	101.8
47.0	3.86	14.6	15.5	0.18	5.04	8.79	3.77	1.44	0.07	1.30	101.5
47.7	3.94	15.8	13.9	0.24	5.03	9.41	3.82	0.58	0.05	1.28	101.6
47.2	3.78	15.8	14.2	0.32	5.05	8.97	3.62	1.21	0.00	1.16	101.3
47.4	3.66	16.2	13.8	0.24	4.84	9.19	3.89	1.13	0.00	1.26	101.7
46.9	3.71	16.4	14.3	0.35	4.93	8.65	4.53	1.15	0.00	1.23	102.0
Sample R16HD010 (5 analyses)											
48.1	4.47	13.8	15.3	0.30	4.09	10.6	4.52	2.22	0.03	1.27	104.6
47.5	4.68	12.4	16.0	0.19	4.24	11.1	3.74	1.79	0.03	1.29	103.0
46.8	4.91	14.5	16.4	0.15	3.11	9.98	3.74	1.06	0.00	1.05	101.7
47.9	4.21	15.3	14.7	0.40	2.28	9.18	4.06	1.74	0.08	0.99	100.8
48.4	4.52	15.1	13.7	0.29	3.74	10.5	3.99	1.78	0.05	1.00	103.0
Basalt of Northern Fingers											
Sample R15DD018 (13 analyses)											
47.5	5.26	14.5	15.04	0.29	4.69	7.04	2.69	1.56	0.00	0.72	99.28
47.5	5.48	14.7	15.32	0.24	4.74	7.34	2.81	1.34	0.00	0.67	100.14
47.5	5.30	14.3	14.56	0.24	4.85	7.52	2.69	1.42	0.04	0.73	99.11
47.9	5.46	14.4	16.37	0.34	4.61	4.73	4.34	1.61	0.04	0.61	100.38
47.6	5.19	14.3	14.35	0.38	4.42	5.87	3.98	1.78	0.05	0.67	98.58
47.0	5.31	14.2	14.43	0.08	5.18	8.37	3.98	0.61	0.00	0.64	99.71
48.5	5.71	14.6	15.33	0.34	4.18	5.70	3.86	1.92	0.03	0.71	100.87

SiO ₂	TiO ₂	Al ₂ O ₃	FeO*	MnO	MgO	CaO	Na ₂ O	K ₂ O	Cl	P ₂ O ₅	Total
Basalt of Northern Fingers—Continued											
Sample R15DD018 (13 analyses)—Continued											
47.6	4.86	14.1	16.94	0.23	3.96	6.57	4.45	1.09	0.02	0.72	100.55
46.7	4.88	14.1	13.49	0.25	4.55	10.60	3.64	0.54	0.03	0.72	99.48
47.2	4.81	14.5	15.22	0.34	4.75	9.52	1.44	1.14	0.04	0.82	99.69
48.3	4.92	14.5	14.07	0.23	4.74	9.39	1.85	1.08	0.00	0.77	99.76
47.4	4.96	14.4	14.42	0.35	4.55	9.54	1.35	1.14	0.00	0.70	98.80
47.7	5.62	14.5	14.78	0.16	4.60	8.55	2.07	1.38	0.01	0.81	100.20
Sample R15DD014 (9 analyses)											
45.5	4.77	15.8	13.9	0.38	4.67	8.40	3.73	1.32	0.06	0.66	99.4
46.0	4.76	15.5	15.2	0.09	4.25	9.19	3.93	0.87	0.02	0.64	100.6
46.5	5.04	15.5	14.5	0.24	4.44	8.87	4.12	0.89	0.06	0.63	100.8
46.2	5.60	15.3	15.1	0.28	4.86	8.99	3.78	0.59	0.03	0.71	101.6
45.9	4.91	15.0	16.4	0.30	4.81	7.25	4.20	1.43	0.00	0.59	100.9
46.0	5.04	15.0	14.9	0.22	5.24	10.2	3.78	0.74	0.00	0.64	101.8
46.5	5.01	15.6	14.0	0.22	4.88	8.24	3.62	1.25	0.06	0.70	100.2
46.9	5.19	15.6	14.3	0.30	4.64	8.47	3.17	1.26	0.02	0.74	100.7
46.1	4.80	15.5	14.9	0.14	4.97	8.67	2.67	1.26	0.03	0.71	99.8
Basalt of Central Finger											
Sample R16HD01 (15 analyses)											
45.3	3.84	15.2	16.9	0.26	8.60	6.14	4.21	0.43	0.00	0.48	101.3
46.6	4.94	16.7	12.7	0.21	4.81	9.52	3.77	0.46	0.03	0.64	100.4
47.8	3.86	16.6	11.8	0.25	5.47	8.95	4.70	0.57	0.04	0.44	100.5
47.3	4.66	16.5	14.0	0.21	5.42	9.25	3.88	0.80	0.04	0.65	102.7
44.0	5.28	15.0	16.6	0.32	6.79	6.56	3.77	2.38	0.02	0.52	101.3
47.1	4.09	17.0	14.2	0.31	4.69	4.53	5.55	1.50	0.02	0.47	99.4
46.5	4.24	16.3	13.4	0.22	5.96	8.18	3.75	0.76	0.02	0.66	99.9
47.1	4.28	16.3	10.2	0.00	4.75	10.5	3.91	1.39	0.05	0.68	99.1
47.4	4.56	16.2	13.5	0.21	5.50	7.61	3.51	1.54	0.03	0.50	100.6
47.4	4.45	16.9	12.5	0.07	4.67	8.68	4.76	0.39	0.05	0.54	100.4
47.3	4.36	16.3	13.5	0.25	5.37	7.89	3.28	1.38	0.05	0.60	100.2
47.0	4.75	16.7	12.7	0.26	4.83	8.81	4.44	0.27	0.02	0.53	100.3
47.1	4.44	16.3	12.3	0.18	4.76	9.46	4.18	0.75	0.02	0.62	100.2
47.9	4.41	16.6	11.8	0.13	5.08	8.57	4.67	0.60	0.03	0.59	100.3
47.5	3.88	17.8	12.2	0.03	4.38	9.73	3.81	0.28	0.03	0.49	100.1
Sample R16HD14 (13 analyses)											
44.3	6.69	12.9	17.4	0.28	5.33	8.60	3.06	1.28	0.04	0.75	100.59
46.0	5.01	14.7	14.9	0.24	4.38	9.15	2.00	1.28	0.04	0.74	98.32
45.8	5.19	14.9	14.3	0.19	4.94	9.22	2.30	1.17	0.06	0.65	98.65
46.3	6.02	14.6	15.3	0.31	4.41	9.13	2.07	1.26	0.02	0.72	100.11
46.5	5.51	14.5	15.9	0.09	4.09	9.92	1.69	1.19	0.07	0.80	100.23
46.3	5.13	15.0	15.0	0.34	4.60	8.75	1.96	1.27	0.00	0.65	98.99
46.4	5.10	15.1	15.1	0.31	4.48	8.87	1.62	1.18	0.02	0.69	98.85
46.7	5.25	14.9	14.9	0.38	4.41	8.72	2.13	1.35	0.00	0.74	99.41
46.3	5.86	14.7	15.2	0.43	4.39	9.21	2.76	1.14	0.05	0.74	100.73
46.0	5.49	14.7	14.6	0.32	4.03	9.24	2.34	1.36	0.09	0.79	98.91

SiO ₂	TiO ₂	Al ₂ O ₃	FeO*	MnO	MgO	CaO	Na ₂ O	K ₂ O	Cl	P ₂ O ₅	Total
Basalt of Central Finger—Continued											
Sample R16HD14 (13 analyses)—Continued											
46.1	5.35	14.7	15.5	0.46	3.97	9.32	1.95	1.20	0.00	0.68	99.18
46.6	5.20	15.1	14.6	0.38	4.45	8.78	1.92	1.17	0.05	0.71	98.89
46.0	5.00	14.2	14.4	0.14	4.94	8.46	3.37	1.53	0.08	0.69	98.79
Sample R16HD13 (11 analyses)											
42.9	4.40	12.7	14.2	0.26	4.67	10.4	4.35	0.78	0.00	0.58	95.2
42.7	4.63	12.3	16.8	0.36	4.08	7.96	3.80	2.34	0.02	0.61	95.6
44.3	4.69	10.8	12.9	0.33	6.48	12.8	2.70	1.25	0.03	0.74	97.0
43.2	4.69	12.4	16.3	0.40	4.72	9.41	3.39	1.55	0.03	0.63	96.7
43.3	4.98	11.1	12.4	0.39	5.90	13.8	2.68	1.22	0.03	0.70	96.5
44.5	4.19	12.5	14.6	0.33	4.30	10.4	3.38	2.07	0.03	0.68	97.0
47.1	4.65	12.7	12.2	0.29	4.61	14.5	3.28	0.62	0.02	0.78	100.7
46.2	4.36	11.8	15.4	0.31	4.63	10.44	2.78	1.94	0.01	0.62	98.6
47.1	4.38	12.4	13.9	0.26	5.42	10.55	3.09	1.90	0.00	0.60	99.6
44.3	5.84	10.7	19.0	0.35	5.53	10.07	2.60	1.67	0.03	0.70	100.8
46.1	4.71	13.2	12.1	0.22	4.64	11.90	3.22	2.14	0.03	0.67	99.0
Sample R16HD15 (10 analyses)											
50.5	4.57	13.0	7.79	0.22	4.74	11.29	2.46	2.14	0.02	1.23	98.0
49.8	5.62	12.1	12.94	0.31	2.17	6.85	2.50	3.10	0.03	1.36	96.7
52.2	6.12	13.1	10.68	0.34	2.62	5.22	4.42	2.37	0.06	1.32	98.4
53.4	3.64	14.7	8.92	0.27	3.90	9.06	5.29	0.93	0.03	1.06	101.1
54.5	3.30	15.8	8.18	0.20	2.51	4.99	4.21	3.16	0.04	1.03	97.9
52.3	3.86	15.1	11.67	0.20	2.52	4.80	4.95	1.52	0.02	1.09	98.0
53.9	3.84	14.9	9.21	0.15	2.63	4.38	3.08	3.66	0.06	1.23	97.0
50.9	5.15	14.0	12.09	0.23	2.54	3.72	4.06	3.39	0.05	1.00	97.1
50.7	5.36	13.1	9.77	0.34	3.88	10.74	3.00	2.27	0.04	1.02	100.3
52.6	4.43	14.9	10.11	0.24	2.02	7.94	5.75	0.94	0.02	0.88	99.8
Sample R16HD16 (9 analyses)											
49.2	5.10	13.1	15.88	0.34	2.49	4.14	3.55	3.06	0.04	1.25	98.1
51.9	5.79	14.4	7.48	0.33	1.81	4.82	5.57	3.61	0.07	1.69	97.5
46.4	5.68	10.9	11.14	0.27	5.10	13.53	2.37	1.74	0.04	1.10	98.3
46.6	5.55	12.0	15.49	0.30	2.94	8.37	3.43	2.86	0.05	0.92	98.5
47.3	5.12	13.0	9.83	0.21	4.85	12.69	3.42	2.30	0.03	0.90	99.6
54.0	4.98	13.9	8.38	0.25	2.12	4.14	5.92	2.81	0.06	1.70	98.2
48.4	4.92	14.5	12.63	0.17	2.44	8.92	2.87	2.17	0.02	0.92	98.0
48.8	5.68	12.0	14.89	0.34	3.79	8.73	3.02	2.43	0.03	1.99	101.7
47.7	6.19	12.5	11.33	0.33	4.60	10.22	3.58	2.11	0.03	1.57	100.2
Basalt of Southern Fingers											
Sample R16HD09 (15 analyses)											
46.9	3.55	15.1	12.2	0.10	6.89	11.5	3.67	0.95	0.02	0.60	101.6
46.5	3.06	15.2	15.8	0.29	5.20	8.28	4.61	1.43	0.05	0.52	101.0
46.6	3.74	15.6	11.9	0.14	5.36	12.0	3.46	0.37	0.01	0.53	99.7
47.5	3.24	15.9	14.3	0.33	8.01	8.3	3.81	0.36	0.03	0.52	102.3
47.0	4.07	14.5	14.8	0.18	5.49	10.9	3.34	0.56	0.01	0.69	101.5
47.7	4.08	15.4	14.0	0.15	5.95	10.7	2.23	0.51	0.00	0.55	101.3

SiO ₂	TiO ₂	Al ₂ O ₃	FeO*	MnO	MgO	CaO	Na ₂ O	K ₂ O	Cl	P ₂ O ₅	Total
Basalt of Southern Fingers—Continued											
Sample R16HD09 (15 analyses)—Continued											
46.8	3.62	15.3	14.1	0.44	5.48	10.1	2.73	0.80	0.05	0.52	99.9
47.6	3.81	15.9	13.6	0.19	6.10	10.1	2.99	0.75	0.00	0.56	101.5
47.8	3.90	15.6	13.2	0.56	6.45	11.1	2.72	0.54	0.01	0.57	102.4
47.1	3.54	15.1	14.8	0.45	5.90	9.62	4.11	0.81	0.00	0.60	102.0
46.9	4.03	15.5	13.4	0.22	5.93	11.4	3.32	0.63	0.08	0.57	101.9
47.5	3.44	15.8	12.3	0.22	6.37	11.2	3.14	0.53	0.04	0.63	101.2
47.1	3.46	15.71	15.30	0.36	5.51	9.62	4.18	0.69	0.00	0.60	102.6
46.8	3.66	15.56	14.07	0.19	6.83	9.15	3.48	0.42	0.02	0.58	100.8
47.9	4.22	15.91	13.60	0.20	4.74	10.30	1.87	1.01	0.03	0.61	100.4
Sample R16HD27 (15 analyses)											
46.1	3.88	14.7	13.8	0.24	5.34	9.82	3.61	0.80	0.04	0.61	98.9
46.6	3.82	14.9	13.8	0.13	5.28	9.92	4.15	0.81	0.01	0.54	99.9
46.4	3.60	15.1	13.2	0.21	5.18	10.16	3.97	0.79	0.03	0.62	99.2
46.5	3.54	14.8	14.1	0.24	5.45	10.13	3.70	0.75	0.00	0.67	99.9
46.5	3.68	14.7	13.8	0.38	5.31	9.91	3.76	0.84	0.02	0.59	99.5
46.4	3.88	15.0	14.1	0.39	5.48	9.56	3.51	0.99	0.03	0.60	99.9
46.2	3.90	14.7	13.3	0.21	5.42	10.27	4.01	0.83	0.01	0.54	99.4
45.7	3.78	14.5	13.3	0.35	6.36	9.26	4.38	0.81	0.04	0.61	99.2
46.6	3.52	14.8	13.3	0.19	5.42	9.92	4.13	0.79	0.03	0.59	99.2
46.7	3.89	14.7	13.5	0.34	5.36	10.03	4.22	0.81	0.00	0.61	100.1
46.7	3.67	14.7	13.1	0.38	5.62	10.00	4.08	0.81	0.00	0.57	99.6
46.8	3.63	14.9	13.0	0.24	5.48	10.02	3.84	0.77	0.00	0.65	99.3
46.6	3.76	14.6	13.5	0.34	5.60	10.22	4.42	0.83	0.02	0.69	100.6
46.9	3.62	14.8	13.3	0.52	5.57	10.12	4.09	0.75	0.03	0.54	100.2
45.8	3.70	14.4	13.2	0.27	5.41	10.06	3.94	0.85	0.04	0.58	98.3
Sample R16HD26 (12 analyses)											
46.0	5.43	11.2	13.3	0.37	4.49	15.1	2.50	1.15	0.04	0.97	100.6
47.4	4.38	12.0	16.3	0.32	2.59	10.1	4.41	2.15	0.02	0.89	100.5
48.0	5.56	9.54	14.2	0.33	2.21	14.1	3.07	1.61	0.00	1.07	99.7
45.0	6.45	9.62	13.6	0.25	4.91	16.4	2.04	1.17	0.05	0.94	100.4
48.7	4.47	14.0	9.99	0.26	4.60	14.1	3.72	1.40	0.00	0.71	101.9
47.4	4.89	13.6	10.6	0.34	4.13	14.0	3.14	1.42	0.01	0.85	100.3
49.0	4.32	15.7	8.73	0.36	4.80	13.8	3.38	0.56	0.05	0.72	101.3
51.0	5.06	10.7	12.6	0.35	2.90	11.1	3.94	1.86	0.00	1.40	101.0
46.7	4.64	16.8	17.4	0.30	1.06	5.27	5.03	1.07	0.05	0.33	98.6
43.6	5.81	9.24	12.2	0.26	8.64	19.8	1.17	0.12	0.00	0.81	101.6
47.4	4.67	13.9	14.9	0.40	3.46	7.85	6.17	1.88	0.03	0.79	101.5
47.3	4.68	15.6	19.1	0.41	2.55	6.36	6.01	0.97	0.02	0.47	103.4

Appendix 4. Microprobe Analyses of Plagioclase in Harrat Rahat Basaltic Lava Flows

[Values in weight percent. All iron reported as FeO (FeO*). -, not analyzed]

SiO ₂	TiO ₂	Al ₂ O ₃	FeO*	MnO	MgO	CaO	Na ₂ O	K ₂ O	BaO	SrO	Total
Basalt of Al Labah (1256 C.E.)											
Sample R14TS95 (21 analyses)											
53.1	-	29.4	0.91	-	0.13	12.7	4.83	0.22	-	-	101.3
53.3	-	29.4	0.97	-	0.19	12.3	4.27	0.23	-	-	100.7
52.6	-	29.4	0.87	-	0.14	12.4	4.65	0.30	-	-	100.3
52.7	-	28.0	1.55	-	0.48	11.9	4.66	0.33	-	-	99.6
53.6	-	28.6	1.08	-	0.18	11.4	4.90	0.32	-	-	100.1
52.9	-	28.7	1.18	-	0.31	12.1	4.55	0.27	-	-	99.9
53.9	-	28.4	0.97	-	0.14	11.7	5.01	0.31	-	-	100.4
53.3	-	28.3	0.79	-	0.13	11.8	4.73	0.25	-	-	99.3
53.6	-	28.7	0.89	-	0.13	11.9	5.01	0.27	-	-	100.5
53.2	-	28.7	0.79	-	0.14	12.0	4.47	0.26	-	-	99.5
53.2	-	28.6	0.74	-	0.14	12.0	4.66	0.22	-	-	99.6
52.7	-	27.0	2.40	-	0.87	11.6	4.81	0.36	-	-	99.7
52.4	-	27.6	1.95	-	0.62	12.0	4.66	0.30	-	-	99.6
52.7	-	27.2	1.86	-	0.68	12.0	4.77	0.31	-	-	99.4
53.4	-	28.9	0.88	-	0.18	12.4	4.78	0.24	-	-	100.8
53.9	-	28.7	0.99	-	0.11	11.9	4.81	0.23	-	-	100.6
53.0	-	29.3	1.03	-	0.16	12.6	4.44	0.24	-	-	100.8
53.0	-	28.9	1.08	-	0.17	12.3	4.27	0.20	-	-	99.9
52.8	-	29.1	1.00	-	0.12	12.5	4.36	0.24	-	-	100.1
53.5	-	29.0	0.95	-	0.21	12.5	4.68	0.27	-	-	101.0
53.2	-	28.4	1.13	-	0.21	12.0	4.74	0.32	-	-	100.0
Sample R15DD150B (7 analyses)											
50.5	0.16	30.4	0.60	0.07	0.30	14.4	3.14	0.07	0.06	0.04	99.8
49.9	0.30	29.2	1.21	0.11	0.78	14.5	2.98	0.10	0.05	0.06	99.2
51.4	0.16	30.4	0.61	0.01	0.30	14.3	3.21	0.07	0.03	0.07	100.4
50.2	0.21	29.3	1.45	0.04	0.42	13.9	3.23	0.25	0.11	0.08	99.2
50.5	0.19	29.5	0.80	0.02	0.35	13.9	3.39	0.08	0.08	0.14	98.9
49.9	0.10	30.3	0.63	0.02	0.20	14.5	3.16	0.07	0.00	0.06	99.0
49.6	0.10	30.5	0.53	0.05	0.19	14.9	2.93	0.07	0.00	0.04	98.9
Sample R15DD015 (15 analyses)											
53.7	0.20	28.0	0.90	0.05	0.09	11.4	5.00	0.28	0.06	0.20	99.9
55.0	0.24	27.4	0.70	0.05	0.09	10.9	5.35	0.27	0.09	0.07	100.2
53.5	0.29	28.3	0.93	0.12	0.13	11.9	4.36	0.21	0.06	0.45	100.2
52.4	0.21	28.6	0.67	0.09	0.12	12.6	4.04	0.19	0.00	0.05	98.9
54.3	0.18	28.2	0.58	0.00	0.10	11.4	5.09	0.27	0.07	0.50	100.8
54.0	0.21	28.1	0.75	0.02	0.09	11.3	4.64	0.27	0.01	0.30	99.7
53.0	0.16	28.6	0.61	0.04	0.11	12.2	4.64	0.26	0.03	0.27	99.9
54.1	0.22	27.6	0.69	0.08	0.09	11.4	4.88	0.31	0.00	0.20	99.5

SiO ₂	TiO ₂	Al ₂ O ₃	FeO*	MnO	MgO	CaO	Na ₂ O	K ₂ O	BaO	SrO	Total
Basalt of Al Labah (1256 C.E.)—Continued											
Sample R15DD015 (15 analyses)—Continued											
53.9	0.14	28.4	0.76	0.07	0.08	11.6	4.71	0.27	0.00	0.20	100.1
53.7	0.21	28.0	0.75	0.04	0.10	11.2	4.81	0.28	0.00	0.00	99.1
54.1	0.24	27.7	0.62	0.04	0.10	11.2	4.94	0.31	0.03	0.42	99.7
52.5	0.17	28.7	0.72	0.00	0.09	12.6	4.04	0.21	0.11	0.30	99.4
55.1	0.10	27.2	0.73	0.00	0.11	10.6	5.12	0.33	0.09	0.22	99.6
52.8	0.18	28.7	0.68	0.00	0.09	12.6	4.19	0.20	0.00	0.10	99.5
53.7	0.25	27.9	0.92	0.00	0.09	11.2	4.52	0.29	0.00	0.05	98.9
Sample R15DD012 (15 analyses)											
54.8	0.34	26.2	1.21	0.04	0.21	10.4	4.98	0.35	0.00	0.10	98.7
52.5	0.17	28.4	0.77	0.01	0.19	12.5	4.25	0.25	0.00	0.00	99.1
54.1	0.21	28.0	0.76	0.05	0.13	11.4	4.75	0.31	0.07	0.27	100.1
53.3	0.21	28.2	0.67	0.03	0.12	11.9	4.73	0.27	0.01	0.00	99.5
54.1	0.28	28.1	0.91	0.07	0.13	11.3	4.81	0.28	0.00	0.40	100.3
50.6	0.33	25.4	1.78	0.08	0.50	12.1	4.14	0.31	0.00	0.12	95.4
54.2	0.24	28.0	0.86	0.02	0.14	11.4	4.85	0.34	0.03	0.25	100.4
54.0	0.10	28.0	0.60	0.03	0.11	11.8	4.56	0.22	0.00	0.10	99.5
54.1	0.21	27.9	0.66	0.00	0.12	11.5	4.80	0.27	0.04	0.02	99.6
54.2	0.17	27.8	0.69	0.03	0.10	11.4	5.03	0.27	0.06	0.22	100.0
54.3	0.10	27.9	0.55	0.02	0.11	11.2	4.96	0.26	0.06	0.00	99.5
52.6	0.21	28.5	0.74	0.02	0.10	12.3	3.88	0.19	0.07	0.00	98.7
53.7	0.23	27.8	0.73	0.10	0.09	11.7	4.48	0.28	0.00	0.00	99.1
52.7	0.14	29.2	0.62	0.13	0.13	12.9	4.09	0.21	0.03	0.22	100.4
52.5	0.14	29.2	0.62	0.10	0.12	12.6	4.07	0.20	0.07	0.00	99.6
Sample R15DD010 (15 analyses)											
49.3	0.05	30.5	0.75	0.07	0.10	15.0	2.95	0.13	0.16	0.00	99.0
55.0	0.20	28.0	0.70	0.00	0.13	10.9	5.36	0.25	0.10	0.07	100.8
49.8	0.06	31.9	0.76	0.00	0.15	15.6	2.83	0.08	0.10	0.08	101.3
54.1	0.24	28.8	0.69	0.00	0.10	11.9	4.64	0.21	0.06	0.00	100.7
51.5	0.11	30.4	0.76	0.10	0.17	13.6	3.75	0.16	0.00	0.20	100.8
55.5	0.31	27.7	0.76	0.06	0.14	10.5	5.43	0.31	0.00	0.22	100.9
50.9	0.04	31.1	0.82	0.18	0.13	14.6	3.36	0.16	0.00	0.03	101.3
53.7	0.19	28.7	0.64	0.05	0.09	11.9	4.72	0.25	0.00	0.00	100.1
53.3	0.19	29.3	0.61	0.09	0.12	12.5	4.37	0.22	0.00	0.20	100.9
53.4	0.22	28.8	0.64	0.07	0.11	12.1	4.52	0.23	0.00	0.12	100.2
53.5	0.27	28.5	0.57	0.11	0.11	11.7	4.67	0.26	0.06	0.42	100.1
51.9	0.18	30.2	0.79	0.12	0.14	13.6	3.74	0.19	0.17	0.57	101.7
53.5	0.21	28.9	0.88	0.07	0.14	12.2	4.49	0.23	0.10	0.37	101.1
50.2	0.12	30.9	0.69	0.07	0.14	14.9	3.11	0.11	0.01	0.07	100.3
55.1	0.24	27.3	1.05	0.03	0.20	11.1	5.11	0.29	0.00	0.15	100.6
Sample R16HD010 (14 analyses)											
52.1	0.18	28.8	0.69	0.00	0.18	12.7	4.06	0.20	0.04	0.20	99.1
51.8	0.20	30.2	0.55	0.10	0.12	13.9	3.84	0.17	0.00	0.05	100.9
50.5	0.29	27.8	1.18	0.12	0.27	12.7	3.75	0.24	0.00	0.22	97.0
49.9	0.08	31.0	0.61	0.09	0.11	15.1	2.92	0.13	0.00	0.00	100.0

SiO ₂	TiO ₂	Al ₂ O ₃	FeO*	MnO	MgO	CaO	Na ₂ O	K ₂ O	BaO	SrO	Total
Basalt of Al Labah (1256 C.E.)—Continued											
Sample R16HD010 (14 analyses)—Continued											
51.1	0.13	30.6	0.69	0.12	0.15	14.3	3.48	0.14	0.10	0.00	100.7
50.6	0.10	30.8	0.64	0.11	0.15	14.6	3.23	0.13	0.22	0.00	100.6
51.4	0.20	30.7	0.46	0.06	0.09	13.7	3.80	0.14	0.13	0.40	101.1
50.9	0.10	31.0	0.58	0.10	0.18	14.6	3.35	0.12	0.01	0.23	101.2
51.8	0.17	30.2	0.70	0.02	0.15	13.7	4.00	0.17	0.04	0.53	101.5
52.6	0.07	30.2	0.81	0.03	0.13	13.2	4.20	0.20	0.20	0.28	101.9
50.5	0.14	31.0	0.69	0.02	0.21	14.8	3.18	0.11	0.10	0.28	101.1
52.0	1.06	26.3	3.14	0.12	1.05	12.1	4.48	0.37	0.26	0.30	101.1
51.8	0.13	30.4	0.60	0.09	0.16	14.1	3.85	0.14	0.04	0.10	101.4
52.5	0.15	29.8	0.64	0.11	0.13	13.3	4.14	0.18	0.00	0.08	101.0
Basalt of Northern Fingers											
Sample R15DD018 (10 analyses)											
53.4	0.31	28.5	0.61	0.05	0.13	11.8	4.65	0.26	0.07	0.07	99.8
53.2	0.28	28.8	0.78	0.00	0.11	11.6	4.69	0.29	0.23	0.00	100.0
51.3	0.15	30.6	0.66	0.00	0.13	13.6	3.64	0.15	0.00	0.09	100.3
52.0	0.06	29.9	0.74	0.00	0.11	12.9	4.10	0.19	0.07	0.16	100.2
50.9	0.17	30.7	0.55	0.00	0.12	13.6	3.72	0.18	0.15	0.09	100.2
51.6	0.10	30.2	0.71	0.05	0.13	13.4	3.89	0.17	0.00	0.14	100.4
51.4	0.14	30.5	0.63	0.03	0.14	13.4	3.76	0.13	0.00	0.34	100.5
51.7	0.16	29.8	0.63	0.02	0.12	13.2	3.90	0.17	0.23	0.34	100.3
50.8	0.18	30.1	0.61	0.02	0.10	14.0	3.73	0.19	0.10	0.14	100.0
53.4	0.35	27.9	1.29	0.08	0.21	11.7	4.73	0.30	0.00	0.00	100.0
Sample R15DD014 (6 analyses)											
52.9	0.17	29.1	0.61	0.09	0.09	13.2	4.15	0.19	0.07	0.14	100.6
52.3	0.25	29.1	1.01	0.07	0.15	13.4	3.96	0.18	0.00	0.12	100.5
53.5	0.22	28.6	0.73	0.06	0.10	12.4	4.51	0.19	0.11	0.12	100.6
51.9	0.17	29.4	0.66	0.00	0.10	13.6	3.84	0.14	0.00	0.19	100.0
52.6	0.17	29.3	0.46	0.08	0.08	13.0	4.37	0.21	0.00	0.30	100.5
53.7	0.36	28.6	0.67	0.00	0.11	12.2	4.59	0.23	0.10	0.25	100.8
Basalt of Central Finger											
Sample R16HD01 (10 analyses)											
52.4	0.34	29.6	0.70	0.11	0.09	12.9	4.22	0.22	0.06	0.37	101.0
52.9	0.28	29.3	0.70	0.10	0.08	12.6	4.54	0.23	0.11	0.00	100.8
53.1	0.32	29.5	0.86	0.08	0.13	12.6	4.29	0.22	0.14	0.07	101.3
51.6	0.38	29.4	0.99	0.04	0.16	13.0	3.77	0.19	0.08	0.23	99.9
52.6	0.38	29.3	0.82	0.13	0.13	12.8	4.37	0.22	0.00	0.32	101.0
53.1	0.30	29.1	0.64	0.02	0.10	12.3	4.60	0.22	0.14	0.28	100.8
52.7	0.18	28.8	0.80	0.02	0.12	12.5	4.41	0.23	0.07	0.05	99.8
52.2	0.32	29.2	0.63	0.01	0.14	12.9	4.19	0.19	0.00	0.30	100.0
51.6	0.20	29.9	0.72	0.00	0.13	13.6	3.76	0.16	0.00	0.64	100.6
52.1	0.25	29.7	0.90	0.02	0.10	13.2	3.96	0.18	0.10	0.23	100.7
Sample R16HD14 (8 analyses)											
52.6	0.28	29.5	0.78	0.05	0.11	12.8	4.05	0.20	0.01	0.28	100.7
52.3	0.30	29.5	0.90	0.00	0.14	12.6	4.18	0.18	0.26	0.00	100.3

SiO ₂	TiO ₂	Al ₂ O ₃	FeO*	MnO	MgO	CaO	Na ₂ O	K ₂ O	BaO	SrO	Total
Basalt of Central Finger—Continued											
Sample R16HD14 (8 analyses)—Continued											
52.8	0.24	29.5	0.67	0.09	0.07	12.7	4.07	0.20	0.00	0.42	100.7
52.3	0.23	29.0	0.75	0.01	0.11	12.6	4.06	0.20	0.10	0.00	99.4
53.2	0.12	29.0	0.90	0.00	0.12	12.0	4.58	0.20	0.22	0.23	100.6
52.1	0.28	29.7	0.85	0.01	0.13	12.6	4.20	0.19	0.01	0.37	100.4
53.4	0.26	28.6	0.80	0.07	0.08	12.3	4.44	0.23	0.04	0.25	100.5
53.2	0.29	28.8	0.56	0.06	0.08	12.5	4.41	0.23	0.11	0.02	100.2
Sample R16HD13 (10 analyses)											
50.4	0.14	30.2	0.74	0.05	0.14	13.9	3.46	0.13	0.05	0.14	99.3
50.3	0.19	30.3	0.81	0.00	0.17	13.6	3.64	0.13	0.05	0.17	99.3
51.7	0.27	29.2	1.15	0.00	0.18	12.2	4.17	0.19	0.00	0.14	99.2
50.7	0.16	30.2	0.76	0.00	0.15	13.4	3.75	0.14	0.04	0.10	99.4
50.3	0.10	30.2	0.67	0.03	0.12	13.4	3.74	0.16	0.13	0.19	98.9
49.9	0.13	30.8	0.58	0.10	0.13	13.5	3.43	0.12	0.10	0.19	99.0
50.3	0.17	30.3	0.72	0.06	0.12	13.0	3.70	0.15	0.06	0.15	98.7
51.4	0.24	29.5	0.82	0.01	0.13	12.8	3.90	0.17	0.01	0.17	99.1
51.5	0.16	30.3	0.70	0.01	0.18	13.6	3.68	0.14	0.00	0.20	100.4
52.4	0.20	29.7	0.83	0.00	0.09	12.9	3.89	0.18	0.00	0.13	100.3
Sample R16HD15 (5 analyses)											
51.9	0.23	29.8	0.92	0.01	0.15	13.3	3.82	0.17	0.21	0.18	100.7
55.0	0.30	26.9	1.17	0.05	0.25	10.4	5.21	0.39	0.04	0.17	99.9
54.4	0.24	27.8	1.13	0.07	0.12	10.7	4.94	0.30	0.09	0.10	99.9
52.2	0.18	29.8	0.80	0.05	0.16	13.2	3.97	0.16	0.10	0.21	100.8
52.5	0.12	30.6	0.72	0.02	0.17	13.9	3.68	0.14	0.06	0.16	102.1
Sample R16HD16 (10 analyses)											
55.3	0.43	27.1	1.49	0.05	0.21	10.6	5.30	0.33	0.00	0.28	101.1
53.5	0.36	28.4	1.06	0.05	0.14	11.9	4.49	0.30	0.00	0.23	100.4
51.8	0.16	30.1	0.91	0.04	0.12	13.4	3.73	0.16	0.03	0.27	100.7
53.1	0.25	29.4	0.81	0.00	0.10	12.4	4.17	0.22	0.04	0.28	100.7
52.2	0.16	30.0	0.80	0.01	0.15	13.2	3.90	0.17	0.13	0.29	101.0
53.2	0.26	28.8	0.89	0.02	0.15	12.5	4.56	0.23	0.00	0.25	100.9
54.0	0.24	27.9	0.96	0.04	0.14	11.7	4.80	0.29	0.00	0.11	100.2
53.4	0.26	28.0	1.01	0.00	0.16	11.8	4.60	0.27	0.01	0.07	99.5
56.3	0.30	26.4	1.05	0.00	0.16	10.0	5.59	0.48	0.11	0.29	100.7
52.8	0.26	28.9	0.93	0.03	0.14	12.8	4.10	0.19	0.06	0.27	100.4
Basalt of Southern Fingers											
Sample R16HD09 (11 analyses)											
50.0	0.18	32.0	0.52	0.08	0.18	15.2	2.97	0.06	0.00	0.35	101.5
51.1	0.12	31.3	0.70	0.00	0.29	13.9	3.60	0.13	0.00	0.30	101.5
51.3	0.19	31.5	0.72	0.09	0.12	13.7	3.71	0.16	0.00	0.30	101.7
51.0	0.14	31.7	0.74	0.08	0.14	14.2	3.57	0.10	0.00	0.05	101.6
51.3	0.30	30.8	0.62	0.03	0.18	14.0	3.68	0.13	0.14	0.00	101.2
51.1	0.11	31.1	0.67	0.02	0.17	13.9	3.50	0.13	0.14	0.09	100.9
51.4	0.16	29.9	0.66	0.00	0.16	13.4	3.71	0.16	0.06	0.12	99.7
51.7	0.11	29.5	0.60	0.10	0.18	13.4	4.00	0.17	0.06	0.00	99.8

SiO₂	TiO₂	Al₂O₃	FeO*	MnO	MgO	CaO	Na₂O	K₂O	BaO	SrO	Total
Basalt of Southern Fingers—Continued											
Sample R16HD09 (11 analyses)—Continued											
51.3	0.14	29.6	0.78	0.06	0.16	13.6	3.79	0.16	0.10	0.00	99.6
51.4	0.12	31.2	0.76	0.04	0.15	14.2	3.35	0.13	0.17	0.00	101.4
50.6	0.18	31.6	0.57	0.03	0.12	14.4	3.21	0.10	0.14	0.21	101.1
Sample R16HD27 (7 analyses)											
51.3	0.15	30.1	0.75	0.10	0.11	13.6	3.36	0.15	0.11	0.32	100.0
52.2	0.15	29.7	0.72	0.21	0.15	13.3	3.69	0.15	0.11	0.28	100.7
51.6	0.15	30.3	0.65	0.03	0.13	13.6	3.68	0.12	0.00	0.05	100.3
51.5	0.15	30.2	0.69	0.01	0.16	13.6	3.67	0.13	0.19	0.23	100.5
51.4	0.10	29.7	0.71	0.08	0.17	13.8	3.53	0.14	0.14	0.00	99.8
51.5	0.08	29.5	0.68	0.01	0.15	13.5	3.72	0.12	0.00	0.00	99.3
52.3	0.11	29.3	0.69	0.08	0.12	13.1	3.81	0.18	0.11	0.00	99.8
Sample R16HD26 (9 analyses)											
53.0	0.16	29.1	0.42	0.07	0.16	13.1	3.89	0.19	0.00	0.00	100.1
52.3	0.24	28.3	0.94	0.08	0.23	13.1	3.79	0.18	0.26	0.14	99.5
52.7	0.46	28.3	1.26	0.12	0.81	13.3	4.05	0.18	0.00	0.52	101.7
52.1	0.16	30.4	0.63	0.00	0.12	13.9	3.73	0.18	0.14	0.24	101.6
52.2	0.19	29.3	0.46	0.05	0.18	13.3	3.79	0.13	0.11	0.00	99.7
53.0	0.24	29.4	0.63	0.00	0.18	12.5	4.39	0.18	0.00	0.61	101.1
53.8	0.35	29.5	0.51	0.02	0.17	13.0	4.18	0.16	0.14	0.75	102.6
53.9	0.05	30.1	0.63	0.11	0.14	12.9	4.10	0.20	0.17	0.00	102.3
51.9	0.24	30.6	0.60	0.10	0.14	13.7	3.64	0.11	0.18	0.26	101.4

Appendix 5. Microprobe Analyses of Olivine in Harrat Rahat Basaltic Lava Flows

[Values in weight percent. All iron reported as FeO (FeO*). -, not analyzed]

SiO ₂	FeO*	MnO	MgO	CaO	Cr ₂ O ₃	NiO	Total
Basalt of Al Labah (1256 C.E.)							
Sample R14TS95 (8 analyses)							
37.3	24.2	0.39	37.1	0.36	-	0.05	99.5
37.7	23.9	0.44	37.2	0.36	-	0.07	99.7
37.8	23.7	0.41	37.1	0.37	-	0.05	99.3
37.7	25.3	0.46	36.1	0.42	-	0.08	100.1
37.5	24.7	0.42	36.3	0.41	-	0.07	99.5
37.8	23.6	0.40	37.4	0.32	-	0.14	99.7
37.8	24.2	0.36	37.3	0.33	-	0.11	100.1
37.5	23.6	0.41	37.2	0.39	-	0.06	99.1
Sample R15DD150B (8 analyses)							
39.0	14.9	0.31	43.8	0.32	0.02	0.10	98.5
39.4	14.3	0.23	45.3	0.30	0.00	0.22	99.7
38.8	14.2	0.20	44.4	0.32	0.00	0.10	98.0
39.7	14.3	0.24	46.0	0.32	0.00	0.19	100.8
39.5	15.2	0.27	44.6	0.35	0.00	0.20	100.2
39.2	16.7	0.26	43.5	0.38	0.00	0.24	100.3
36.3	18.9	0.29	35.4	0.52	0.08	0.11	91.6
39.1	14.7	0.26	43.1	0.32	0.14	0.08	97.7
Sample R15DD015 (25 analyses)							
37.1	27.7	0.48	34.2	0.00	0.00	0.00	99.5
37.3	26.7	0.57	35.5	0.00	0.00	0.00	100.1
37.0	27.4	0.47	34.4	0.52	0.02	0.00	99.8
37.2	26.7	0.54	35.0	0.32	0.00	0.00	99.7
36.7	26.7	0.51	35.1	0.37	0.00	0.00	99.4
37.5	27.1	0.54	35.0	0.40	0.00	0.00	100.5
37.4	26.4	0.55	34.7	0.35	0.00	0.00	99.4
37.3	27.3	0.55	34.0	0.43	0.01	0.00	99.6
37.3	27.7	0.47	34.4	0.35	0.00	0.00	100.2
37.3	28.0	0.50	34.1	0.38	0.00	0.00	100.2
37.4	28.0	0.50	34.3	0.38	0.02	0.00	100.5
37.1	27.7	0.60	34.3	0.41	0.01	0.00	100.1
37.5	27.3	0.55	35.4	0.35	0.02	0.00	101.1
37.2	26.3	0.48	35.4	0.40	0.00	0.00	99.8
37.4	27.3	0.52	34.1	0.39	0.04	0.00	99.8
37.3	27.0	0.59	34.9	0.37	0.07	0.00	100.2
37.1	26.8	0.59	34.5	0.36	0.06	0.00	99.4
37.1	27.1	0.59	34.4	0.38	0.00	0.00	99.6
37.1	27.5	0.49	34.5	0.43	0.00	0.00	100.0
37.5	27.0	0.62	35.1	0.33	0.00	0.00	100.5

SiO ₂	FeO*	MnO	MgO	CaO	Cr ₂ O ₃	NiO	Total
Basalt of Al Labah (1256 C.E.)—Continued							
Sample R15DD015 (25 analyses)—Continued							
37.6	25.7	0.45	35.8	0.33	0.00	0.00	99.9
37.0	27.4	0.66	34.8	0.39	0.00	0.00	100.2
36.8	27.2	0.63	33.6	0.50	0.00	0.00	98.8
37.2	27.7	0.66	34.4	0.34	0.00	0.00	100.3
37.5	27.4	0.48	34.9	0.36	0.03	0.00	100.6
Sample R15DD012 (23 analyses)							
37.7	26.8	0.50	35.4	0.29	0.00	0.00	100.7
36.9	26.8	0.48	33.8	0.91	0.00	0.00	98.8
37.1	26.6	0.49	34.6	0.39	0.00	0.00	99.2
37.6	26.6	0.53	35.4	0.32	0.00	0.00	100.5
37.9	25.8	0.51	36.2	0.27	0.01	0.00	100.6
36.8	26.9	0.56	34.8	0.43	0.04	0.00	99.4
38.1	26.1	0.48	36.2	0.46	0.03	0.00	101.3
37.6	25.9	0.51	35.7	0.42	0.03	0.00	100.1
37.2	26.3	0.53	35.0	0.27	0.00	0.00	99.2
37.2	26.9	0.54	34.9	0.41	0.00	0.00	99.9
37.2	27.2	0.56	34.7	0.36	0.01	0.00	100.0
36.9	27.4	0.56	34.5	0.35	0.04	0.00	99.8
37.7	27.0	0.50	34.9	0.37	0.03	0.00	100.6
37.5	27.4	0.37	34.8	0.44	0.01	0.00	100.4
37.5	27.2	0.35	34.9	0.37	0.02	0.00	100.3
37.4	27.0	0.56	34.8	0.39	0.01	0.00	100.1
37.1	27.3	0.64	34.9	0.36	0.00	0.00	100.3
37.2	27.3	0.58	35.0	0.40	0.00	0.00	100.4
37.3	27.2	0.61	35.0	0.38	0.03	0.00	100.5
37.3	27.2	0.52	34.8	0.38	0.00	0.00	100.1
37.1	27.0	0.63	34.3	0.40	0.00	0.00	99.4
37.5	26.6	0.40	35.6	0.30	0.01	0.00	100.3
37.5	27.3	0.48	35.1	0.34	0.01	0.00	100.7
Sample R15DD010 (30 analyses)							
38.3	25.4	0.50	36.9	0.36	0.04	0.00	101.5
37.3	26.9	0.63	35.2	0.43	0.06	0.00	100.5
38.2	24.6	0.24	36.9	0.48	0.00	0.00	100.4
37.8	24.4	0.45	36.9	0.49	0.00	0.00	100.0
37.8	25.5	0.33	36.0	0.41	0.00	0.00	100.1
38.4	24.1	0.54	37.0	0.51	0.02	0.00	100.6
37.0	27.1	0.50	35.4	0.38	0.00	0.00	100.4
38.2	24.6	0.54	36.9	0.46	0.00	0.00	100.4

SiO ₂	FeO*	MnO	MgO	CaO	Cr ₂ O ₃	NiO	Total
Basalt of Al Labah (1256 C.E.)—Continued							
Sample R15DD010 (30 analyses)—Continued							
38.1	24.6	0.47	37.2	0.43	0.00	0.00	100.8
38.2	25.0	0.57	36.7	0.43	0.01	0.00	100.9
38.1	25.3	0.51	36.7	0.43	0.01	0.00	101.1
38.1	24.4	0.50	37.4	0.53	0.05	0.00	100.9
38.1	24.4	0.47	37.2	0.46	0.07	0.00	100.7
38.2	24.0	0.42	37.4	0.46	0.06	0.00	100.5
38.4	23.7	0.41	37.8	0.50	0.00	0.00	100.7
38.1	25.0	0.42	36.6	0.53	0.00	0.00	100.7
37.9	24.5	0.43	37.2	0.43	0.00	0.00	100.5
38.1	24.2	0.50	37.6	0.53	0.05	0.00	101.0
37.9	25.3	0.51	36.6	0.32	0.00	0.00	100.5
37.9	25.7	0.41	36.3	0.31	0.05	0.00	100.6
38.0	25.9	0.38	36.1	0.39	0.00	0.00	100.8
38.0	25.8	0.43	36.5	0.45	0.02	0.00	101.2
38.1	25.3	0.39	36.7	0.43	0.00	0.00	100.9
38.4	24.0	0.47	37.3	0.52	0.00	0.00	100.7
37.6	26.1	0.57	36.2	0.42	0.01	0.00	100.9
38.4	23.1	0.46	38.0	0.44	0.00	0.00	100.3
38.1	24.6	0.48	37.4	0.48	0.00	0.00	101.0
37.9	24.4	0.55	37.3	0.44	0.00	0.00	100.5
37.6	24.4	0.43	37.0	0.49	0.00	0.00	99.9
38.2	24.4	0.39	37.5	0.47	0.03	0.00	101.0
Sample R16HD010 (19 analyses)							
37.5	25.2	0.45	36.8	0.39	0.00	0.00	100.4
38.1	24.8	0.42	37.3	0.43	0.02	0.00	101.0
37.9	25.5	0.46	36.8	0.47	0.01	0.00	101.2
38.2	25.5	0.57	37.2	0.46	0.00	0.00	101.9
37.3	25.5	0.41	36.3	0.53	0.00	0.00	100.0
37.9	25.4	0.57	37.3	0.44	0.04	0.00	101.7
37.6	25.4	0.46	36.7	0.41	0.02	0.00	100.6
37.6	25.3	0.46	36.6	0.50	0.03	0.00	100.4
37.0	25.1	0.46	36.9	0.45	0.00	0.00	99.9
37.7	25.4	0.48	37.0	0.44	0.00	0.00	101.0
37.5	25.5	0.42	36.3	0.45	0.00	0.00	100.2
37.9	23.0	0.39	38.5	0.40	0.00	0.00	100.2
38.0	25.7	0.49	36.5	0.51	0.00	0.00	101.1
37.9	25.4	0.49	36.6	0.51	0.02	0.00	101.0
38.2	25.0	0.51	37.1	0.45	0.00	0.00	101.3
37.2	25.4	0.51	36.4	0.44	0.00	0.00	100.0
37.7	24.2	0.41	37.2	0.37	0.06	0.00	99.9
38.2	25.1	0.49	37.7	0.36	0.05	0.00	101.9
38.1	25.3	0.50	37.4	0.43	0.01	0.00	101.7

SiO ₂	FeO*	MnO	MgO	CaO	Cr ₂ O ₃	NiO	Total
Basalt of Northern Fingers							
Sample R15DD018 (4 analyses)							
38.0	21.5	0.42	39.3	0.30	0.04	0.04	99.6
37.4	25.5	0.33	35.4	0.24	0.04	0.15	99.1
37.5	25.5	0.35	35.6	0.00	0.05	0.07	99.1
37.5	25.9	0.45	35.2	0.01	0.01	0.08	99.1
Sample R15DD014 (10 analyses)							
38.3	23.4	0.45	37.8	0.33	0.01	0.09	100.4
38.4	22.8	0.37	39.3	0.27	0.01	0.11	101.3
39.0	22.8	0.32	38.1	0.23	0.13	0.07	100.7
38.4	24.0	0.42	37.0	0.36	0.06	0.07	100.3
38.2	24.9	0.41	35.9	0.37	0.06	0.06	99.8
38.9	20.6	0.34	39.5	0.32	0.08	0.11	99.8
38.0	25.6	0.45	35.7	0.44	0.06	0.05	100.3
39.0	22.5	0.43	38.8	0.29	0.00	0.04	101.0
39.1	22.0	0.38	39.4	0.26	0.10	0.08	101.3
38.1	26.7	0.35	35.6	0.44	0.15	0.05	101.4
Basalt of Central Finger							
Sample R16HD01 (13 analyses)							
37.8	24.7	0.39	36.6	0.42	0.03	0.09	100.0
38.4	21.0	0.37	40.4	0.27	0.07	0.13	100.6
38.2	20.8	0.42	40.2	0.23	0.11	0.12	100.0
37.9	23.3	0.30	38.6	0.31	0.08	0.06	100.6
37.8	23.7	0.41	37.5	0.44	0.15	0.05	100.1
38.3	21.2	0.39	40.3	0.30	0.00	0.08	100.5
38.3	22.1	0.35	39.8	0.27	0.08	0.07	100.9
38.2	22.8	0.33	38.6	0.29	0.03	0.09	100.2
38.5	20.6	0.32	39.7	0.26	0.04	0.08	99.5
37.5	24.0	0.33	37.9	0.31	0.00	0.04	100.1
37.6	25.0	0.46	37.1	0.39	0.03	0.00	100.6
38.4	20.5	0.35	40.1	0.33	0.17	0.12	99.9
37.8	24.5	0.38	37.6	0.37	0.05	0.07	100.7
Sample R16HD14 (6 analyses)							
38.5	21.6	0.27	39.7	0.27	0.09	0.14	100.5
38.9	20.7	0.26	40.7	0.18	0.18	0.07	101.0
38.3	22.0	0.46	39.4	0.25	0.04	0.08	100.5
38.6	21.7	0.27	39.5	0.26	0.11	0.09	100.5
39.0	20.2	0.27	41.1	0.25	0.03	0.12	101.0
38.9	20.3	0.25	40.9	0.22	0.10	0.11	100.7
Sample R16HD13 (12 analyses)							
36.7	31.0	0.66	31.6	0.44	0.02	0.03	100.5
36.4	31.0	0.69	31.7	0.43	0.20	0.05	100.5
36.4	30.9	0.86	32.1	0.48	0.00	0.02	100.7
37.3	31.3	0.68	32.4	0.42	0.00	0.08	102.3

SiO ₂	FeO*	MnO	MgO	CaO	Cr ₂ O ₃	NiO	Total
Basalt of Central Finger—Continued							
Sample R16HD13 (12 analyses)—Continued							
36.2	30.9	0.65	32.6	0.32	0.08	0.09	100.8
37.3	27.3	0.49	35.6	0.20	0.01	0.11	101.0
37.4	27.1	0.45	35.8	0.23	0.08	0.02	101.1
38.7	18.7	0.36	41.9	0.23	0.04	0.07	100.0
37.1	29.2	0.64	33.8	0.27	0.08	0.09	101.1
37.2	28.2	0.51	34.9	0.26	0.08	0.10	101.3
36.4	31.1	0.62	31.6	0.45	0.12	0.01	100.3
36.7	31.0	0.74	31.7	0.39	0.01	0.03	100.5
Sample R16HD15 (12 analyses)							
38.3	21.2	0.39	40.3	0.30	0.00	0.08	100.5
38.3	22.1	0.35	39.8	0.27	0.08	0.07	100.9
38.2	22.8	0.33	38.6	0.29	0.03	0.09	100.2
38.5	20.6	0.32	39.7	0.26	0.04	0.08	99.5
37.5	24.0	0.33	37.9	0.31	0.00	0.04	100.1
37.6	25.0	0.46	37.1	0.39	0.03	0.00	100.6
38.4	20.5	0.35	40.1	0.33	0.17	0.12	99.9
37.8	24.5	0.38	37.6	0.37	0.05	0.07	100.7
38.1	22.3	0.44	39.6	0.26	0.02	0.13	100.9
37.8	24.7	0.39	36.6	0.42	0.03	0.09	100.0
38.4	21.0	0.37	40.4	0.27	0.07	0.13	100.6
38.2	20.8	0.42	40.2	0.23	0.11	0.12	100.0
Sample R16HD16 (12 analyses)							
37.5	25.2	0.43	35.2	1.13	0.00	0.23	99.7
37.3	25.3	0.38	36.2	0.39	0.00	0.05	99.7
36.6	25.6	0.43	34.4	0.50	0.00	0.21	97.7
37.1	27.3	0.53	35.0	0.49	0.00	0.03	100.4
39.1	19.9	0.36	41.9	0.27	0.00	0.05	101.5
37.5	26.7	0.56	35.6	0.50	0.00	0.05	100.8
37.6	26.8	0.56	34.7	0.60	0.00	0.09	100.3
37.3	27.0	0.56	34.9	0.54	0.00	0.05	100.4
37.0	27.4	0.61	33.9	0.53	0.00	0.09	99.6
37.1	27.2	0.49	34.5	0.45	0.10	0.10	99.9
37.3	27.8	0.60	35.2	0.51	0.09	0.10	101.6
36.9	26.8	0.58	34.5	0.50	0.01	0.10	99.4

SiO ₂	FeO*	MnO	MgO	CaO	Cr ₂ O ₃	NiO	Total
Basalt of Southern Fingers							
Sample R16HD09 (15 analyses)							
38.9	19.8	0.24	41.5	0.44	0.18	0.09	101.1
38.9	19.2	0.18	42.0	0.38	0.04	0.14	100.8
38.7	18.9	0.27	41.8	0.38	0.13	0.12	100.3
39.0	18.2	0.28	43.0	0.28	0.00	0.17	100.9
39.0	18.8	0.26	42.6	0.30	0.04	0.11	101.1
38.8	19.5	0.31	41.3	0.31	0.11	0.16	100.5
38.2	23.5	0.31	37.9	0.51	0.16	0.10	100.6
38.1	23.1	0.42	38.4	0.49	0.20	0.11	100.8
39.3	18.0	0.26	43.5	0.30	0.03	0.17	101.6
38.8	18.3	0.29	42.7	0.34	0.11	0.16	100.7
39.2	17.7	0.26	43.3	0.34	0.09	0.18	101.1
39.0	20.3	0.27	40.7	0.38	0.00	0.20	100.8
38.9	19.2	0.38	41.2	0.41	0.00	0.14	100.3
39.2	18.7	0.28	42.9	0.32	0.04	0.14	101.5
38.7	18.6	0.24	42.2	0.35	0.04	0.14	100.2
Sample R16HD27 (5 analyses)							
39.5	17.9	0.31	42.3	0.29	0.03	0.14	100.4
39.1	18.7	0.32	41.4	0.27	0.12	0.12	100.0
38.4	21.5	0.36	39.7	0.38	0.10	0.09	100.5
38.0	21.4	0.39	38.9	0.39	0.08	0.12	99.3
38.9	19.4	0.27	41.1	0.29	0.00	0.09	100.0
Sample R16HD26 (3 analyses)							
38.2	21.8	0.36	38.7	0.45	0.10	0.09	99.6
38.6	20.8	0.46	39.8	0.38	0.00	0.11	100.1
38.7	20.0	0.34	41.0	0.41	0.08	0.12	100.6

Appendix 6. Geothermometry Results and Sample Locations

[km, kilometer]

Basalt of Al Labah (1256 C.E.)						
Sample	R14TS95	R15DD150B	R15DD15	R15DD12	R15DD10	R16HD10
Description	Tephra	Lava	Lava	Lava	Lava	Lava
Distance from vent (km)	0	3.5	5.5	11.1	13.5	20.2
Thermometry, in degrees Celsius						
MgO in glass (Helz and Thornber, 1987)	1,121	1,124	1,093	1,104	1,114	1,084
CaO in glass (Helz and Thornber, 1987)	1,109	1,133	1,117	1,109	1,113	1,138
MgO in glass (Montierth and others, 1995)	1,134	1,138	1,102	1,115	1,127	1,092
Glass composition (Putirka, 2008, eq. 13)	1,134	1,138	1,098	1,112	1,125	1,086
Glass composition (Putirka, 2008, eq. 14)	1,172	1,174	1,139	1,149	1,167	1,129
Glass composition (Putirka, 2008, eq. 15)	1,155	1,158	1,122	1,135	1,150	1,114
Glass composition (Yang and others, 1996)	1,107	1,111	1,081	1,093	1,100	1,070
Olivine-liquid (Beattie, 1993)	1,157	1,153	1,116	1,134	1,144	1,089
Olivine-liquid (Putirka and others, 2007, eq. 2)	1,143	1,115	1,095	1,119	1,126	1,049
Olivine-liquid (Putirka and others, 2007, eq. 4)	1,176	1,143	1,121	1,147	1,157	1,065
Olivine-liquid (Sisson and Grove, 1993, eq. 1)	1,157	1,153	1,135	1,142	1,150	1,124
Olivine-liquid (Sisson and Grove, 1993, eq. 4)	1,112	1,091	1,068	1,092	1,099	1,031
Plagioclase-liquid (Putirka, 2008, eq. 23)	1,164	1,172	1,152	1,151	1,162	1,158
Plagioclase-liquid (Putirka, 2005, eq. 24a)	1,136	1,149	1,118	1,123	1,133	1,131
Average	1,141	1,139	1,111	1,123	1,133	1,097
Standard error	6	6	6	5	6	10

References Cited

- Beattie, P., 1993, Olivine-melt and orthopyroxene-melt equilibria: Contributions to Mineralogy and Petrology, v. 115, p. 103–111, <https://doi.org/10.1007/BF00712982>.
- Helz, R.T., and Thornber, C.R., 1987, Geothermometry of Kilauea Iki lava lake, Hawaii: Bulletin of Volcanology, v. 49, no. 5, p. 651–668, <https://doi.org/10.1007/BF01080357>.
- Montierth, C., Johnston, A.D., and Cashman, K.V., 1995, An empirical glass-composition-based geothermometer for Mauna Loa lavas, in Rhodes, J.M. and Lockwood, J.P. eds., *Mauna Loa Revealed—Structure, Composition, History, and Hazards*: American Geophysical Union, p. 207–217.
- Putirka, K.D., 2005, Igneous thermometers and barometers based on plagioclase + liquid equilibria—Tests of some existing models and new calibrations: American Mineralogist, v. 90, no. 2–3, p. 336–346, <https://doi.org/10.2138/am.2005.1449>.

Basalt of Northern Fingers		Basalt of Central Finger					Basalt of Southern Fingers		
R15DD18	R15DD14	R16HD1	R16HD14	R16HD13	R16HD15	R16HD16	R16HD9	R16HD27	R16HD26
Spatter	Lava	Spatter	Lava	Lava	Lava	Lava	Spatter	Spatter	Lava
0	8.9	0	1	3	5.2	8.8	0	0	0.3
Thermometry, in degrees Celsius									
1,107	1,110	1,123	1,115	1,104	1,073	1,081	1,135	1,124	1,092
1,097	1,112	1,106	1,152	1,118	1,088	1,107	1,139	1,133	1,173
1,118	1,121	1,136	1,120	1,115	1,079	1,086	1,150	1,138	1,101
1,115	1,119	1,137	1,118	1,113	1,071	1,080	1,153	1,139	1,096
1,145	1,156	1,173	1,164	1,131	1,083	1,110	1,182	1,174	1,120
1,136	1,143	1,157	1,149	1,129	1,078	1,099	1,168	1,158	1,113
1,098	1,096	1,109	1,095	1,093	1,079	1,088	1,120	1,111	1,078
1,129	1,133	1,155	1,137	1,113	1,072	1,086	1,157	1,153	1,083
1,104	1,107	1,134	1,143	1,077	1,031	1,062	1,135	1,128	1,053
1,129	1,135	1,167	1,187	1,095	1,025	1,079	1,167	1,159	1,069
1,119	1,134	1,159	1,130	1,150	1,101	1,104	1,149	1,137	1,111
1,089	1,087	1,108	1,114	1,070	1,010	1,041	1,113	1,102	1,037
1,138	1,160	1,166	1,146	1,160	1,120	1,119	1,180	1,169	1,158
1,127	1,134	1,139	1,121	1,135	1,113	1,103	1,154	1,145	1,135
1,118	1,125	1,141	1,135	1,114	1,073	1,089	1,150	1,141	1,101
5	6	6	6	7	9	6	5	6	10

Putirka, K.D., 2008, Thermometers and barometers for volcanic systems: Reviews in Mineralogy and Geochemistry, v. 69, no. 1, p. 61–120, <https://doi.org/10.2138/rmg.2008.69.3>.

Putirka, K.D., Perfit, M., Ryerson, F.J., and Jackson, M.G., 2007, Ambient and excess mantle temperatures, olivine thermometry, and active vs. passive upwelling: Chemical Geology, v. 241, no. 3, p. 177–206, <https://doi.org/10.1016/j.chemgeo.2007.01.014>.

Sisson, T.W., and Grove, T.L., 1993, Temperatures and H₂O contents of low-MgO high-alumina basalts: Contributions to Mineralogy and Petrology, v. 113, no. 2, p. 167–184, <https://doi.org/10.1007/BF00283226>.

Yang, H.-J., Kinzler, R.J., and Grove, T.L., 1996, Experiments and models of anhydrous, basaltic olivine-plagioclase-augite saturated melts from 0.001 to 10 kbar: Contributions to Mineralogy and Petrology, v. 124, p. 1–18.

